Kinetic Modeling Methods for the Measurement of Glucose Metabolism and Blood Flow with Total-Body PET

By

ELIZABETH JANE SI YING LI
DISSERTATION

Submitted in partial satisfaction of the requirements for the degree of

DOCTOR OF PHILOSOPHY

in

Biomedical Engineering

in the

OFFICE OF GRADUATE STUDIES

of the

UNIVERSITY OF CALIFORNIA

DAVIS

Approved:

_____

Simon R. Cherry, Chair

_____

Guobao Wang

_____

Alice F. Tarantal

_____

Audrey P. Fan

Committee in Charge

2022

Abstract

PET/CT systems are used to visualize and quantify molecular processes *in vivo*. The extended axial field of view (FOV) of total-body PET/CT systems, like the recently developed uEXPLORER, leads to increased system sensitivity and can allow for reduced scan time and dose, improvements in image quality, and most importantly for this work, the ability to fit the entire body of a subject within the FOV. The FOV includes large blood pools in addition to any organ of interest, allowing for the use of an appropriate image-derived input function (IDIF) for the purposes of quantitative total-body PET kinetic modeling.

Although the first clinical scans on the uEXPLORER at UC Davis were performed in 2019, *in vivo* assessment of the quantitative performance of the scanner and the development of total-body PET kinetic modeling methods are necessary to extend single-organ and limited FOV studies to encompass organs throughout the entire body. Thus, this work focused on the development of total-body PET kinetic modeling methods. First, via a group of fourteen healthy volunteers who underwent 60-minute dynamic PET acquisitions on the uEXPLORER system with the commonly used radiotracer [^{18}F]-fluorodeoxyglucose (FDG), *in vivo* performance metrics were established to quantitatively assess differences in the reconstructed images from a newly installed total-body PET system (e.g., due to software updates and reconstruction settings), and methods to mitigate the impact of motion (e.g., respiratory) and partial volume effects across a wide range of organs were determined. Then, with the same cohort of healthy subjects in addition to seven patients with genitourinary cancer, the computational efficiency of voxel-wise total-body PET kinetic modeling was increased by a factor of 6.7 through the development of the leading-edge method for time delay correction of the IDIF. Without delay correction there was an underestimation of blood volume, v_b (69.4%), and the rate of FDG transport from blood to tissue, K_1 (4.8%).

Total-body PET kinetic modeling methods developed above using FDG datasets were extended to the assessment of [^{11}C]-butanol for total-body imaging of tissue blood flow (perfusion). The application of total-body PET/CT for radiation dosimetry of tracers with rapid kinetics and short half-life was demonstrated with this tracer. Radiation doses were estimated on an early small-scale prototype of a total-body PET scanner in two young rhesus monkeys and subsequently on the uEXPLORER in humans. Average adult dosimetry estimates of total effective dose were consistent (rhesus monkeys-derived: 3.67 uSv/MBq, human-derived: 3.64 uSv/MBq). Perfusion test-retest reproducibility was established in healthy volunteers at a wide range of flow values and showed good repeatability (slope 0.9, Pearson's $r = 0.97$, $p < 0.001$) with up to two weeks between acquisitions. Intra-human sensitivity assessments were performed in two ways: (1) a rest-stress paradigm with a cold pressor test and (2) the comparison of right and left lower limbs for an individual with peripheral artery disease. Initial studies demonstrated changes in perfusion in both cases.

In this work, appropriate methods for the quantitative assessment of total-body dynamic PET images were developed; computational efficiency of total-body kinetic modeling was increased 6.7-fold; and ultimately, these methods were developed and exploited in the measurement of FDG transport, FDG metabolism and [^{11}C]-butanol perfusion, in organs throughout the body.

Acknowledgements

First and foremost, I am extremely grateful to Prof. Simon R. Cherry for his tremendous support throughout this process and for giving me the chance to work with an incredible group of scientists, and Prof. Guobao Wang for his wonderful co-mentorship and guidance. I would also like to thank my defense committee members Prof. Audrey P. Fan and Prof. Alice F. Tarantal for their time and effort to provide invaluable suggestions to improve this work. And many thanks to Prof. Ramsey D. Badawi for chairing my qualifying exam, and for his unwavering support of this work as well.

Secondly, I am extremely appreciative of the members of the MIPET and EMIC groups for their guidance, friendship, and mentorship over the years. Although there are many members of the group who have generously taken the time to teach me new concepts or provide suggestions, this work would not have been possible without the advocacy and help of Dr. Benjamin Spencer.

Thirdly, I would like to thank my family and friends for all their encouragement and support. And finally, I cannot thank my partner Pete enough for keeping my spirits high with plenty of laughter and willingness to set out on new adventures.

Table of Contents

List of Figures

List of Tables

1. Chapter 1: Background

1.1. Molecular imaging

Molecular imaging is a subset of medical imaging that involves the visualization and characterization of molecular or cellular level processes *in vivo* (Mankoff, 2007) through the use of a molecular probe or imaging agent. Some medical imaging modalities that can be leveraged for molecular imaging include optical coherence tomography (OCT), ultrasound (US), magnetic resonance imaging (MRI), x-ray computed tomography (CT), positron emission tomography (PET), and single photon emission computed tomography (SPECT). Many of these modalities use inherent properties of the tissue to generate contrast. For example, OCT detects on the interactions of visible or infrared light with tissue, relying on heterogenous tissue absorption and scattering characteristics to generate contrast. Similarly, ultrasound signal utilizes the propagation and reflection of sound waves within a tissue. CT relies on the differences in the radiodensity, or absorption and transmittance of X-rays through the different tissues in the body. The biochemical properties of a tissue can be leveraged as well. MRI involves manipulating the magnetic fields experienced by water protons throughout the body, and differences in the chemical environments of those protons result in signal contrast. While endogenous contrast allows these modalities to be minimally or noninvasive, contrast can be enhanced through the use of a contrast media or injected dye.

Nuclear medicine is a branch of medical imaging that includes PET and SPECT. Nuclear medicine with PET and SPECT involves detection of the emissions from an externally supplied radioactive source of contrast that is used for gaining a functional understanding of the behavior of the contrast agent *in vivo*. Referred to as a radiotracer, the PET contrast agent is a compound labeled with a positron-emitting radioisotope. It can be introduced into the blood pool of the subject,

most commonly via intravenous injection. How the radiotracer interacts with different tissues throughout the body over time will depend on the radiotracer used, allowing for specific image contrasts that are based on the physiology of individual tissues or organs.

1.2. Radiotracers of interest: [^{18}F]-FDG and [^{11}C]-butanol

This work focused on the metabolism and distribution of 2-deoxy-2-[^{18}F]-fluoro-D-glucose (FDG) and the kinetics and radiation dosimetry of [^{11}C]-butanol. FDG, one of the most commonly used PET radiotracers, is structurally similar (i.e., an analog) to glucose, and is taken up by different organs of the body in a similar manner to glucose. Upon uptake into the cell, FDG is phosphorylated ([^{18}F]-FDG-6-phosphate or FDG6P) by hexokinase, as would occur with glucose. However, FDG6P is irreversibly trapped in the cell, and further metabolism of FDG6P does not occur due to the substitution of the hydroxyl group at the number 2 carbon for fluorine-18. Although FDG is non-specific to any particular disease pathology, glucose metabolism has been shown to be increased in cancerous lesions, and thus has been used extensively in tumor lesion evaluation and staging (Cori & Cori, 1925; Hess et al., 2014; Warburg et al., 1927). [^{11}C]-butanol is a perfusion or blood flow tracer that has been used previously to estimate cerebral and myocardial blood flow in humans (Hack et al., 1983; Manouilenko et al., 2013; Quarles et al., 1993). It is metabolized in a similar manner to ethanol by alcohol dehydrogenase: [^{11}C]-butanol is rapidly converted to [^{11}C]-butyric aldehyde, which is then oxidized by aldehyde dehydrogenase to form [^{11}C]-butyric acid, which can be fully broken down to [^{11}C]-CO_2 and water via fatty acid metabolism (DiVincenzo & Hamilton, 1979; Knapp et al., 1985).

1.3. PET physics and reconstruction

PET radioisotopes include unstable nuclei like ^{11}C and ^{18}F that undergo radioactive decay through the release of a high-energy particle called a positron, also called a beta particle (β^+). Below are the decay schemes for ^{11}C and ^{18}F:

$$^{11}_{6}C \xrightarrow{\beta^+} {}^{11}_{5}B \qquad\qquad {}^{18}_{9}F \xrightarrow{\beta^+} {}^{18}_{8}O$$

Although the β^+ decay from any given atom occurs randomly, each radioisotope has a characteristic rate of decay given by lambda (λ), which is inversely proportional to the half-life ($t_{1/2}$) of the tracer. The characteristic half-lives of ^{11}C and ^{18}F are approximately 20.3 and 109.8 minutes, respectively, and thus ^{11}C decays more rapidly.

When the β^+ interacts with any nearby electron within a tissue, the pair of particles undergo annihilation, in which they are converted into energy in the form of two, 511 keV photons that are approximately colinear, or 180 degrees, from each other. These photons are used to generate the PET image through two additional processes: (1) conversion to an electrical signal via arrival at and interaction with the PET detector module, and (2) the PET image reconstruction algorithm.

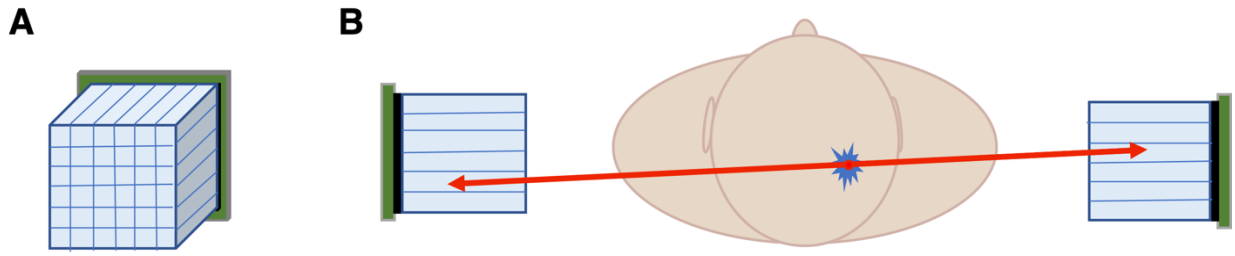

Figure 1.1: Simplified illustrations of a PET detector module and detection of a coincident event

Figure 1.1: Simplified illustrations of a PET detector module with a silicon photomultiplier (A) and the detection of coincident event by a pair of detectors (B), as adapted from figure 18-1 of *Physics in Nuclear Medicine* (Cherry et al., 2012). (B) shows the detection of colinear photons (red) after an annihilation event in the head of a subject injected with a positron-emitting

radiotracer. It is important to note that the photons will only be detected if both photons interact with the detector modules, demonstrating the importance of scanner geometry in improving system sensitivity (which is discussed in section 1.4).

The PET detector module is composed of a scintillation crystal and a photomultiplier (either photomultiplier tube or silicon photomultiplier). In the event that a photon interacts in a detector module, the high energy photon is converted into visible light within the scintillation crystal. This visible light is then detected by a photomultiplier, which amplifies the light output of the scintillation crystal and converts the deposited energy into an electrical signal. Once this signal, also referred to as a detected event or a count, is collected by the scanner electronics, its timing is compared with detected events recorded from opposing detectors. If two events occur approximately 6-12 nanoseconds (Cherry et al., 2012) apart, they are recorded as a coincident pair, and their timing and detector positions are recorded on a log known as a list-mode file. The PET image can then be reconstructed using the list-mode file. Alternatively, each event can be stored based on the angle of projection of the two detectors and the distance of the event from the center point in the form of a sinogram. Sinograms consist of rows of projections taken by rotating 180 degrees around the center of the FOV. However, this requires determining the temporal framing (how the scan acquisition length is divided into dynamic frames) prior to creating the sinograms, and is thus less flexible than list-mode representation of the data. The reconstructed image units are typically in terms of radioactivity concentration, such as counts per second per cubic centimeter, or Becquerels/cc (Bq/cc). For further details regarding the PET detectors and acquisitions, see Cherry *et al*. (2012) (Cherry et al., 2012).

PET reconstruction algorithms capitalize on the colinear nature of the 511 keV photons released by annihilation events. Analytical methods, such as filtered back-projection (FBP), or iterative processes such as ordered subsets expectation maximization (OSEM) generate an image reflecting the 3-dimensional (3D) localization of radiotracer activity in space. These reconstruction algorithms can also take advantage of time-of-flight (TOF) information. If the two annihilation photons arrive at colinear detectors at times t_1 and t_2, their position Δd relative to the midpoint of the line (called a line of response, or LOR) between the two detectors can be determined by the following: $\Delta d = c \cdot (t_2 - t_1)/2$, where c is the speed of light $3x10^8$ m/s (Cherry et al., 2012). Due to the additional time it takes within the scintillation crystal to convert the annihilation photons into visible light and detect that light, there is uncertainty in the measurement of t_1 and t_2, and thus uncertainty in Δd. Nonetheless, TOF information reduces the uncertainty in the position of the annihilation event, since a TOF probability distribution, or kernel, can be used during the reconstruction to constrain the location of events within a narrow region of the LOR, instead of allowing the events to occur over the entire LOR. However, there are many factors that affect the image quality and quantification, including the random alignment in time of photons that did not derive from the same annihilation event (called a random or accidental event), differences in detector sensitivity for detecting individual events, detector pulse pileup or deadtime, or the scatter of the 511 keV photons within the detectors or the body. Prior to or during the reconstruction process, corrections for these effects are applied to make the images as quantitatively accurate as possible.

1.4. Image quality trade-offs

The efficiency of a PET imaging system to account for as much of the available signal as possible is measured by the system sensitivity. Sensitivity is dependent on the source activity or emission

rate, the efficiency of each detector, the fraction of events that can be detected based on the geometric arrangement of the detectors (geometric efficiency), and the attenuation that occurs within the object (Cherry et al., 2012). For given crystal and geometric efficiencies, sensitivity can be affected by multiple aspects of the acquisition. Photons can be scattered in the tissue or detector modules and not be detected, and high activity levels can cause the electronics to become overwhelmed by the number of pulses detected, known as deadtime. Although physical factors such as positron range and non-collinearity of the resulting annihilation photons, as well as random and scattered coincidences, do not directly impact sensitivity, they can cause blurring of the images and reduce image contrast. Trade-offs can be made among the factors that affect sensitivity—in addition to the phenomena that affect image quality— to produce images of sufficient statistical quality for clinical and diagnostic use.

In addition to modifying the geometric efficiency of the scanner, the most straightforward way to increase image statistics would be to increase the amount of injected radioactivity or dose. Although this may increase the spatial resolution, this comes with increased radiation exposure to the subject, in addition to increased deadtime and random coincidences. Instead, the trade-off between higher image resolution and reducing the noise can be considered when the PET images are reconstructed. As discussed in the previous section, PET data for an entire scan session is acquired and saved as a list-mode file. This data can then be reconstructed as either a single static 3D image or broken up into segments over time to produce a 4-dimensional (4D) dynamic PET image series. The latter is used for quantitative kinetic modeling. This 4D image can have image frames with different temporal lengths, typically ranging from 5 or 10 seconds—to capture any changes in activity—out to a frame length of 5 minutes, as the tracer biodistribution stabilizes. Rapid changes in activity can be captured with shorter (e.g., < 2 s) frames, but can result in lower

image quality. Increasing the amount of radioactivity present and reducing the impact of noise in each 3D image voxel can be accomplished through either increasing the voxel size or increasing the frame lengths.

However, reduced spatial resolution can lead to increased partial volume effects (PVE), where the signals from anatomically distinct tissues are averaged together in the same image voxel, and, as will be discussed in chapters 2 and 3, reduced temporal resolution can negatively impact kinetic modeling and quantification. Recent improvements in scanner design have led to increases in sensitivity that have allowed for high spatiotemporal-resolution scanning with reasonable noise levels without sacrificing image resolution.

1.5. Significance of total-body PET

In previous generations of PET scanners, the imaging field of view (FOV) was limited to roughly 20 cm in the axial direction. Dynamic PET studies were limited to a single organ, such as the entire brain, since 20 cm is approximately the distance from the top of the head to just below the jaw line (figure 1.2A). With this limited FOV, one could focus on individual organs like the brain, or step the patient through the scanner FOV over the course of the scanning session. But with the advent of long axial FOV scanners such as the uEXPLORER, events throughout the entire body can be detected simultaneously with a higher sensitivity, since many more rows of detector modules are utilized, in addition to increasing the acceptance angle, which allows for a greater number of rows of the detectors to record coincidence events with each other (Badawi et al., 2019; Leung, Berg, et al., 2021; Spencer et al., 2021). Although no imaging modality is 100% sensitive, total-body PET systems are capable of a 40-fold gain in sensitivity over conventional commercially available PET scanners with short axial FOV (Poon et al., 2012; Spencer et al., 2021).

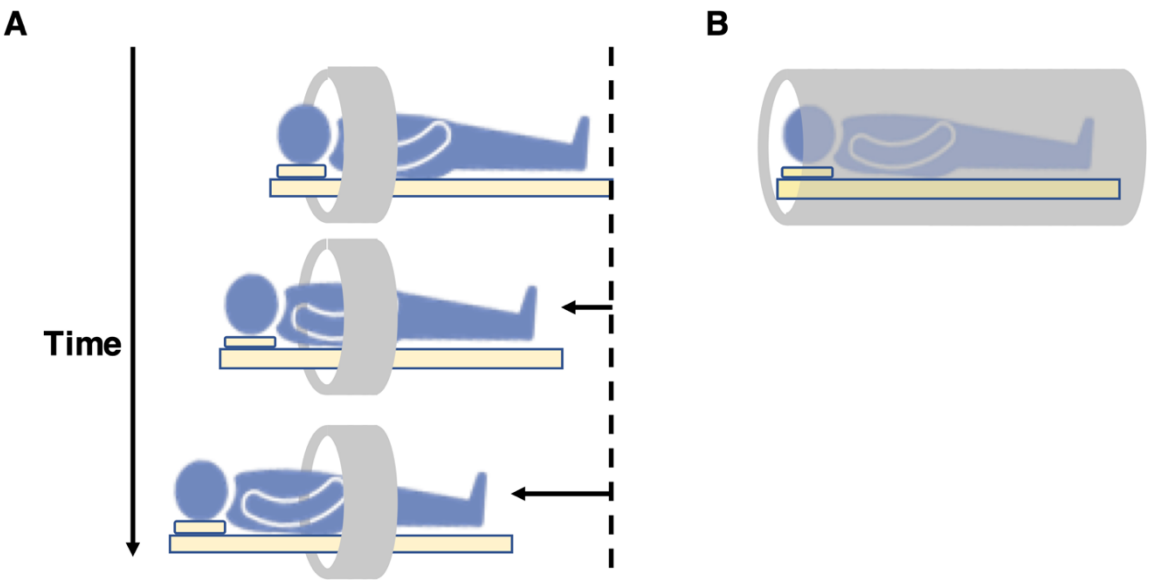

Figure 1.2: Whole-body PET versus total-body PET

Figure 1.2: Whole-body PET versus total-body PET. In (A), a whole-body PET acquisition requires stepping the subject through the scanner over time. The long axial FOV of total-body PET systems allows for the entire body to fit within the imaging FOV (B), allowing for all regions of the body to be imaged simultaneously.

The uEXPLORER scanner is made up of 8 rings of detector modules, reaching a bore length of nearly 2 meters (figure 1.2B). Most individuals can fit completely within the imaging FOV, allowing one to measure radiotracer uptake in all of the organs at once. For example, rapid changes in activity in the brain and heart due to the injection of a radiotracer bolus can be tracked at the same instance in time. Though tracking changes across different organs may not be important in every study, multi-site diseases such as metastatic cancer or diabetes can affect a wide range of tissues and may benefit from the increased FOV of total-body PET (Cherry et al., 2018). Additionally, radiation safety characterization of radiotracers with rapid changes in biodistribution or short half-lives is feasible with total-body PET, as will be demonstrated in chapter 5.

As discussed in more detail in the next section, quantitative PET kinetic modeling can be performed using an input function (IF) and the uptake and clearance of radiotracers, as measured by the tissue time-activity curve (TAC), to estimate changes in parameters such as perfusion and other metabolic rates. But a major hurdle to the quantification of parameters via PET kinetic modeling is that it requires measuring the radiotracer activity concentration in the blood, in addition to that of the tissue itself. Measurement of the IF is traditionally done by drawing arterial blood samples from the radial artery, a process that is considered safe (Everett et al., 2009), but is nonetheless invasive. Additionally, some organs have unique relationships to their blood pool. For example, the liver is perfused by both the portal vein and the hepatic artery, and would also require accounting for the activity from the portal vein in addition to the radial artery either by measuring the activity in the portal vein from the images, or as part of the modeling process. The uEXPLORER's long axial FOV allows for the measurement of an image-derived input function (IDIF) from large, central blood pools in the aorta and cardiac ventricles non-invasively, directly from the images themselves. Additionally, with a spatial resolution of approximately 3 mm (Spencer et al., 2021), IDIF blurring due to motion and partial volume effects (PVE) are reduced compared to IDIF measurements with scanners from previous generations. The narrow axial FOV of these older scanners requires using an IDIF from small vessel—often fraught with motion and PVE—that can be captured in the same bed position as the tissue of interest, or through invasive measures such as arterial sampling (Bohm et al., 1988), making quantitative PET kinetic modeling challenging to execute routinely without a long axial FOV scanner like the uEXPLORER.

1.6. Dynamic PET

As discussed in section 1.3, PET images represent the concentration of radioactivity in each voxel, generally with units Bq/cc. However, a common method of standardizing the pixel values is to use

the standardized uptake value (SUV) (Lucignani et al., 2004). SUV normalizes the activity in the images by the injected dose and body weight of the subject. SUV can be determined from a static PET image and is considered a semi-quantitative metric that is dependent on the way in which the tracer behaves within the body, as well as on the uptake time, or how long after injection the static image is acquired. High SUVs for FDG PET are indicative of increased glucose metabolism, as might be the case in inflamed tissues and cancerous lesions. However, as noted in section 1.2, FDG is nonspecific to any particular disease or pathology; it simply reflects glucose delivery, transport into the cells, phosphorylation, and clearance, which are unique to each individual tissue and also depends on the uptake time (Chin et al., 2009). Therefore, it is important to perform the static acquisition at the optimal scan time post injection, i.e., after the tracer has had time to accumulate, but before it washes out of the tissue of interest.

Alternatively, dynamic imaging can also be performed, which allows for the assessment of radiotracer uptake over time. Serial PET images acquired dynamically allow for quantitative kinetic modeling to be performed. After a subject is placed in the scanner, for example, dynamic studies can be performed to visualize and track the distribution of the radiotracer bolus into the blood pool and its delivery into tissues throughout the body. The radiotracer tissue TAC can then be measured from any tissue of interest. The uptake and distribution of a radiotracer can occur rapidly, and unfortunately, depending on the scanner geometry, the temporal gaps between successive frames can be too large to adequately sample multiple region TACs. This is an issue with whole-body PET kinetic modeling with limited axial FOV scanners, where as depicted in figure 1.2A, the subject must be stepped through the scanner to acquire a single whole-body image. In order to acquire a dynamic dataset, multiple timepoints per positioning step are needed, and the subject must be cycled through the scanner FOV multiple times.

In addition to the tissue TAC, the radioactivity concentration in the plasma, or plasma IF, is often needed for kinetic modeling. As discussed briefly in the previous section, the traditional method of acquiring an IF is to take many samples of arterial blood from the radial artery in the wrist during the study. This procedure is invasive to the subject, and requires additional expertise and hardware for measuring the plasma radioactivity in each blood sample drawn from the subject. The IDIF is a non-invasive alternative to arterial sampling that can be easily measured in total-body PET images from a variety of blood pool locations such as the right ventricle, left ventricle, aortic arch, and descending aorta. However, since the IF represents the activity concentration in whole blood it must be converted to the plasma concentration for kinetic modeling. In section 1.7.1, foundational concepts regarding compartment modeling will be addressed. Then, in section 1.7.2, corrections such as the conversion of whole-blood to plasma and additional corrections to the IF that build on section 1.7.1 will be discussed.

1.7. Kinetic modeling

1.7.1. Compartment models and other relevant modeling methods

As discussed in the previous section, semiquantitative metrics such as SUV are utilized for clinical assessments of disease. SUV represents the static assessment of the radiotracer distribution at a pre-determined time. SUV images for FDG, for example, are typically acquired 60 to 90 minutes post injection. However, the PET radiotracer distribution is a dynamic process that depends on delivery, uptake, binding, and clearance of the tracer over time. Thus, there is additional uncertainty associated with SUV when assessing disease status, which has been demonstrated in relation to assessment of coronary artery disease, cancer, and receptor binding studies (Lammertsma, 2017). Quantitative kinetic modeling can reduce this uncertainty; through the measurement of the plasma IF and a tissue TAC over the course of the dynamic study, these rates

of uptake, transport or binding, and clearance of the tracer to tissues of interest can be estimated using compartment modeling. In compartment modeling, each compartment represents a different physical or chemical state of the radiotracer, rather than spatial location alone. The number of compartments—and therefore the complexity of the model—is dependent on the radiotracer and associated mechanisms being studied. The models for [^{11}C]-butanol and FDG typically have one and two tissue compartments, respectively. To align with the order of the subsequent chapters, FDG and two-tissue compartment modeling will be discussed first.

A two-tissue compartment model can be represented by two compartments where distinct processes occur. For FDG, the following occurs: (1) bidirectional transport and uptake of the tracer between the plasma and the cells in tissue (C_{free}) and (2) phosphorylation of FDG within the cell (C_{met}), as shown figure 1.3.

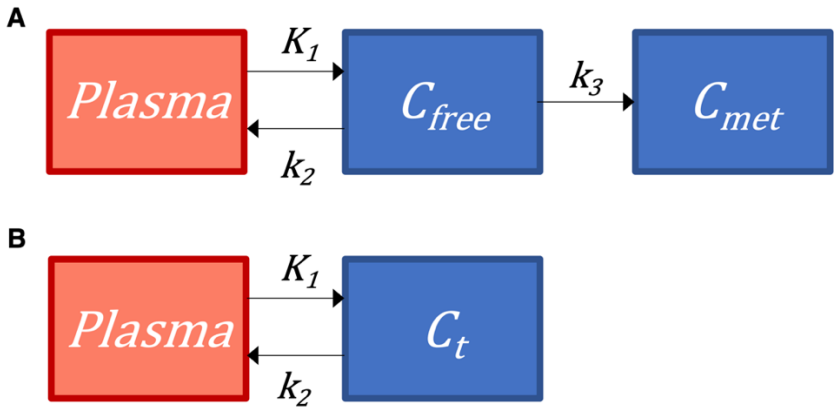

Figure 1.3: Tissue compartment models implemented in this work

Figure 1.3: Tissue compartment models implemented in this work. Two-tissue compartment model was implemented for FDG (A), where the phosphorylation of FDG by hexokinase is considered irreversible. K_1 represents the blood-to-tissue rate of transport of FDG, and has units ml plasma/min/ml tissue, or ml·min^{-1}·cm^{-3}. k_2 has units of min^{-1} and reflects the transport of unphosphorylated FDG back into the blood pool. k_3 (units min^{-1}) is the rate at which FDG is

phosphorylated by hexokinase and then is trapped in the cell. The reverse rate, which would be called k_4 (units min^{-1}), is not shown, since the rate of dephosphorylation is very small and challenging to measure, and thus is assumed to be negligible (Gallagher et al., 1978; Huang et al., 1980). A one-tissue compartment model is appropriate for [^{11}C]-butanol (B), since [^{11}C]-butanol is considered freely diffusible across the cell membrane.

It is important to note that compartment modeling relies on the following key assumption: the tracer concentration in each different tissue compartment is homogenous at any given time, meaning that instantaneous mixing of the tracer within each compartment is assumed. If homogeneity can be assumed, then the activity in each compartment can be modeled as the convolution of the plasma IF with its impulse response function. For FDG, change in the compartment concentrations of C_{free} and C_{met} over time can be represented by a series of linear ordinary differential equations:

$$\frac{dC_{free}(t)}{dt} = K_1 C_p(t) - (k_2 + k_3) C_{free}(t) \tag{1.1}$$

$$\frac{dC_{met}(t)}{dt} = k_3 C_{free}(t) \tag{1.2}$$

which can be solved by least-squares methods for individual parameters (Gunn et al., 2001; Watabe et al., 2006) using a TAC measured from the dynamic images (C_T):

$$C_T(t) = (1 - v_b)(C_{free}(t) + C_{met}(t)) + v_b C_b(t) \tag{1.3}$$

C_p is the plasma IF, K_1 (units ml/min/ml or $ml \cdot min^{-1} \cdot cm^{-3}$) is the transport rate constant from the blood into the cell, k_3 represents the rate of phosphorylation of FDG into FDG-6P with units min^{-1}, and k_2 (min^{-1}) represents the return of unphosphorylated FDG to the blood pool. $C_b(t)$ denotes the whole blood TAC and is commonly approximated by $C_p(t)$ for FDG. Correction for the blood volume fraction present in the tissue space v_b will be discussed in further detail in section 1.7.2.

The rate of dephosphorylation of FDG-6P within the cell, which would be called k_4, is not shown in figure 1.3, since it is challenging to estimate due to its small magnitude, and is assumed in this work to be negligible (Gallagher et al., 1978; Huang et al., 1980). The parameter estimates of the two-compartment model can then be obtained through non-linear least squares fitting (G. Wang & Qi, 2009), and can be combined to determine the net influx rate, K_i (ml/min/ml or ml·min^{-1}·cm^{-3}). K_i accounts for both net transport into the tissue (K_1 and k_2) and FDG trapping (k_3), and is equal to $K_1k_3/(k_2+k_3)$.

In addition to compartment modeling, additional analysis methods can be used to assess FDG kinetics. In this work, Patlak graphical analysis was implemented. Patlak graphical analysis can be performed for tracers like FDG where the tracer is assumed to be irreversibly trapped (Gjedde, 1982; Patlak et al., 1983; Patlak & Blasberg, 1985; Rutland, 1979) but has the advantage of being independent of the assumed compartment model structure. Patlak analysis can be used to derive the net influx rate of FDG, known as K_i, for tissue TAC C_t by determining the slope of the equation:

$$\frac{C_t(t)}{C_p(t)} = K_i \frac{\int_0^t C_p(\tau)d\tau}{C_p(t)} + V, \qquad t > t^*. \tag{1.4}$$

Equilibrium must be reached after time t^*, such that the resulting plot from equation 1.4 becomes linear for $t > t^*$. For the linear portion of the plot, the slope is K_i. The intercept V is related to the initial volume of distribution, or ratio of tissue to blood concentrations at equilibrium. It is important to note that the fractional blood volume v_b within the tissue space is not accounted for in equation 1.4 for Patlak modeling, and thus will impact the estimate of K_i, particularly for large values of v_b. For compartmental modeling, v_b can be accounted for as part of the fitting process, which will be discussed in more detail in section 1.7.2. Both 2-tissue compartment modeling and Patlak graphical analysis will be used in the analysis of FDG dynamic datasets in chapter 3.

Chapters 4 and 5 focus on [^{11}C]-butanol. Here, relevant methods of analysis for perfusion tracers like [^{11}C]-butanol will be discussed. Whole-brain cerebral blood flow using an inert gas was first assessed by Kety and Schmidt (1947). This was based on the Fick principle, where the change in tissue concentration C_t can be written as a mass-balance equation:

$$\frac{dC_t(t)}{dt} = K_1(C_a(t) - C_v(t)) \tag{1.5}$$

where C_a is the arterial inflow, C_v is the venous outflow, and K_1 is blood flow with units of ml/min/ml or ml·min^{-1}·cm^{-3}. Equation 1.5 can be solved for blood flow by finding the integral of both sides and rearranging:

$$K_1 = \frac{C_t(t)}{\int_0^t C_a(\tau) - C_v(\tau) d\tau}. \tag{1.6}$$

For dyes or inert gasses such as nitrous oxide that were used for the foundational paper in this field (Kety & Schmidt, 1947), it was not possible to measure the brain tissue concentration C_t directly. But by reaching an equilibrium state at time t_e, the partition coefficient ρ, mathematically equivalent to the volume of distribution of the tracer, can have an assumed value of the ratio of the tissue and arterial concentrations at equilibrium ($C_t(t_e)/C_a(t_e)$), and thus the measurement of CBF depended solely on the equilibrium arterial and venous concentrations:

$$K_1 = \frac{\rho C_a(t)}{\int_0^t C_a(\tau) - C_v(\tau) d\tau}. \tag{1.7}$$

Assuming equilibrium is reached, equation 1.5 can be solved using Laplace transforms to obtain the following:

$$C_t(t) = K_1 C_p(t) \otimes e^{-(K_1/\rho)t}. \tag{1.8}$$

Equation 1.8 is very similar to the equation for one-tissue compartment model (figure 1.3B):

$$C_t(t) = K_1 C_p(t) \otimes e^{-k_2 t}. \tag{1.9}$$

Thus, by comparing equations, the partition coefficient is also equal to K_1/k_2 for a one-tissue compartment model. When accounting for the blood volume fraction present in the tissue, equation 1.9 can be written:

$$C_t(t) = (1 - v_b)K_1 C_p(t) \otimes e^{-k_2 t} + v_b C_b(t). \tag{1.10}$$

Once in this form, non-linear least squares regression can be used to solve for K_1 and k_2 in a similar manner to the two-tissue compartment model for FDG.

As an alternative to solving the compartment model via non-linear least squares, ρ can be assumed to have a specific value, as is done for PET autoradiographic methods (Herscovitch et al., 1983; Raichle et al., 1983). PET autoradiography (ARG) traditionally utilizes static acquisitions, where the coincident events across the entire acquisition time are used to estimate the area under the curve (AUC) for each voxel. Dynamic PET can be utilized for ARG methods by taking the integral for each TAC C_t:

$$AUC = \int_0^t C_t(\tau)\, d\tau \tag{1.11}$$

where τ represents the time of integration. An AUC lookup table can be generated for a wide range of K_1 values, and then K_1 can be estimated by determining the K_1 that provides the closest AUC to that of the measured C_t. Although ARG is more computationally efficient, only K_1 can be estimated, while assumptions about the partition coefficient and integration time must be made prior to determination of K_1. While the partition coefficient for [^{11}C]-butanol has been investigated previously in the brain (Gjedde et al., 1980), its value in other organs is unclear. The integration time must also be carefully decided, since freely diffusible perfusion tracers such as [^{11}C]-butanol can washout of the tissue quickly, leading to the underestimation of K_1 for too long of scan times (Sage et al., 1981). Additionally, dispersion and delay of the input function can lead to large biases in autoradiographic perfusion estimates (H. Iida et al., 1986). Applying autoradiographic

techniques across the many organs of interest in total-body PET datasets, without knowledge of partition coefficients, integration times, and delay and dispersion correction of the input function, is likely prone to significant error. Thus, for this work, we focused on the non-linear least squares solution of equation 1.10 to accurately estimate K_1 and k_2 for [^{11}C]-butanol studies.

One important factor not yet discussed is extraction, or the ability of the tracer to cross out of the arterial inflow into the tissue space. The Renkin-Crone model of the capillary is a cylindrical tube which describes the flow (F) of the tracer through the capillary (Crone, 1963; Renkin, 1959). Extraction of the tracer into the tissue is based on the permeability-surface area product (PS):

$$E = 1 - e^{-PS/F}. \tag{1.12}$$

PS is dependent on both the vessel wall permeability to the tracer used, as well as the capillary surface area (figure 1.4). Small, non-polar lipophilic tracers such as [^{11}C]-butanol and [^{15}O]-O_2 have high permeability because they pass easily through the cell membranes, while larger or hydrophilic molecules must pass through gaps in the endothelium or must be transported (as is the case for FDG) via facilitated diffusion across the vessel wall. If blood flows through a tissue at a flow rate F, the observed K_1 or clearance to the tissue is the product of the extraction and flow rate EF. For tracers explicitly used to measure flow (e.g., [^{15}O]-water), high flow rates or low PS will lead to the underestimation of flow due to a lower K_1 relative to a tracer that might be more highly extracted (figure 1.4).

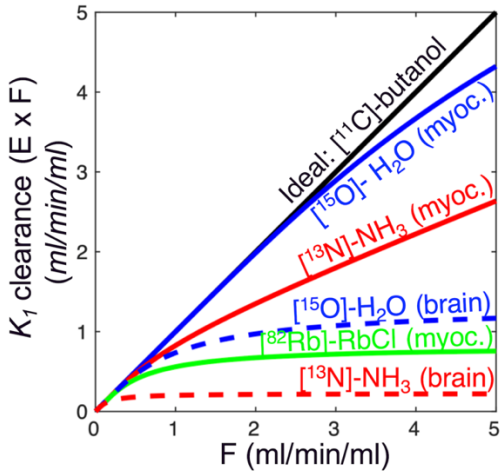

Figure 1.4: Blood flow F (ml/min/ml) versus K_1 clearance (ml/min/ml).

Figure 1.4: Blood flow F (ml/min/ml) versus K_1 clearance (ml/min/ml). Based on the Renkin-Crone model (equation 1.12), the permeability surface area products for several cerebral and myocardial perfusion scenarios were determined based on previous literature (Berridge et al., 1991; Glatting et al., 1997; Hack et al., 1983; Herscovich et al., 1987; Phelps et al., 1981; Schelbert et al., 1981).

This underestimation of blood flow F via K_1 among the different tracers in across tissue types is important for perfusion tracers, which focus on quantification of blood flow through estimation of K_1. One of the strengths of [^{11}C]-butanol is that it has been shown to have an extraction fraction of ~1 even at high flow rates in the brain (Hack et al., 1983; Herscovich et al., 1987; Knapp et al., 1985). Commonly used perfusion tracers such as [^{15}O]-water (Herscovich et al., 1987; Raichle et al., 1976), as well as [^{13}N]-ammonia and [^{82}Rb]-RbCl (Maddahi & Packard, 2014), show underestimation of clearance at flow rates greater than 0.8 ml/min/ml in the myocardium, and 0.6 ml/min/ml in the brain (figure 1.4). Thus, for this work, E is assumed to be equal to 1 for [^{11}C]-butanol, and the terms blood flow, perfusion and K_1 are used interchangeably in reference to [^{11}C]-

butanol. In chapter 4, one-tissue compartment modeling is used to measure perfusion using this tracer at a variety of flow rates in the body.

1.7.2. Quantitative corrections to the input function

In addition to considering how the tracer interacts with the tissue (uptake, metabolism, clearance), kinetic modeling also relies critically on the plasma time-activity curve $C_p(t)$. Thus it is important to note that many quantitative corrections to the IF curve can be applied prior to or as part of the modeling process, including corrections for: whole blood to plasma ratio, metabolites, blood volume fraction, delay, and dispersion.

Blood consists not only of plasma, but also proteins, leukocytes, and erythrocytes. Since the tissue can only interact with free radiotracer in the plasma and not that which is taken up into erythrocytes or bound to plasma proteins, a TAC derived via a region of interest (ROI) within the blood pool may not represent the true activity concentration of the IF. Thus, it is common to scale the IF based on the radiotracer concentration ratio φ between plasma and whole blood:

$$C_p(t) = \varphi(t)C_b(t). \tag{1.13}$$

In the case where there is little uptake by erythrocytes, the plasma curve C_p can be recovered by scaling the whole blood IF C_b by the relative plasma to blood ratio, or division by 1 minus the hematocrit (HCT), where the nominal HCT is approximately 0.45 (Billett, 1967). If there is uptake into the erythrocytes, then this ratio has the potential to change over the course of the scan. For example, [^{11}C]-butanol is taken up rapidly into erythrocytes that exhibit a φ of approximately 1 (Knapp et al., 1985). However, for some tracers, φ is time-dependent rather than a constant scaling factor. For FDG for example, glucose is the primary source of energy for erythrocytes. Therefore, initial FDG transport into erythrocytes occurs rapidly (Gambhir et al., 1989) and φ is approximately 1.09 after the bolus is injected (Hinz, 2012; Naganawa et al., 2020). However,

erythrocytes have low but non-negligible metabolic demand, and only some of the FDG that is transported into the erythrocytes are actually phosphorylated and trapped. Thus, this ratio gradually drops to 1.05 after 60 minutes (Feig et al., 1972; Hinz & Turkheimer, 2006; Lowe & Walmsley, 1986; Naganawa et al., 2020). For this work, the appropriate correction factor φ can then be applied depending on the radiotracer:

$$C_p(t) = \varphi(t)C_b(t), \qquad \varphi(t) = \begin{cases} 1 & : [^{11}C] - butanol \\ 1.09 + r_s C_b(t) & : FDG \end{cases} \tag{1.14}$$

where r_s (units 1/s) is equal to the rate of FDG sequestration by erythrocytes, which was set to (1.05-1.09)/3600, or -1.1x10^{-5}. Example plasma and whole blood curves for FDG are shown in figure 1.5.

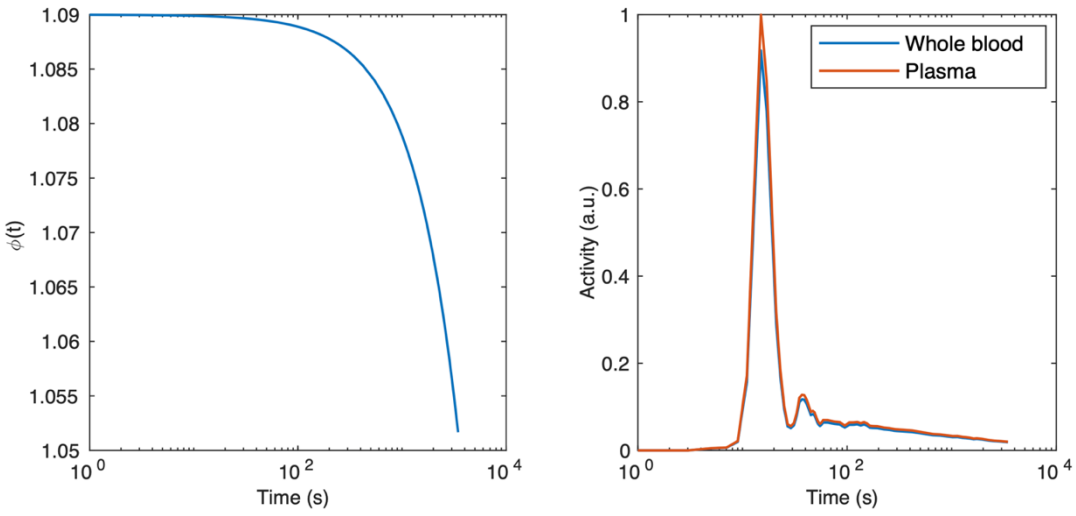

Figure 1.5: Example of whole blood to plasma correction for FDG

Figure 1.5: Example of whole blood to plasma correction for FDG. $\varphi(t)$ from equation 1.13 (left) was multiplied by the whole blood TAC (right, blue curve) derived from the descending aorta to obtain the plasma concentration (right, orange curve). Note that the x-axis is shown in

logarithmic scale for better visualization of the change in $\varphi(t)$, and that the right curves were scaled to the maximum value of the plasma curve for visual comparison.

In addition to correcting the IF function curve for differences between the free concentration in plasma versus whole-blood, metabolite correction may be necessary. Metabolites are the products of the breakdown of the radiotracer in the body. When these metabolites are released into the blood, any metabolite with a radioisotope label can alter the apparent concentration of the original unmetabolized radiotracer, called the parent tracer, as measured by the PET scanner. The relative amounts of these products in the blood over time, called the metabolite fraction, is obtained through blood sampling and chromatography. The metabolite fractions obtained via blood sampling can be fit to a model to match the sampling rate of the images. Then, metabolite correction can be performed by subtracting the metabolite fraction from the parent IF curve.

Like most other radiotracers, [^{11}C]-butanol has metabolites that have the potential to impact IF quantification. Potential metabolites of [^{11}C]-butanol include [^{11}C]-CO_2, [^{11}C]-butyric aldehyde, and [^{11}C]-butyric acid (DiVincenzo & Hamilton, 1979; Knapp et al., 1985). [^{11}C]-butanol is metabolized similarly to ethanol, and thus can be metabolized in the liver or undergo fatty acid esterification in the pancreas (Carlson, 1994; DiVincenzo & Hamilton, 1979; Manautou & Carlson, 1991). However, these processes occur slowly enough that metabolites are not detected in the first 3.5 minutes (Knapp et al., 1985) and thus do not affect first-pass perfusion imaging. For illustrative purposes, an example metabolite correction curve was generated based on the model used by Gunn *et al*. in the monitoring of the metabolite [^{11}C]-CO_2 in the blood after intravenous injection of [^{11}C]-thymidine (Gunn et al., 2000), where the fraction of metabolites in the plasma f_{met} over time is:

$$f_{met}(t) = \begin{cases} 0 & t \leq 3.5\ min \\ \alpha(1 - e^{-\beta(t-d)}) & t > 3.5\ min \end{cases} \quad (1.15)$$

where α was set to 0.7, β was set to 0.005, and the delay d was set to 3.5 minutes. The corrected plasma curve is then equal to (1-f_{met}) x C_p. The resulting metabolite-corrected plasma IF is shown in orange in figure 1.6. In this case, metabolite correction does not affect the first pass of the tracer, but by 8 minutes into the study, 50% of the activity in the blood represents the metabolite [^{11}C]-CO_2. Although the knowledge of such a curve would allow for longer time periods to be used for kinetic modeling of [^{11}C]-butanol, the metabolite fraction curve in figure 1.6 is a simulated result based on the metabolite curve of a different tracer, and implementation of such a curve would require performing a validation study with blood sampling using [^{11}C]-butanol. This study therefore focuses on modeling over the first pass of the tracer, when metabolites from [^{11}C]-butanol can be considered negligible.

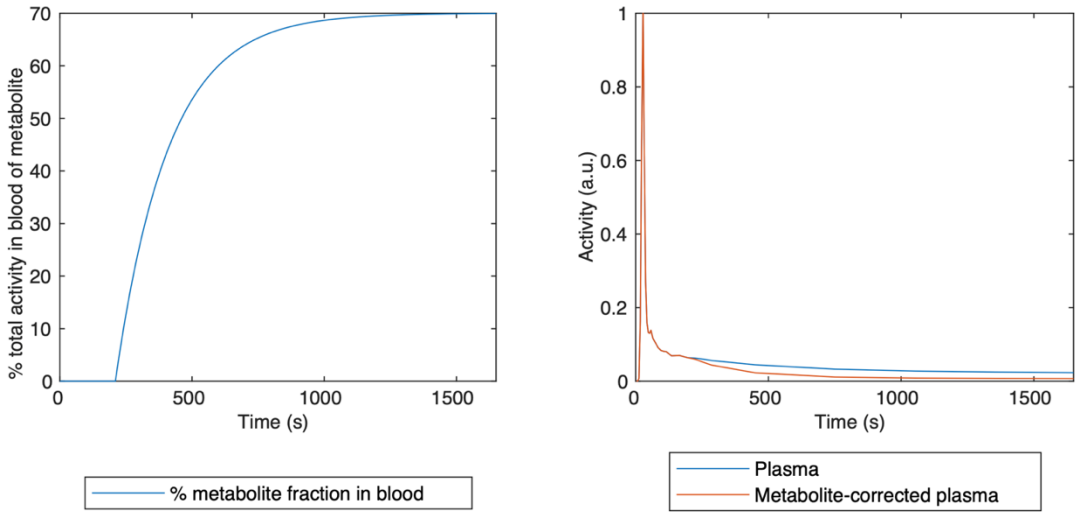

Figure 1.6: Example of metabolite fraction in the blood and corrected plasma IF

Figure 1.6: Example of metabolite fraction in the blood (left) and corrected plasma IF over time (right, orange). The metabolite fraction model implemented here was designed such that no metabolite formation occurred prior to 3.5 minutes. Such a metabolite-corrected plasma curve on

the right (orange) could in principle be used for kinetic modeling with longer acquisition times for [^{11}C]-butanol.

In the case of FDG, corrections for metabolites are well-understood: since the phosphorylated FDG6P is irreversibly trapped within the cell (Phelps et al., 1979; Sokoloff et al., 1977), no additional metabolites are present in the plasma fraction of whole blood. Therefore, correction of the IF only requires correction of the plasma to whole-blood ratio as discussed above.

Regardless of the tracer used, corrections for blood volume fraction, delay, and dispersion must also be considered. Although the impact of these corrections differs depending on the tissue type, figure 1.7 demonstrates the importance of each of these factors in estimating liver perfusion with [^{11}C]-butanol. The parameter estimates for each scenario are included in table 1.1. Each of these corrections will be discussed in further detail, starting with blood volume fraction.

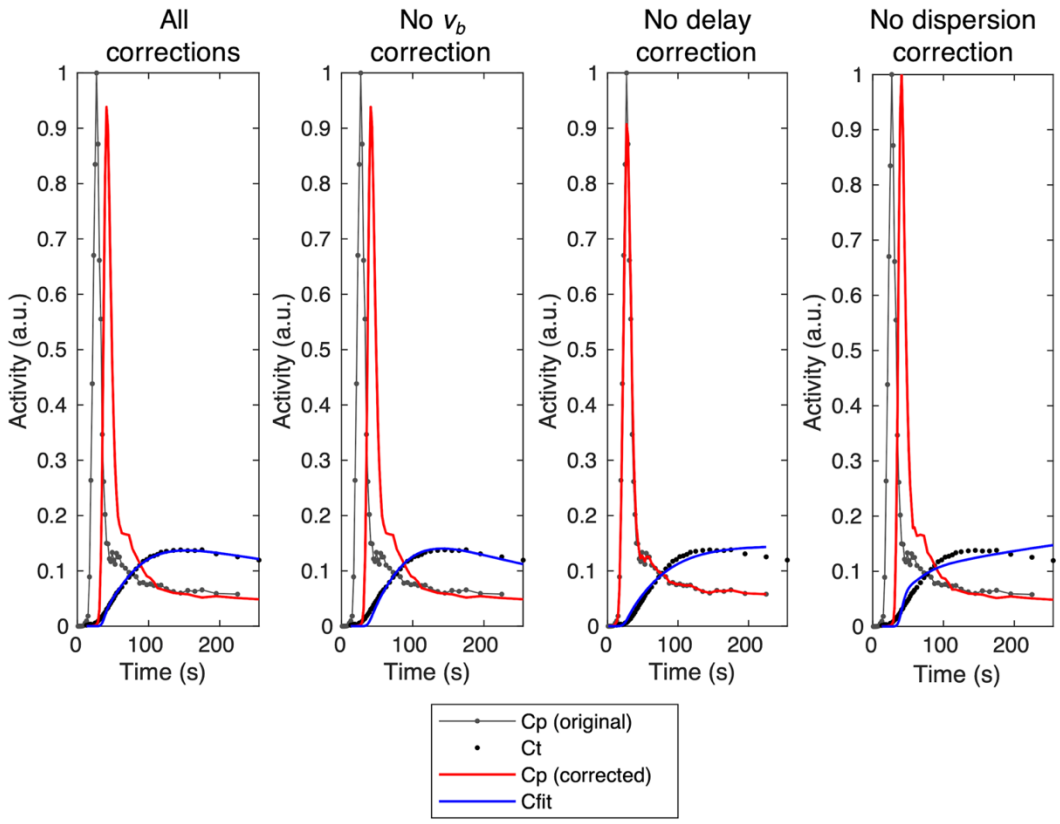

Figure 1.7: Impact of blood-based corrections on liver [^{11}C]-butanol TAC quality of fit

Figure 1.7: Impact of blood-based corrections on liver [^{11}C]-butanol TAC quality of fit. In the plots shown above, the original IDIF derived from the descending aorta is shown (Cp (original)), along with the measured activity concentration in the tissue (Ct), which in this example is the liver. Various combinations of corrections were applied to the corrected plasma curve (Cp (corrected)). The resulting fitted tissue curve (Cfit) is shown.

The first correction of interest is for blood volume fraction, or v_b. Although large vessels can be avoided when drawing ROIs, small blood vessels such as arterioles and venules cannot be avoided. These small vessels can contribute to the apparent tissue concentration, particularly in organs where the blood volume fraction is high, such as in the lungs and liver. To account for this, equations 1.3 and 1.10 above also include blood fraction v_b, such that it is included as part of the

fitting process. As seen in figure 1.7, there is slight underestimation of liver activity during both the early phases and later time frames when v_b is ignored. This results in a higher K_1 by 13.5% relative to when all corrections were applied (table 1.1).

Table 1.1: Impact of blood-related corrections for [^{11}C]-butanol perfusion in the liver

Parameter	All corrections	No v_b corr.	No delay corr.	No dispersion corr.
v_b	0.069	0.0	0.0	0.0
K_1 (ml·min^{-1}·cm^{-3})	0.658	0.747	0.559	0.360
delay (s)	14.0	14.0	0.0	14.0

After an intravenous bolus injection, the bolus travels through the veins, right ventricle, and lungs prior to entering the arterial blood supply. This pass through the lungs leads to internal dispersion or blurring of the IF. Further, there is internal time delay; delay occurs not only prior to the arrival of the bolus into the arterial blood supply where an IDIF may be measured (e.g., left ventricle or descending aorta), but also between the IDIF sampling location to its arrival into a tissue of interest, such as the brain. For studies involving an arterial blood sampling system, external delay and dispersion due to the sampling site (e.g., the radial artery in the wrist) and the additional system tubing (Bohm et al., 1988), can lead to larger delay and dispersion correction factors (H. Iida et al., 1986) than those occurring internally. However, even with an IDIF, as used in this work, there is delay and dispersion within the subject. This can be seen in the example IDIFs for [^{11}C]-butanol shown in figure 1.8, where there is a shift in time and slight lengthening of the bolus with longer delay times. Without delay or dispersion correction, the fit of the liver TAC in figure 1.7 is poor and results in the underestimation of K_1 by 15.0% without delay correction, and 45.3% without dispersion correction, and v_b is underestimated by 100% without delay or dispersion correction (table 1.1).

Although delay correction will be discussed in further detail in chapter 3, it is important to note that the mismatch of the IDIF and true IF to a tissue can cause poor fitting of the data. This is

shown in figure 1.7 and table 1.1, where the poor fit when delay correction was not performed resulted in a 15% drop in K_1 relative to when all corrections were included. More specifically, errors in accounting for the IDIF delay and dispersion can cause large biases in the resulting parameter estimates (H. Iida et al., 1986; E. J. Li et al., 2021). Delay correction can be performed by shifting the IF over time, while dispersion can be accounted for via deconvolution of the IF with an exponential function (H. Iida et al., 1988; Ito et al., 2001). It is important to note that the liver is a special case, where dispersion of the IF is severe due to the passing of blood through the gastrointestinal tract and mesentery prior to arrival at the liver. Thus, a lack of dispersion correction for the liver greatly impacted the estimate of K_1 (45.3% decrease) in figure 1.7. Nonetheless, these correction factors all caused a shift in the estimated K_1 by greater than 10% and must be carefully considered across tissue types.

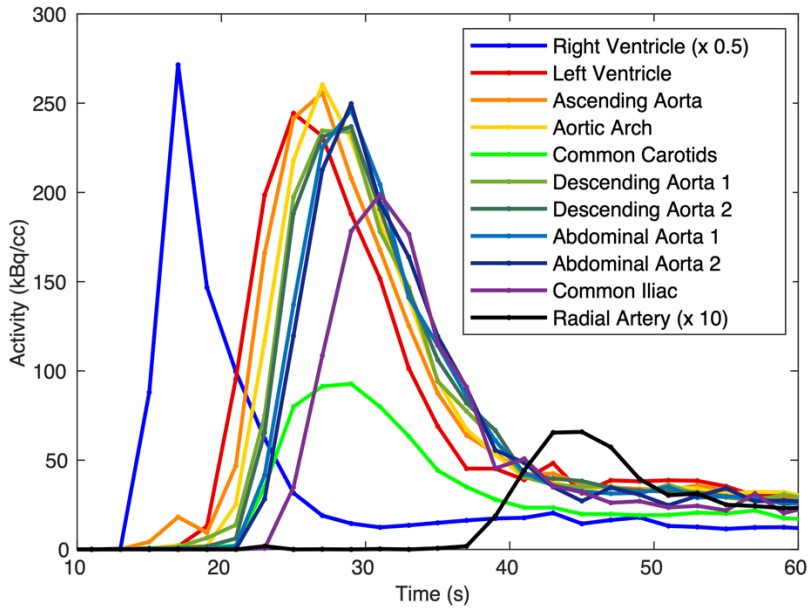

Figure 1.8: [^{11}C]-butanol IDIFs across the blood pool

Figure 1.8: [^{11}C]-butanol IDIFs across the blood pool. The delay in the bolus arrival across the IDIFs can be identified from the differences between the start of the rising edges of the arterial IDIFs in the central blood pool, which approximately ranges from 18 to 22 seconds for this

acquisition. Due to the small diameter of the carotids and radial artery, partial volume effects lead to reduced peaks for these IDIFs. For improved visualization of the differences between the IDIFs in this plot, the right ventricle IDIF was scaled by a factor of 0.5, and the radial artery IDIF was scaled by a factor of 10. A temporal frame length of 2 seconds was used for the dynamic reconstruction of the image dataset used to obtain the IDIFs shown here.

Figure 1.8 also illustrates the substantial internal delay experienced by the radial artery, which was approximately 20 seconds relative to the left ventricle IDIF. Dispersion of the radial artery IDIF may also occur, based on the flatter slope of the rising edge as compared to IDIFs derived from the ventricles or descending aorta. However, since the radial artery diameter is approximately 2.7 mm (Wahood et al., 2022) and the uEXPLORER spatial resolution is approximately 3 mm (Spencer et al., 2021), partial volume effects play a role in the shape of the radial artery IDIF in figure 1.8. Although automatic blood sampling systems are traditionally used for quantitative kinetic modeling, they tend to sample from the radial artery, and thus measure the IF with the internal delay and dispersion shown in figure 1.8, as well as the dispersion and delay that occurs within the blood sampling system. Automatic blood sampling systems require corrections for delay that are larger in magnitude and further complicated by the dependence on the sampling system, and must include dispersion correction. In this work, a blood sampling system was not used as a ground truth; instead, emphasis was placed on correcting the IDIFs derived from large blood pools (e.g., the left ventricle or descending aorta) for internal delay, since they produced similar curve shapes across sampling locations. The impact of IDIF sampling location will be discussed in further detail in section 2.5.

1.7.3. Evaluation of modeling results

In sections 1.7.1 and 1.7.2, relevant compartment models and corrections to the input function are discussed. However, a quantitative metric is needed to evaluate whether these models and corrections are appropriate to apply in various scenarios. One example is the liver, which receives blood from both the hepatic artery and portal vein, and thus requires consideration of a second blood input function (Zuo et al., 2019). Further, the blood from the portal vein is collected from the vessels leaving the gastrointestinal tract, spleen, pancreas, and gallbladder. Thus, prior to entering the liver, the portal vein blood experiences dispersion. As shown in figure 1.7, fitting of the liver curve with the proper assumptions improves the fitting process. Quantitative assessment of the quality of the model fit can be performed using a variety of criteria, including the F-test, the Akaike information criterion (AIC), the Schwarz criterion, and the Bayesian information criterion (BIC). In this work, the AIC with a correction for small sample sizes was implemented as follows:

$$AIC = M \cdot \ln\left(\frac{WRSS}{M}\right) + 2N + \frac{2N(N+1)}{M-N-1}, \quad WRSS = \sum_m^M w_m (c_{m,fit} - c_m)^2 \tag{1.15}$$

where M is equal to the number of frames, N is the number of estimated parameters in the model, and WRSS is the residual sum of squares. For the WRSS, w_m represents a weighting factor, which in this work is equal to 1, and c_m and $c_{m,fit}$ represent the measured TAC and fitted model result respectively.

1.8. Qualities of a good radiotracer

As discussed above, there are many important corrections that are required prior to obtaining quantitative measures of radiotracer kinetics. The use of a radiotracer that is specific to the physiological process of interest is key, as the image contrast of PET studies is based on a number of factors, including any delivery, transport, metabolism, binding, and clearance of the tracer in

the body. Ideally a tracer exhibits high specificity for the process of interest, limited recirculation of metabolites, or has metabolites that do not interact with the tissue of interest over the course of the dynamic acquisition. Having to perform fewer data corrections may improve upon the accessibility of quantitative modeling metrics for clinical use, to improve upon the reliability of clinically implemented imaging metrics. Since high temporal resolution dynamic PET images of the entire body can be generated with a total-body PET system, these qualities should ideally apply to the majority of organs throughout the body. Additionally, the half-life of the radioisotope is an important factor to consider for practical scan considerations. Because the half-life of carbon-11 (20 mins) is 10 times that of oxygen-15 (2 mins), the cyclotron for carbon-11 based radiotracers need not be on the immediate premises, but must still be in close proximity to the scanner. The 109.8-minute half-life of fluorine-18 allows for further flexibility and distance from a cyclotron. For a review on some of these qualities as they relate specifically to neuroimaging, see Ametamey, Honer, and Shubiger (2008).

1.9. Flow-metabolism coupling mismatch

This work focuses on the measurement of [^{11}C]-butanol perfusion (K_1) and FDG metabolism (K_i) in dynamic total-body PET. Although these two tracers both ultimately rely on the delivery of blood across the vessel wall into the tissue of interest, the information they provide are distinct. As a freely diffusible tracer with a high first-pass extraction fraction, [^{11}C]-butanol is rapidly distributed to and cleared from tissues. On the other hand, depending on the organ, FDG has a relatively low extraction fraction (Zuo et al., 2021), and is an irreversibly trapped marker of glucose metabolism. In most healthy tissues, metabolism and flow are coupled, with cerebral autoregulation of the brain as a notable exception. Thus, perfusion and glucose metabolism would

be correlated throughout the body. But in cases of flow-metabolism mismatch, dual tracer studies can provide complementary information.

This pathological change in flow-metabolism mismatch has been demonstrated in the myocardium. In a fasting state, the healthy myocardium relies on the oxidation of fatty acids as an energy source. However, with mild to moderate ischemia, the blood to the myocardium becomes partially restricted due to an atherosclerotic blockage, and glucose is taken up by myocardial cells at a higher rate (Brosius et al., 1997; Sun et al., 1994) with a corresponding reduction of perfusion in regions with mild ischemia (Marshall et al., 1983; Yamagishi et al., 1999, 2000). This flow-metabolism mismatch has been assessed via myocardial viability studies; perfusion SPECT tracers such as thallium-201 and [^{99m}Tc]-sestamibi and PET tracers like [^{82}Rb]-RbCl have been paired with FDG to assess myocardial viability (Tamaki et al., 1989; Tillisch et al., 1986). If there is a mismatch (e.g., reduced perfusion but normal FDG uptake), the tissue is assumed to be in a state of hibernation, and revascularization may reverse the ischemia. Reductions in both perfusion and glucose metabolism is indicative of irreversible scarring (Allman, 2013; Madsen et al., 2020).

Flow-metabolism mismatches have also been observed in many types of cancer. In fact, the Warburg effect, or the high glucose utilization by tumors even in aerobic, or oxygen-rich, settings (Cori & Cori, 1925; Warburg et al., 1927), is central to the clinical adoption of FDG PET for cancer imaging. The observation of altered metabolism in tumor cells has led to additional work investigating the difference in blood flow and metabolism with dual tracer PET. Although the studies catalogued in the review by Miles and Williams show no clear patterns overall in the relationship between tumor blood flow and metabolism, the studies cover a range of cancer types, which each have unique relationships between flow and metabolism (2008).

The reason for this mismatch in tumors is likely due to the microenvironment and changes in the availability of nutrients. The high metabolic rates of tumor cells result in increased vessel growth that leads to the formation of disorganized and leaky vascular networks in solid tumors (Dvorak et al., 1988). Further, tumors beyond approximately 100 microns in diameter can exhibit acute hypoxia, or lack of oxygen, due to the increased metabolic demand partnered with larger distances of these tumor cells to the nearest vessel (Dewhirst & Secomb, 2017; Krogh, 1919). Hypoxic tumor environments lead to two scenarios: chronic and acute hypoxia. Chronic hypoxia can lead to necrosis or cell death in parts of a tumor lesion; acute hypoxia can lead to increased tumor aggressiveness through the promotion of vessel growth but reduced cell proliferation, which in turn leads to resistance to both radiation therapy (Busk et al., 2020; Harada, 2011; Moeller et al., 2004) and chemotherapy (Gray et al., 1953; Rankin & Giaccia, 2008; Shannon et al., 2003). This resistance to therapies is both a result of reduced delivery of the therapy due to disorganized vessel networks, as well as the ability of tumor cells to reduce their metabolic needs in acutely hypoxic environments. Thus, quantification of coupled changes in perfusion and glucose metabolism may be important for treatment planning and monitoring. Since [^{11}C]-butanol maintains a high extraction fraction at high flow rates such as those in healthy myocardium, the investigation of flow-metabolism mismatch is an important future direction of this work.

1.10. Summary

In this chapter the foundational knowledge and motivations needed to understand the subsequent research in total-body PET kinetic modeling were introduced. The relevant kinetic models and associated IDIF corrections that are integral to this work were discussed, as the latter are key to addressing some of the quantitative complexities of kinetic modeling with total-body PET. Underlying concepts including radioisotope physics and the PET image reconstruction process

were also introduced. Since an important underlying assumption of PET kinetic modeling is that the dynamic sequence of images is quantitative, and given the many data corrections and the large dynamic range the scanner must operate across, it is first important to assess the magnitude and extent of quantitative errors in the underlying image data itself before proceeding to kinetic modeling. Those quantitative errors are the subject of chapter 2.

2. Chapter 2: Factors that affect quantification

2.1. Introduction: Challenges of total-body PET

As with the installation of any new scanner, characterization of image quality and quantitative accuracy is important for future studies. However, there are many unique challenges associated with the implementation of total-body PET systems. As compared to conventional PET/CT, where the axial FOV is limited to approximately 20 cm, the uEXPLORER has a 15- to 68-fold gain in sensitivity for total-body imaging due to its 196 cm axial FOV and 8 separate PET ring units that can detect counts from other rings, as long as they are within ±4 rings of each other (Spencer et al., 2021). However, this gain in sensitivity also increases the randoms and scatter fractions, and data-based corrections such as scatter and dead-time have to occur over a wide dynamic range. Additionally, the increased sensitivity allows the use of short (less than one $1/20^{th}$ of the scan time of conventional PET) temporal frames while still achieving diagnostic image quality (Badawi et al., 2019). Increased scatter and randoms contributions, activity ranges, and temporal resolution have pushed the existing PET correction standards to their limits, which were optimized using static PET images or uniform distributions of activity. Thus, as physics corrections specific to total-body PET mature, updates to the data correction and image reconstruction software are vital to improving quantitative accuracy. For further discussion of image reconstruction for total-body PET see the review by Efthimiou (2020).

Although the assessment of quantitative accuracy and improvement of the corrections for total-body PET across different software versions is actively being addressed by others (Leung, Berg, et al., 2021; Spencer et al., 2021), the work presented here uniquely focuses on the *in vivo* assessment of the quantitative accuracy of the uEXPLORER system. For previous scanner generations, standardized image phantoms and analyses could be performed based on the National

Electrical Manufacturers Association (NEMA) NU-2 guidelines. While it is still possible to characterize the uEXPLORER scanner with these guidelines, Spencer *et al*. (2021) have modified these guidelines for use with total-body PET scanners and have worked to demonstrate the performance of the scanner across a wide range of activity levels. Since most subjects can fit entirely within the imaging FOV, one can also assess quantitative accuracy in humans in a similar manner as is typically performed with image phantoms. Assuming a properly calibrated total-body PET scanner and perfect reconstruction process, all the activity within the imaging FOV can be summed and should equal the total injected dose. It is important to emphasize that is *unique* to total-body PET scanners, where all the injected activity can be accounted for within the FOV of the scanner, and any changes in the tracer distribution over time can be captured. For total-body PET acquisitions, the total image-derived activity (TIDA) can be compared directly with the injected dose.

In addition to updates to the reconstruction software, biases can arise from the spatial location of the tissue and IDIF ROIs. Although the use of an image-derived input function allows any issues with global image scaling or scanner calibration between software versions to be ignored during the modeling process, many corrections are spatially variant and thus, in addition to positioning differences during ROI delineation, can impact kinetic modeling. Further, any subject motion during the acquisition can negatively impact quantification; and since the entire body is within the FOV for total-body PET/CT systems, motion can influence the quantification in organs throughout the body. Thus, motion correction methods that require image cropping and focus on a single organ of interest (e.g., rotations of the head, cardiac gating) were not considered, and instead, methods that could be applied across multiple regions within the same image FOV were developed.

Using TIDA bias and other quantitative comparisons, the *in vivo* accuracy of the total-body PET system can be assessed for scenarios that push the correction factors to their limits, as is the case for high temporal resolution dynamic acquisitions, where, in the initial frames of the study, the frames may be short (~2s), and rapid changes in activity distribution occur that may influence deadtime, randoms, and scatter correction. Here, we discuss our work assessing and mitigating the impact of software updates, ROI position, and subject motion on TIDA, dynamic image activity, and the measured kinetic parameters.

2.2. Total-body PET bias—TIDA

As part of the scanner characterization work by Leung and others (2021a), total image-derived activity (TIDA, units MBq) was used to assess the activity bias for a number of subjects, allowing for further characterization of the uEXPLORER performance for different body habitus and body mass indices (BMI), activity levels, and activity distributions. For an image frame *m*, TIDA and TIDA bias can be calculated as follows:

$$TIDA(m) = \sum_i V \times A_i\,(m) \tag{2.1}$$

$$TIDA\ bias(m) = 100\% \cdot \frac{TIDA(m) - i.d.}{i.d.} \tag{2.2}$$

where V is the voxel volume in milliliters, $A_i(m)$ is the activity concentration in frame m for pixel i (units MBq/ml) and *i.d.* is the injected dose (MBq). To assess the performance of the uEXPLORER reconstruction software in recovering the total injected dose, TIDA was compared across different voxel sizes, temporal framing, isotopes, and software updates. TIDA was assessed across entire dynamic acquisitions as well as for longer static frames (i.e., 5-minute frames) after the stabilization of activity. Here, the ways in which TIDA measurements provide relevant information are discussed with examples.

FDG TIDA bias was compared for 2 healthy volunteers who underwent 1-hour dynamic FDG acquisitions (BMI: 29.5, 20.0 kg/m^2; injected doses: 374.3, 378.7 MBq FDG; 1 male, 1 female; 62 and 30 years). FDG datasets were reconstructed with three different software versions (V0, V1, and V2). Major algorithmic updates that occurred with the different versions are listed in table 2.1. FDG images were reconstructed with 3 temporal framing schemes designated 1H29, 1H66, and 2m90, with increasing temporal resolution with frame number (table 2.2).

Table 2.1: Reconstruction software version updates

Version	*Major updates with respect to previous version*
V0	-
V1	Artifact reduction of the attenuation map, deadtime correction look-up table updated
V2	Additional artifact reduction of the attenuation map, updated scatter correction methods

[^{11}C]-butanol TIDA bias was compared across matrix sizes and temporal framings for one subject who underwent a dynamic study at rest lasting 30 minutes (BMI: 28.9 kg/m^2; injected dose: 249.0 MBq [^{11}C]-butanol; female; 64 years). Images were reconstructed with the temporal framing schemes 30m29, 5m12, 5m52, and 2m90 with 4.0 and 2.344 mm isotropic voxel sizes, as listed in table 2.2.

Table 2.2: Temporal framing and reconstructed image sizes for TIDA bias

Tracer	*Framing designation*	*Framing*	*Matrix size*	*Voxel size(s)*
FDG	1H29	6x10 s, 2x30 s, 6x60 s, 5x120 s, 4x180 s, 6x300 s	150x150x486x29	4.0 x 4.0 x 4.0 mm^3
FDG	1H66	30x2 s, 12x10 s, 6x30 s, 12x120 s, 6x300 s	150x150x486x66	4.0 x 4.0 x 4.0 mm^3
FDG	2m90	60x1 s, 30x2 s	150x150x486x90	4.0 x 4.0 x 4.0 mm^3
[^{11}C]-butanol	30m29	12x5 s, 6x10 s, 6x30 s, 5x300 s	150x150x486x29	4.0 x 4.0 x 4.0 mm^3
[^{11}C]-butanol	30m29	12x5 s, 6x10 s, 6x30 s, 5x300 s	256x256x828x29	2.3438 x 2.3438 x 2.344 mm^3
[^{11}C]-butanol	5m52	30x2 s, 12x5 s, 6x10 s, 4x30 s	150x150x486x52	4.0 x 4.0 x 4.0 mm^3
[^{11}C]-butanol	5m52	30x2 s, 12x5 s, 6x10 s, 4x30 s	256x256x828x52	2.3438 x 2.3438 x 2.344 mm^3
[^{11}C]-	5m12	6x10 s, 4x30 s, 2x60 s	150x150x486x12	4.0 x 4.0 x 4.0 mm^3

butanol				
[^{11}C]-butanol	5m12	6x10 s, 4x30 s, 2x60 s	256x256x828x12	2.3438 x 2.3438 x 2.344 mm^3
[^{11}C]-butanol	2m90	60x1 s, 30x2 s	150x150x486x90	4.0 x 4.0 x 4.0 mm^3
[^{11}C]-butanol	2m90	60x1 s, 30x2 s	256x256x828x90	2.3438 x 2.3438 x 2.344 mm^3

The investigation of TIDA bias can verify that decay or scatter correction were correctly applied. A lack of scatter correction can be identified through a large increase in scale of the TIDA curve for an FDG study, and shifts in the TIDA curve that may occur due to software updates can be identified (figure 2.1A). TIDA can also be used to assess relationships between different corrections and patient size; figure 2.1B demonstrates this, where an artifact in the attenuation map was corrected for, and the average TIDA bias over the last 15 minutes of the acquisitions decreased in magnitude in proportion to BMI. Figure 2.1C shows the impact of updated deadtime correction on the resulting TIDA; as the number of frames increase, the shorter the frames, and higher the bias in the early phases of the dynamic study. Improvements in deadtime correction can reduce this bias in the short frames. Changing of temporal framing and matrix size also can push the reconstruction algorithm and associated corrections to their limits, as seen in figure 2.1D in the early frames, where the activity enters the imaging FOV and stabilizes after the radiotracer becomes more distributed throughout the body, and the frame lengths increase.

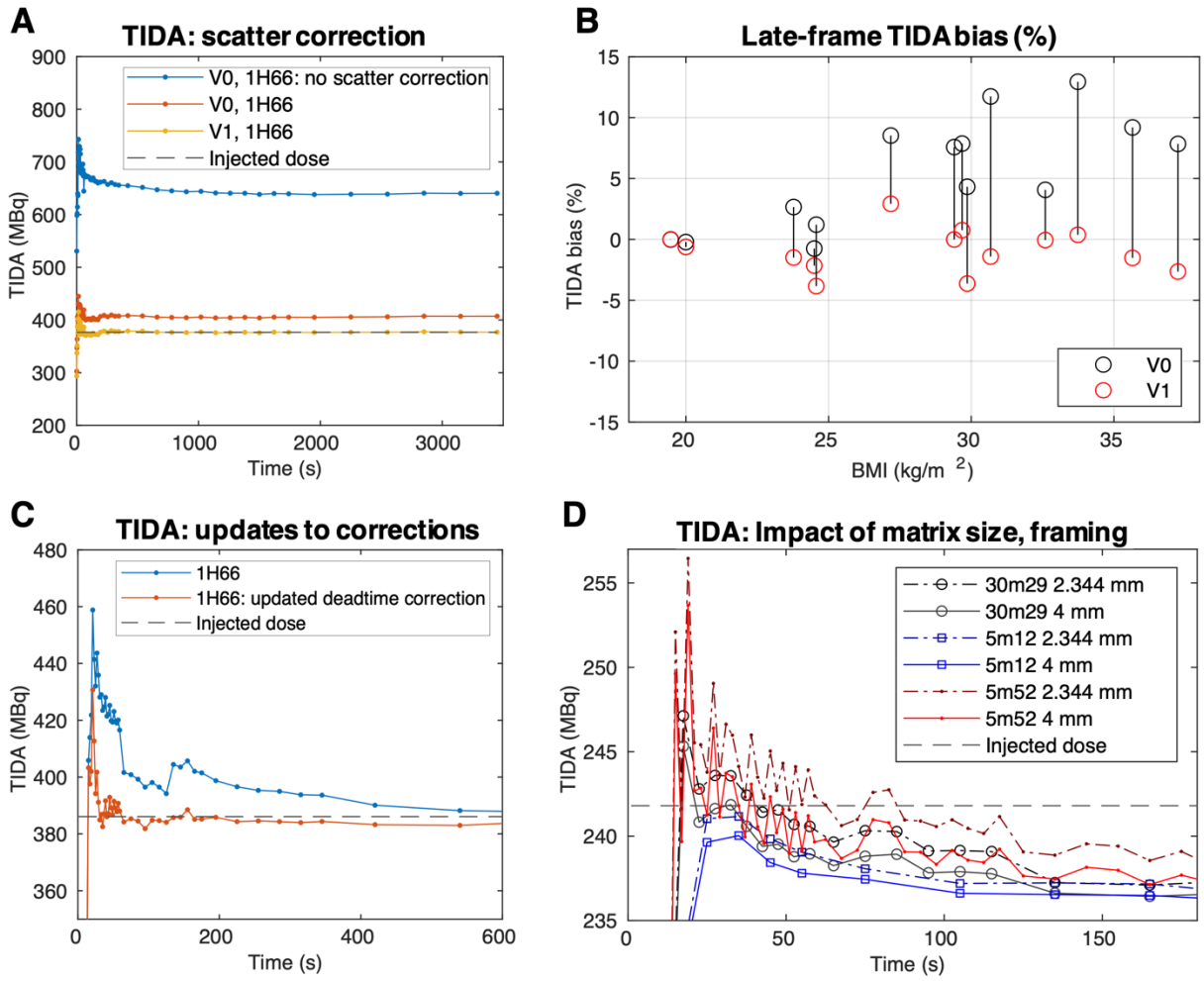

Figure 2.1: TIDA investigations of correction factors, software updates, and reconstruction parameters

Figure 2.1: TIDA investigations of correction factors, software updates, and reconstruction parameters. Subfigures A, B, and C focus on FDG acquisitions, while subfigure D shows results for a baseline [^{11}C]-butanol study. TIDA plots with and without scatter correction, in addition to changes in software from V1 to V2 (A). As time increases, the TIDA values become stable, and software updates improved agreement with the injected dose (dashed line). By looking at the average TIDA bias from the last 15 minutes of the study, late frame bias could be compared to BMI (B). With a change in the reconstruction software (from V0 to V1) accounting for differences between the CT and PET FOVs for generation of the attenuation map (B, red circles), there was a

BMI-dependent reduction in the magnitude of TIDA bias. TIDA can be used to check the impact of updates to correction factors like dead time, as shown in (C), where improved agreement of TIDA and the injected dose (dashed line) can be seen in the early timepoints of the acquisition. In the early phases of the scan, the activity is highly concentrated in the blood, pushing the limits of deadtime correction for the detector modules that capture events from the blood pool. Overall performance of the reconstruction algorithm can also be assessed across temporal framing protocols and matrix sizes, as is shown for [^{11}C]-butanol in (D).

2.3. Total-body PET bias—TAC-level assessment of reconstructed PET images

Although TIDA plots are useful for understanding global scaling issues, changes to the reconstruction or image corrections can also cause local changes in the activity concentration over the course of a dynamic study. Thus, ROI-based TACs can also be used to investigate the impact of software updates in a regional manner for different parts of the body. TACs derived for grey matter, liver, and the descending aorta (DA) using the software versions V0, V1, and V2 are shown Figure 2.2. Changes in the TACs were both tissue and frame dependent. While V1 demonstrated a scalar shift in the TACs with respect to V0, software version V2 TACs for liver and DA decreased across the scan time as compared to V1. In contrast to liver and DA, grey matter showed increasing activity across time with V2 as compared to V1.

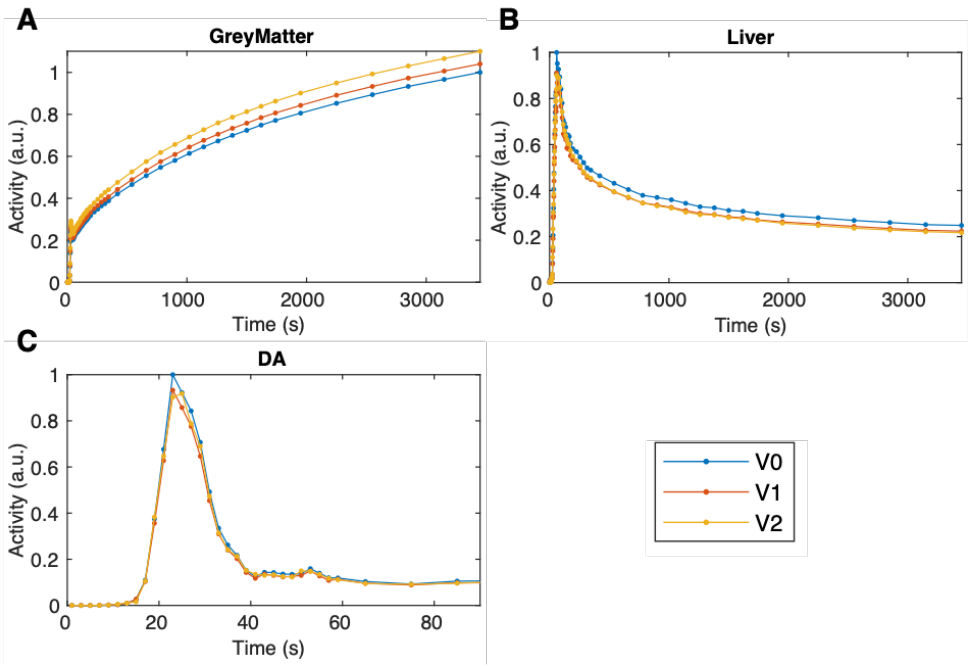

Figure 2.2: Representative TACs of grey matter, liver, and descending aorta IDIF

Figure 2.2: Representative TACs of grey matter (A), liver (B), and descending aorta (DA) IDIF (C), from a 60-minute dynamic FDG study. TACs were derived using identical ROIs applied to images reconstructed with different software versions (V0, V1 and V2). By the last frame of the 60-minute study, grey matter V2 activity was 10% greater than V0.

Previous work has demonstrated the effects of the iterative reconstruction methods and parameters such as iteration number, temporal framing, image matrix size, time-of-flight (TOF) and point spread function modeling-based smoothing on kinetic parameter estimates (Boellaard et al., 2001; Brambilla et al., 2021; Girard et al., 2020; Häggström et al., 2014, 2015; Hove et al., 2008; Presotto et al., 2015; Siekkinen et al., 2020; Wallstén et al., 2017). Although we employ similar methods to characterize the effects of some of these reconstruction parameters (framing, voxel size) in kinetic modeling estimates in chapter 4, in this chapter changes in the kinetic parameter estimates from software version to version are highlighted. To accomplish this, the bias

was determined using the current software version (V2) as the standard, to compare to two previous versions (V0 and V1). Dynamic FDG studies from two healthy volunteers were used for the comparison (BMIs: 29.5, 29.6 kg/m^2; injected doses: 374.3, 370.0 MBq FDG, 1 male, 1 female). An irreversible two-tissue compartment model was fit for TACs from a number of metabolically distinct regions (whole brain, grey matter, kidney, liver, lung, muscle, myocardium, spleen). Differences in parameter estimates were assessed using Bland-Altman plots with 95% limits of agreement.

As shown in the Bland-Altman plots in figure 2.3, V1 and V2 parameter estimates were more similar than V0 and V1 for K_1, K_i and v_b, and moreover, V1 showed a tighter K_1 and K_i agreement with V2 than V0, for spleen and grey matter respectively.

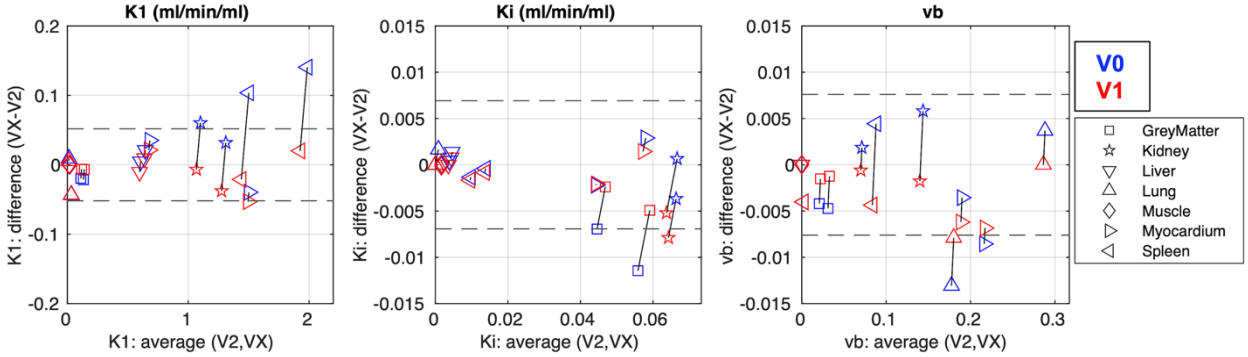

Figure 2.3: Bland-Altman plots of FDG parameter estimates.

Figure 2.3: Bland-Altman plots of FDG parameter estimates that compare modeling results between different software versions. Using the most current software version V2 as the ground truth, Bland-Altman plots were generated in comparison to VX, where X is 1 or 0, representing progressively older software versions. Sets of Bland-Altman data points for the same ROI are connected by a solid black line. The difference between V1 and V2 (red) show fewer datapoints outside the 95% limits of agreement, showing that V1 and V2 software result in more similar values than V0 (blue).

2.4. Tissue and IDIF ROI delineation: motion correction

The increased temporal resolution of total-body PET, while improving the overall dynamic image quality, also captures physiologic motion. Respiratory and cardiac motion occur at rates on the order of 10-100 per minute. While the impact of cardiac motion might be considered somewhat limited to the heart and the aorta (Zhang et al., 2020), respiration can compress most of the tissues in the abdomen and can shift the position of tissues throughout the body. Further, filling of the bladder over the course of a 60-minute acquisition can cause aperiodic, large shifts in many tissues (figure 2.4A). Shorter frames will reduce the amount of spatial averaging of motion-related shifts in position that occur within a given frame, but also can result in large changes in the TACs from one frame to the next, if the motion is left uncorrected (figure 2.4B). If the tracer is delivered as a short bolus, as is ideal, the IDIF activity from the blood in the aorta or left ventricle will have a sharp peak. However, the shape and height of the IDIF are also impacted by spatial positioning of the ROI, as will be discussed in the next section.

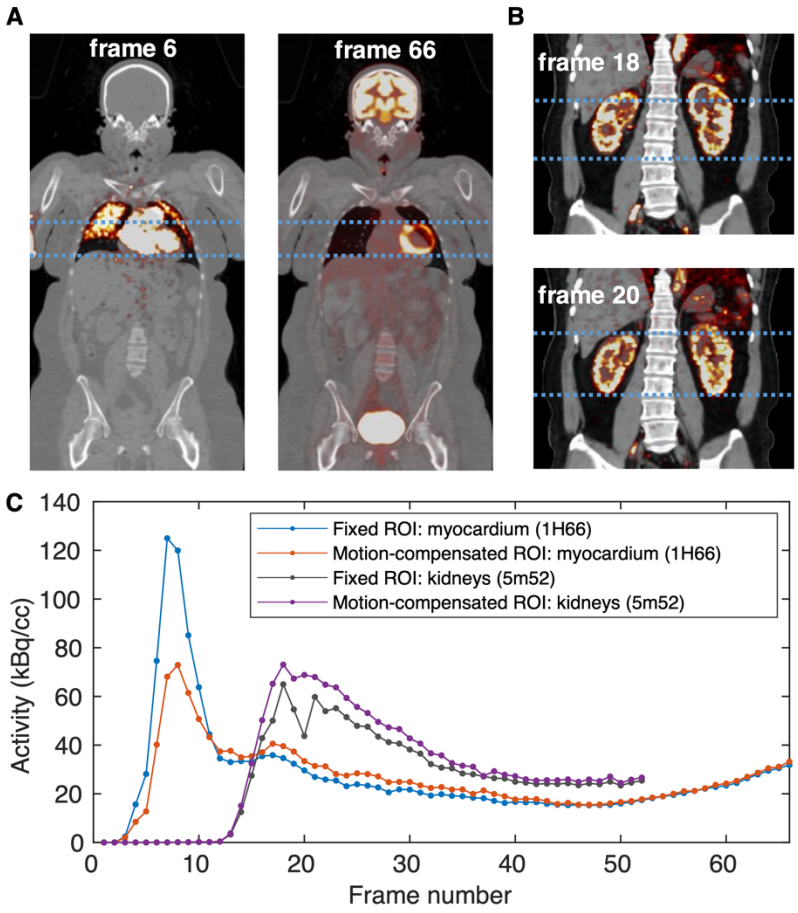

Figure 2.4: Impact of subject motion on TACs

Figure 2.4: Impact of subject motion on TACs. A myocardial example is shown in (A), dashed lines indicate the superior and inferior edges of the myocardium in frame 66, which represents the last 5 minutes of the 60-minute FDG acquisition. Frame 6 shows the position of the myocardium as the tracer enters the left ventricle; in this frame, the right and left ventricles can be distinguished from each other and from the septal wall by the lack of uptake in the myocardium. The mismatch between the final PET frame 66 and the CT, which was acquired just prior to the dynamic PET acquisition, illustrates the difference in the positioning of the myocardium over the 60-minute acquisition, likely due to bladder filling during the acquisition. This results in reduced activity in the measured TAC due to less overlap of the ROI with the left ventricle blood pool. Respiratory motion can cause large shifts in the position of the renal cortices (B). The dashed lines in (B)

indicate the superior and inferior edges of the right renal cortex in frame 20. Manual compensation for motion can be performed across the dynamic series by shifting the ROI to reduce the misalignment, as is shown in (C), for the myocardial example in (A) and for the renal cortex in (B). The mismatch between the ROI position and the frame-by-frame tissue location can lead to large jumps in the ROI-based TACs (C, fixed ROI: kidney). For the kidney, higher activity in the measured TAC was observed with motion compensation, due to better alignment of the ROI with the renal cortex within individual image frames.

It is important to note that, although both rigid and non-rigid image-based registration methods exist, these approaches need to be compared and carefully evaluated before they can be implemented routinely for total-body PET datasets. Shifts in the centroid of distribution or the geometric center of preselected regions within the FOV have been used to guide dynamic frame selection during the reconstruction process (Leung, Revilla, et al., 2021). Non-rigid deformations, where geometric transformations can be applied at the voxel level, can also be applied to total-body PET data (Sundar, Wang, et al., 2021), but this is computationally demanding given that the image size is frequently $>10^6$ voxels, and is challenging for dynamic studies, when the tracer distribution changes throughout the course of the scan. With large enough sample datasets, it is possible that a machine learning approach may be used to perform motion correction with low bias and high computational efficiency (T. Li et al., 2021; Sundar, Iommi, et al., 2021). Thus, the strategies discussed here focus on minimizing the impact of and manual correction for motion in total-body PET datasets.

Three procedures were aimed at reducing the impact of or compensating for motion with ROI-derived TACs. ROIs were defined on: (i) the last frame of the dynamic series, (ii) an average image,

and (iii) multiple frames for maximizing the contrast. Methods (i) and (ii) utilize static ROIs to reduce the impact of motion artifacts based on high-statistical quality images, and method (iii) implements dynamic ROIs, where the ROI was shifted from frame to frame to correct for motion.

Since there are many possible tissues of interest with varying statistical quality throughout a total-body PET study, table 2.3 lists the strategies employed in this work to delineate specific ROIs in total-body PET image datasets, where strategy (i) utilizes the frame 55-60 minutes into the FDG acquisition. Since the distribution and radioactive decay of [^{11}C]-butanol results in peak image quality during the first 5 minutes of the 30-minute dynamic study, (i) and (ii) utilize frames from 3-3.5 minutes and the first 0-3.5 minutes respectively. After application of methods (i), (ii), and (iii), ROIs were then manually corrected for gross motion as needed. For example, for subjects that exhibited a turning or rotation of the head during the study, white and grey matter ROIs were manually adjusted across dynamic frames.

Table 2.3: ROI delineation strategies to reduce the impact of motion

	ROI delineation strategy		
Region	**(i) Late frame**	**(ii) Average image**	**(iii) High-contrast frames**
Grey matter		x	
White matter		x	
Kidney		x	x
Liver		x	x
Lung		x	x
Skeletal Muscle	x (FDG)	x ([^{11}C]-butanol)	x
Myocardium		x	x
Spleen		x	x

The three delineation strategies were compared in grey matter, kidney, and the myocardium of two healthy subjects that each underwent dynamic FDG or [^{11}C]-butanol acquisitions. As can be seen in figure 2.5, the impact of the three methods was tissue and activity distribution dependent.

The use of high-contrast frames reduces the myocardial peak activity concentration by approximately 50% (figure 2.5 B,E). As shown in table 2.4, the different delineation methods can result in variable estimates of v_b and K_1, particularly in the myocardium, with little impact on AIC.

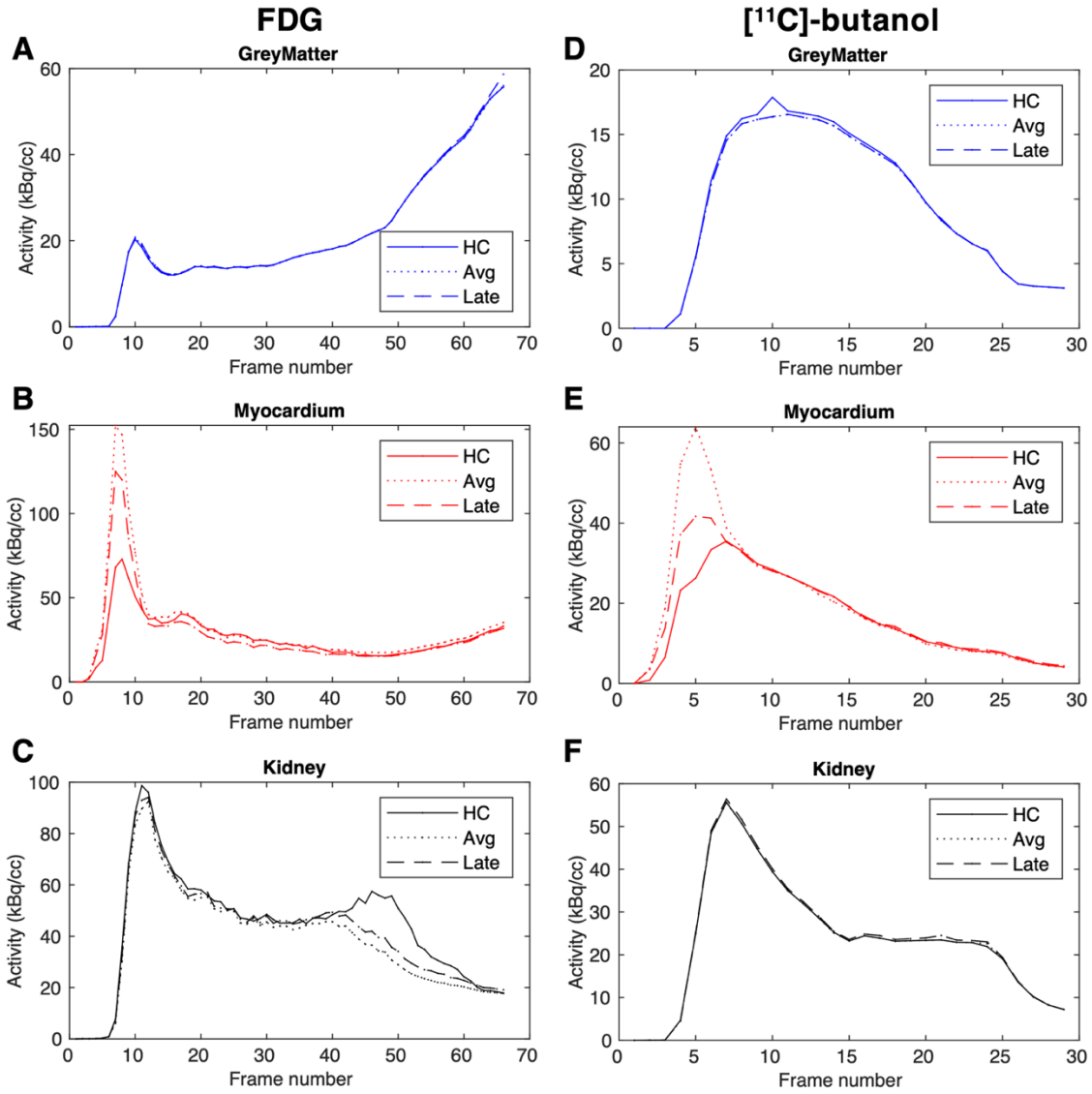

Figure 2.5: TACs for various tissues derived with different strategies.

Figure 2.5: TACs for various tissues derived with different strategies (high-contrast (*HC*), average image (*Avg*), and late frame (*Late*)) aimed at addressing subject motion. TACs are shown for two acquisitions: one FDG (A-C) and one [^{11}C]-butanol (D-E). Across the three tissue types shown here, grey matter was least impacted by ROI delineation strategy (A, D). The use of high-contrast

(HC) frames results in lower myocardial peaks for both FDG (B) and [^{11}C]-butanol (E), likely due to the improved corrections for cardiac motion and spillover from the right ventricle blood pool, especially in early frames.

Table 2.4:Parameter estimates and AIC across ROI delineation methods

	(i) Late frame	(ii) Average image	(iii) High-contrast frames
Parameter		**Butanol** **Grey Matter**	
v_b	0.061	0.061	0.066
K_1 (ml·min^{-1}·cm^{-3})	0.489	0.489	0.505
delay **(s)**	9	9	10
AIC	-500.107	-500.145	-485.212
		Myocardium	
v_b	0.262	0.437	0.151
K_1 (ml·min^{-1}·cm^{-3})	1.028	1.040	1.084
delay (s)	0	0	1
AIC	-445.070	-434.547	-483.101
		Kidney	
v_b	0.263	0.258	0.258
K_1 (ml·min^{-1}·cm^{-3})	1.339	1.323	1.325
delay (s)	4	4	4
AIC	-450.998	-452.393	-452.473
Parameter		**FDG** **Grey Matter**	
v_b	0.054	0.054	0.053
K_1 (ml·min^{-1}·cm^{-3})	0.172	0.169	0.167
delay (s)	4	4	4
AIC	-964.828	-951.639	-945.544
		Myocardium	
v_b	0.320	0.383	0.109
K_1 (ml·min^{-1}·cm^{-3})	0.850	1.247	1.284
delay (s)	-2	-2	-3
AIC	-845.291	-801.273	-831.939
		Kidney	
v_b	0.167	0.150	0.201
K_1 (ml·min^{-1}·cm^{-3})	1.252	1.312	1.026
delay (s)	2	2	2
AIC	-700.910	-713.728	-665.601

2.5. Tissue and IDIF ROI delineation: inter-reader variability

Delineating ROIs for each region, including the IDIF, can be observer-dependent. This is especially true for the measurement of blood parameters such as delay and dispersion, which not only depend on physiological parameters like heart rate, but also on the location of the IDIF measurement within the blood pool as compared to the tissue ROI. For example, the delay and dispersion from the carotids to the brain are smaller than if an IF was derived from the radial artery using an external blood sampling system that has been calibrated for use with the PET scanner. Even within the same vessel, such as the descending aorta, ROI placement for the IDIF measurements can vary.

As shown in figure 2.6, three researchers in the UC Davis Molecular Imaging Physics and Engineering Team (MIPET) who have been implementing IDIF-based kinetic modeling for at least 2 years were tasked with delineating IDIFs in the right ventricle (RV), left ventricle (LV), ascending aorta or aortic arch (AA), and the descending aorta (DA, figure 2.6, arrows) for a number of 1-hour dynamic FDG studies. From fully automated methods like k-means clustering of the dynamic data, to manually choosing a distinct portion of each blood vessel using an anatomical landmark, the position and dimensions of the IDIF ROIs can vary depending on the best judgement of the delineator, also referred to here as a reader. As shown in figure 2.7 for the descending aorta, the resulting IDIFs are impacted by the anatomical location and volume of the defined ROI, which impacts the estimated kinetic parameters for FDG. The mean peak IDIF activity in figure 2.7 was 450.6 kBq/cc with a standard deviation of 36.3 kBq/cc, yielding a coefficient of variation (mean/standard deviation) of 0.08. The average area under the curve was 44.7 MBq·sec/cc with a standard deviation of 2.5 MBq·sec/cc and a coefficient of variation of 0.06.

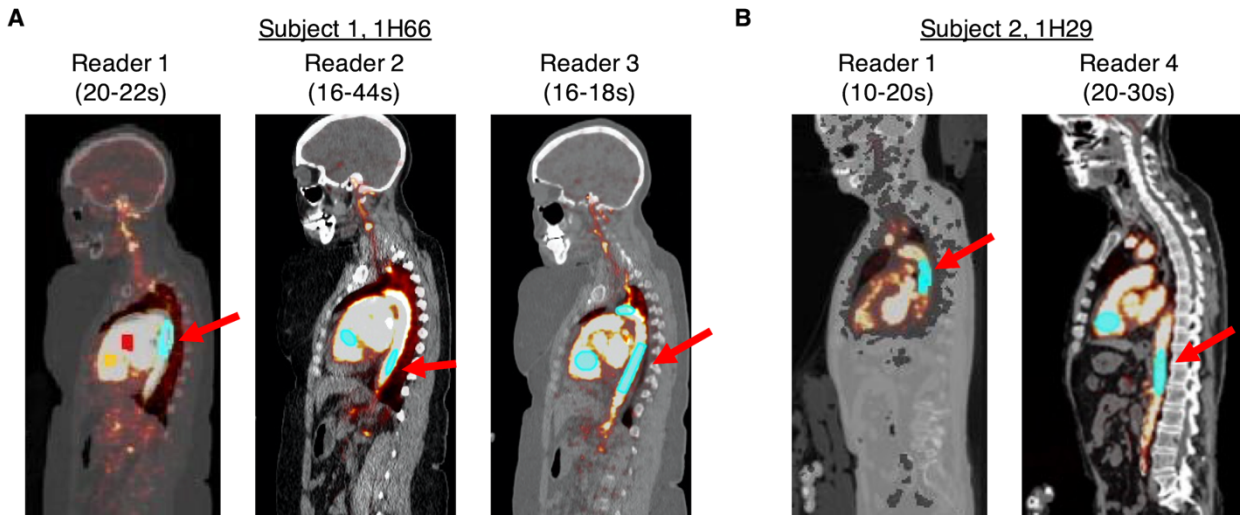

Figure 2.6: Cross-sectional views of IDIF delineations in the aorta

Figure 2.6: Cross-sectional views of IDIF delineations in the aorta. Each panel shows views focused on the descending aorta IDIF (arrows) delineated by different experienced kinetic modeling researchers. (A) focuses on one subject with 1H66 framing, while (B) focuses on another subject with 1H29 framing. IDIF position and the selected frame for ROI delineation can vary depending on the reader.

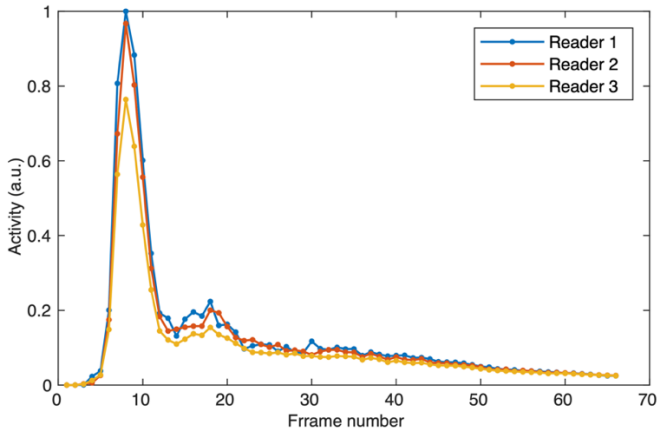

Figure 2.7: **IDIFs from the three readers for the descending aorta**

Figure 2.7: IDIFs from the three readers for the descending aorta across frame number. The three IDIFs are scaled to the maximum of Reader 1 for the purpose of visual comparison. The peak in frame 8 (approximately 12-14 seconds post injection) and recirculation portion in frames 14-22

(approximately 24-40 seconds post injection) show discrepancies between the three readers, although all three TACs converge for the later frames of the acquisition.

For the subject included in figure 2.6A, whole-grey matter TACs were fit using an irreversible two-tissue compartment model with delay correction, for each of the reader-defined IDIFs, a subset of which is shown in figure 2.7. The percent difference in K_i for each IDIF was determined as follows: 100% x (minimum K_i – maximum K_i) / maximum K_i. After the fitting process was complete, K_i estimates are used as labels for each of the IDIFs delineated by the three readers in various IDIF locations (figure 2.8). ROIs were overlaid on dynamic time frames that best illustrate the differences between the blood pool. Not only was there a large range of percent differences (8-40%) in parameter estimates between readers in the same IDIF region such as the left ventricle, but there were also >20% increases in K_i depending on the IDIF location. Thus, in subsequent chapters, IDIFs were derived by a single individual with the goal of keeping the locations and volumes of the ROIs consistent between image datasets.

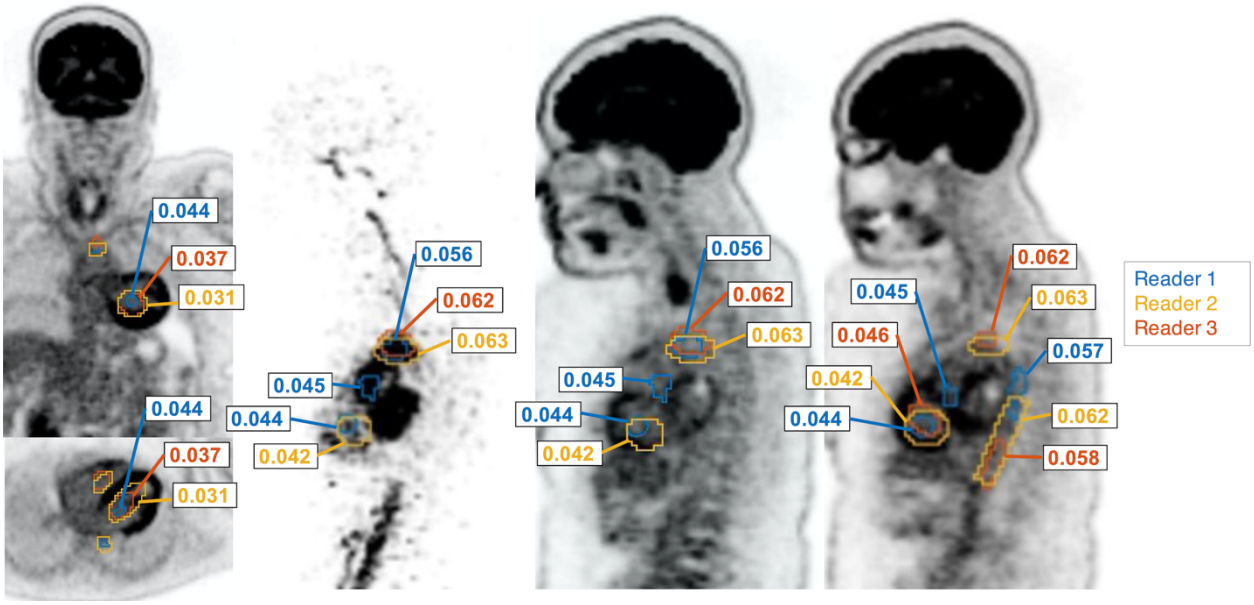

Figure 2.8: Color-coded IDIF ROIs from three readers

Figure 2.8: Color-coded IDIF ROIs from three readers. Each ROI is labeled with the associated whole-grey matter K_i ($ml \cdot min^{-1} \cdot cm^{-3}$), and overlaid on a number of frames and sagittal slices.

2.6. Discussion

As detailed in this chapter, PET image-based quantification relies on a variety of factors, including updates to the image reconstruction software, dynamic framing and voxel size. A major challenge with the installation of any new PET/CT system is determining the standard practices for reconstructing the images. Different reconstruction settings are necessary depending on the use case; for static clinical acquisitions, for example, one set of reconstruction settings may work better for a specific clinical question than another set. For dynamic imaging and quantitative kinetic modeling, the crucial impact of this work was the quantitative assessment of the reconstructions and software at the total-body level.

One metric implemented here to evaluate quantitative image accuracy was TIDA; TIDA can be used to assess a variety of reconstruction scenarios, including lack of scatter correction or other

correction factors, but also changes from software version to version, and instances where there is a gradual loss of activity in the FOV, as is the case for [^{11}C]-butanol and the exhalation of its metabolite, [^{11}C]-CO_2. However, TIDA may not be implemented in PET/CT systems when the subject does not fit within the imaging FOV. While this is a strength of the uEXPLORER system, as the only commercially available total-body PET/CT system to date, TIDA-based metrics for *in vivo* quantification is not broadly available to all systems.

The examples included here for software-based changes in kinetic parameters, and the impact of various ROI-based delineation strategies demonstrate the need for thoughtfulness when selecting image datasets and defining ROIs, especially if quantitative comparisons are drawn between them. Further, if multiple readers are needed, careful training to reduce the variability in the reader IDIF delineation may be needed. The ROI-based delineation strategies discussed here may also serve as guidelines for cases where a ground-truth TAC is needed, such as in the assessment of motion correction algorithms on TAC shape and kinetic parameter estimates.

A limitation of the ROI strategies included here is that they have not been extended to multi-acquisition or longitudinal studies, where a dynamic study is performed on day 0, and the subject leaves the scanner. Follow up studies may occur hours to weeks later. While the ROI delineation methods developed here may still be useful since they were developed and assessed in a number (N = 3) of test-retest studies, they were not developed explicitly in consideration of extended timepoint imaging. Thus, further work is needed to consider ROI delineation for additional timepoints.

2.7. Summary

Quantification of metabolism in dynamic PET can be affected by reconstruction parameters such as temporal framing and image matrix size, in addition to changes in the correction methods and

factors during the reconstruction process, such as scatter correction. For long axial FOV of total-body PET scanners, TIDA can be used to investigate and interpret the global effects of changes to the software or reconstruction parameters. For local changes in the activity distribution, investigation of the regional or organ-specific TACs and estimated parameter values can be fruitful in assessing the impact of software changes. Additionally, ROI delineation can be tissue and tracer-dependent, where the effects of motion, tracer distribution over time, and method of delineation can alter the quality of the measured TAC. Though the methods to understand and mitigate the effect of these phenomena on TAC and estimated kinetic parameters were briefly discussed here, Chapter 4 will dive deeper into the methodology implemented for [^{11}C]-butanol perfusion imaging.

3. Chapter 3: Leading edge method for delay correction

3.1. Introduction

An input function (IF) is required for fully quantitative PET kinetic modeling and can be derived through arterial blood sampling (ABS) (Lammertsma, 2019). However, ABS is invasive, technically challenging, and can introduce additional errors in the measured IF arrival time and bolus shape, which may result in biased kinetic parameter estimates when left uncorrected (T. Feng et al., 2021; H. Iida et al., 1986; Islam et al., 2017). An image-derived input function (IDIF) can be sampled from the images directly, reducing errors in arrival time and removing the external dispersion introduced by ABS. Still, the delay between the IF peak and arrival time at a tissue or voxel of interest must be considered.

The advent of high-efficiency, long axial field-of-view scanners, such as the uEXPLORER total-body PET system (Cherry et al., 2017; Zhang et al., 2020), presents the opportunity for high signal-to-noise total-body kinetic modeling. Short frames with high count statistics are possible for improved estimation of parameters such as delay. Additionally, an IDIF can be derived from the larger vessels, where partial volume effects are reduced. However, with total-body PET, delay correction becomes more important because the IDIF will be further from a tissue of interest than a more localized IDIF (e.g., carotid IDIF for grey matter) and incorrect delay estimates may lead to parameter bias (T. Feng et al., 2021; H. Iida et al., 1986; Islam et al., 2017). Different tissues will also have their own unique delay values, and thus delay correction must be performed for every voxel or regional time activity curve (TAC).

Common methods of delay correction include: (i) setting delay to a predetermined value (H. Iida et al. 1986; H. Iida et al. 2000), (ii) adjusting the IF based on an IDIF close to the tissue of interest (H. Iida et al., 1986, 1988), or (iii) jointly estimating delay during the fitting process (T.

Feng et al., 2021; Lammertsma et al., 1990; Meyer, 1989). However, the widely used joint estimation (JE) method is costly in terms of computation time, especially for voxel-level total-body PET, because it involves non-linear fitting of kinetic parameters for all possible delay values. Therefore, a much faster method for estimating bolus delay would be beneficial. Applications where voxel-level parametric imaging is important include the detection/quantification of metastatic lesions, and disease processes that result in heterogenous tracer delivery and uptake within a tissue or organ.

Here, we draw our inspiration from pulse timing methods, including leading edge (LE) and the constant fraction discriminator (CFD) methods, that are used to efficiently determine the arrival time of electronic pulses from a radiation detector (Knoll, 2005). In this work, LE and CFD pulse timing methods are applied to TACs rather than electronic pulses. Delay is defined as $t_d - t_0$, which is the difference between the arrival times of the bolus in the region chosen to define the IF, t_0, and of a tissue or voxel TAC determined using one of the pulse timing methods, t_d. Implementation of pulse timing methods would greatly reduce the computational burden of the fitting process for a given kinetic model, since the non-linear least-squares fitting process can be performed for a single delay value, as determined by these methods. While these methods are computationally efficient, the choice of parameters (LE trigger threshold, CFD attenuation values) can impact delay estimation. Therefore, we investigate the use of pulse timing methods for time delay estimation and correction for quantitative total-body kinetic modeling and parametric imaging.

3.2. Materials and methods:

3.2.1. Computer simulations

Computer simulations of TAC data were developed to evaluate bias and standard deviation (s.d.) of delay estimation approaches. A high-temporal resolution IF (0.1-second sampling) representing

a bolus of ^{18}F-FDG was generated based on the tri-exponential function proposed by Feng *et al*. (D. Feng et al., 1993, 1997). The IF was shifted by 100 randomly selected delay values between 0 and 50 s. Brain grey matter TACs were simulated based on these delayed IFs and typical kinetic parameters (v_b = 0.05, K_1 = 0.06 (mL/min/mL), k_2 = 0.07 (min^{-1}), and k_3 = 0.07 (min^{-1}), k_4 = 0 (min^{-1})) from Huisman et al., (2012). For each delay value, 500 noisy realizations were generated using a commonly used time-changing Gaussian noise model (Wu & Carson, 2002) with a mean equal to the initial activity concentration in frame m, and standard deviation $S_c \cdot \delta_m$:

$$TAC_m \sim Gaussian(\overline{TAC_m}, S_c\delta_m), \quad \delta_m = \sqrt{\frac{\overline{TAC_m}\cdot\exp(\lambda t_m)}{\Delta t_m}} \tag{3.1}$$

where δ_m is dependent on the radioisotope decay constant λ, frame length Δt, and mean activity concentration $\overline{TAC_m}$ in frame m. The scale S_c was set to four noise levels of 0.03, 0.1, 0.2, and 0.3 to encompass TACs with different statistical quality. To mimic zero-mean noise present in measured TACs prior to bolus arrival, the activity concentration included in $\delta_m$was modified to have a mean of 0.5% of the maximum TAC activity:

$$TAC_{early,m} \sim Gaussian(0, S_c\delta_m), \quad \delta_m = \sqrt{\frac{0.005\cdot\max(\overline{TAC})\cdot\exp(\lambda t_m)}{\Delta t_m}}. \tag{3.2}$$

TACs were then re-binned to frame lengths of 1, 2, 5, and 10 s and used to assess the impact of framing on delay estimates. Supplemental figure A.1A shows an example TAC with S_c equal to 0.1.

For the LE method (Knoll, 2005), a trigger threshold is selected and the time at which the signal amplitude passes that threshold is recorded as the arrival time. LE thresholds were set across a wide range (2.5 to 50%) of the peak activity in the first 120 seconds. A 10% LE threshold is shown in supplemental figure A.1B. For the CFD method (Knoll, 2005), the TACs were shifted in time by 2 seconds for shorter framing, or by 1 frame for frame lengths >2 seconds. Attenuated and

inverted versions of the TAC (attenuated to between 2.5 and 50% of the peak activity) were added to the shifted TAC and the resulting zero-crossing point marks the arrival time (supplemental figure A.1C). LE and CFD-based estimates for each combination of delay value, frame length, noise level, and % peak activity were determined. Average bias and standard deviation of the LE and CFD delay estimates were determined by comparing the estimates with the ground truth. Based on the results of these simulations, only the LE method was subsequently applied on human data.

3.2.2. Human data

Institutional Review Board approval and written informed consent was obtained for 14 healthy volunteers (6 male, 8 female, body mass index (BMI): 19.4-37.0 kg/m^2, 26-78 years) and 7 male subjects with genitourinary cancer (GUC) (BMI: 20.1-32.0 kg/m^2, 56-76 years). Subjects were injected with an average dose of 357.8 MBq FDG (range: 331.9-391.8) and underwent 60-minute dynamic studies on the uEXPLORER scanner (Spencer et al., 2021). Images were reconstructed with vendor-provided TOF-OSEM software (20 subsets, 4 iterations, 150x150x486 image matrix size, 4 mm isotropic voxels) with corrections for attenuation, scatter, randoms, deadtime and decay (Leung, Berg, et al., 2021). No point spread function modeling was applied. For generating parametric images, image data were smoothed using a composite image prior and the kernel method (G. Wang & Qi, 2015). The following framing protocol was used to generate 66 timepoints: 30x2 s, 12x10 s, 6x30 s, 12x120 s, 6x300 s.

For all human data, an IDIF was derived from a region of interest (ROI) in the left ventricle. Tissue compartment model selection was incorporated to account for tissue spaces where FDG is not metabolized, such as the blood pool. Model selection was performed for a range of tissue ROIs and voxel TACs by fitting a 0-tissue 1-parameter (where v_b was the only non-zero parameter), a 1-tissue 3-parameter, and an irreversible 2-tissue 4-parameter model ($k_4 = 0$); the model with the

lowest Akaike Information Criterion was chosen. For comparison, parametric Patlak plots (Patlak et al., 1983) were generated with and without using the JE delay estimates from model selection. Patlak-transformed TAC data representing the period from 35 to 60 minutes post injection were used for determination of Patlak-based Ki. All results were obtained using a non-linear least-squares fitting process as described previously (G. Wang & Qi, 2009). Initialization parameters are included in supplemental table A.1. To assess the impact of delay correction methods, delay was estimated jointly (JE), via the leading edge (LE) method, or not at all (no delay correction). The first 36 dynamic frames, representing the first 120 seconds of the acquisition, were used to jointly estimate delay prior to fitting all 66 timepoints for estimation of the rest of the parameters. For ROI-based analysis, the same LE thresholds used in simulations (between 2.5 and 50% of the peak activity in the first 2 minutes) were used to determine the IDIF bolus arrival time t_0 and arrival time at the tissue t_d. Both JE and LE estimates of delay (t_d - t_0) were estimated in 1-second steps and were constrained to be between zero and 50 seconds. The conventional JE method was considered ground truth, such that the optimal LE threshold could be determined across a variety of ROIs. After determining the optimal LE threshold, a single LE threshold was used for kinetic modeling, and the quality of ROI-based and parametric image-derived parameter estimates was assessed using Pearson's *r*.

ROIs were identified in six tissue types: grey matter, liver, lungs, muscle, myocardium, spleen, in addition to the left ventricle blood pool. An additional 28 GUC lesions were delineated based on a threshold of 41% of the maximum standardized uptake value, as recommended by Boellaard *et al*. (2015). All ROIs were manually corrected for subject motion. ROI delineation was performed using PMOD (PMOD Technologies, Zurich, Switzerland).

In order to highlight a variety of tissue types for prototyping of the method, parametric maps

of delay and other kinetic parameters (v_b, K_1, K_i) were generated with both JE and LE methods using the entire image volumes of one representative healthy and one GUC subject. The tissue ROIs listed above were used to generate tissue-specific voxel-wise parameter estimates from the parametric images (supplemental figure A.2). A vascular ROI was also included to assess the impact of delay within the blood pool in the parametric images.

3.3. Results:

3.3.1. Simulations

Delay estimates were determined for different framing schemes and noise levels (e.g., supplemental figure A.1). From the wide range of LE thresholds and CFD attenuation fractions tested, LE results indicate that higher noise levels resulted in only marginal increases in bias and standard deviation of estimated delay times, particularly with 2-second frames and a LE threshold of less than 15%, while CFD bias and standard deviation increased with higher noise levels for attenuation fractions of 15% or less (supplemental table A.2). With 2-second frames, there was less than a 1-second bias in delay for all LE thresholds of 10% or greater, and a 30% LE threshold

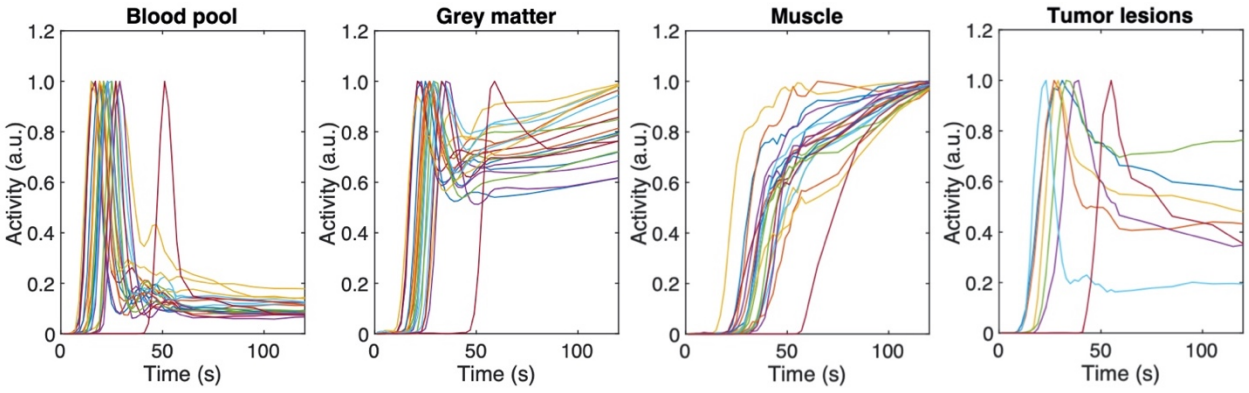

Figure 3.1: Normalized FDG TACs in healthy subject and GUC patient tissues

Figure 3.1: Normalized TACs in a number of healthy subject and GUC patient tissues. Although injection bolus shape was consistent across pooled human subjects, injection time relative to the start of the scan, delay in arrival time to individual tissues, and initial lesion uptake differed. A single lesion is shown per GUC patient for ease of visualization.

led to the lowest bias in delay (0.11-0.18 seconds, supplemental table A.2, bold). As frame length increases from 2 to 10 seconds, the effect of frame length dominates the bias, particularly at higher LE thresholds and higher CFD attenuation fractions. This was mitigated for LE results by increasing the LE threshold to 25% or greater, which reduced bias to < 5 seconds for all noise levels. With a 30% LE threshold, absolute biases for 10 second frames are between 3.80 and 3.96 seconds for all noise levels tested. The CFD method was not investigated further due to its poorer performance on noisy simulated data and reliance on a user-chosen time shift, traditionally based on waveform rise-time (Knoll, 2005). The LE method does not rely directly on the rise-time, making it the more practical method for total-body PET human subject data. Supplemental table A.3 expands upon the LE results showing data for additional frame lengths. The impact of frame length dominates the bias estimates for longer (5- and 10-second) frames and were within 0.5 seconds of each other across the different noise levels at the same LE threshold.

Although a LE threshold of 25% was the most insensitive to noise level, and a threshold of 30% resulted in the lowest biases and standard deviations for 2-second frames, the simulations focus solely on a grey matter TAC with an ideal bolus injection. Therefore, to assess the performance of the LE method on different tissue types with varying kinetics and the effect of time walk, or the over estimation of LE estimates, in slowly rising TACs (e.g., liver), a variety of LE thresholds were tested in human ROI-based analyses.

3.3.2. Human ROI-based Analysis

Tissue-specific TACs were consistent across organ type among subjects (figure 3.1, supplemental figure A.3). The subset of the 28 lesion TACs shown in figure 3.1 demonstrates the heterogeneity of tracer arrival time and metabolism. Since there were no noticeable differences between healthy subject and GUC patient TACs, ROI-based parameter estimates were pooled across the 14 healthy subjects and 7 GUC patients. Average JE and LE delay estimates with their standard errors (figures 3.2A, 3.2B) demonstrate the impact of slower TAC rise-times on the LE estimates of liver and muscle, as compared to grey matter, spleen, and GUC lesions, which all demonstrate a sharp rising edge (supplemental figure A.3). Based on simulation results and the timing walk, or overestimation of delay that occurs for more slowly-rising TACs as LE thresholds are increased in figure 3.2B, a LE threshold of 10% was selected for further ROI-based results and implemented for parametric imaging. As shown in figure 3.2C, there was good agreement between JE and LE methods in the estimation of delay (Pearson's r=0.96, p<0.001, slope: 1.00) with a 10% LE threshold for all ROIs.

The impact of delay correction can be seen in Table 3.1 where parameter estimates were obtained with and without delay correction. With LE-based delay estimation, mean parameter estimates were in agreement with JE results for v_b (r=0.96, p<0.001, slope: 0.98), K_i (r=1.00, p<0.001, slope: 0.99), and K_1 (r=0.97, p<0.001, slope: 0.91) when all regions were pooled (N=154)

(table 3.1, top, supplemental figure A.4). When delay correction was not performed, there was little impact on K_i (r=1.00, p<0.001, slope: 1.02), however v_b (r=0.86, p<0.001, slope: 0.85) and K_1 (r=0.89, p<0.001, slope: 0.89) are poorly estimated in some tissues, including grey matter, spleen, and GUC lesions. When tissues with negative or zero delay (myocardium, lung) were excluded from pooled analyses, K_i remains relatively constant while there was a drop in v_b (69.4%), and K_1 (4.8%) without delay correction (table 3.1).

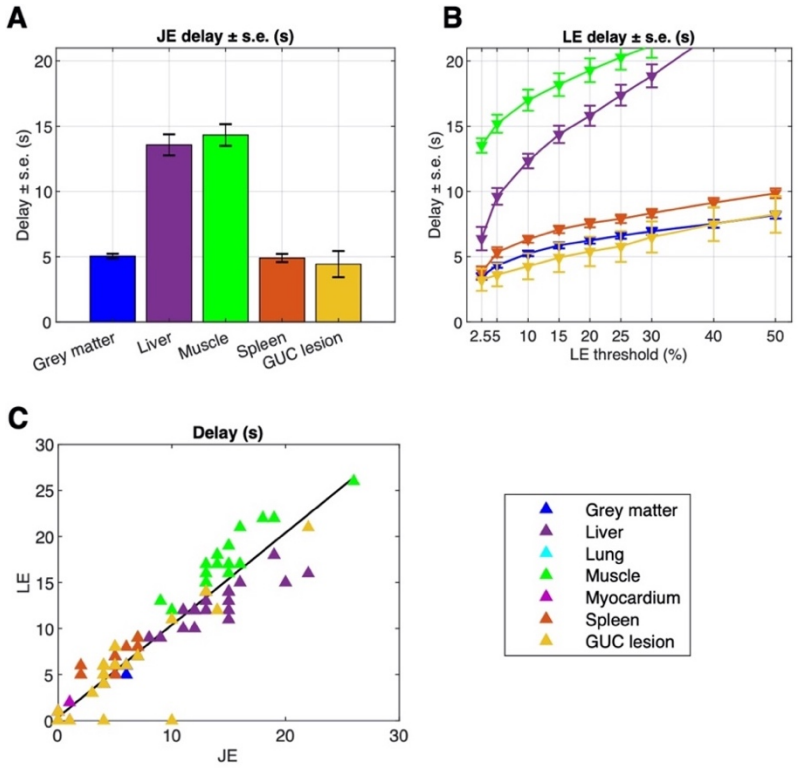

Figure 3.2: Average JE versus LE delay estimates

Figure 3.2: Average JE delay estimates with standard error (s.e.) (A), and LE estimates (B) at thresholds ranging from 2.5 to 50% for different ROIs. As LE threshold increases, LE delay estimates exhibit time walk for tissues with longer rise-times such as the liver (▲) and muscle (▲). Based on A and B, a threshold of 10% was selected for further kinetic analyses. The LE method was in good agreement with JE estimates of delay (C, r=0.96, p<0.001, slope: 1.00) with a 10% threshold across all regions.

Table 3.1: Mean (s.d.) estimated kinetic parameters obtained from pooled regions

	All regions (N=154)					Regions* with positive delay (N=112)				
Parameter	JE		LE		$r^{\dagger}$	JE		LE		$r^{\dagger}$
v_b	0.070	(0.079)	0.076	(0.080)	0.96	0.036	(0.056)	0.044	(0.061)	0.91
K_1	0.553	(0.629)	0.529	(0.584)	0.97	0.600	(0.677)	0.569	(0.618)	0.98
K_i	0.012	(0.017)	0.012	(0.017)	1.00	0.011	(0.014)	0.011	(0.014)	1.00
Delay	5.981	(6.073)	6.377	(6.331)	0.96	8.205	(5.701)	8.732	(5.888)	0.94
k_2	1.213	(1.292)	1.171	(1.277)	0.94	1.133	(1.230)	1.084	(1.188)	0.95
k_3	0.039	(0.069)	0.037	(0.057)	0.97	0.035	(0.064)	0.032	(0.046)	0.96
	All regions (N=154)					**Regions* with positive delay (N=112)**				
Parameter	JE		No delay corr.		$r^{\dagger}$	JE		No delay corr.		$r^{\dagger}$
v_b	0.070	(0.079)	0.050	(0.078)	0.86	0.036	(0.056)	0.011	(0.036)	0.57
K_1	0.553	(0.629)	0.541	(0.622)	0.89	0.600	(0.677)	0.571	(0.656)	0.88
K_i	0.012	(0.017)	0.012	(0.017)	1.00	0.011	(0.014)	0.011	(0.015)	0.99
Delay	5.981	(6.073)	0	0	N.A.	8.205	(5.701)	0	0	N.A.
k_2	1.213	(1.292)	1.205	(1.348)	0.85	1.133	(1.230)	1.085	(1.233)	0.79
k_3	0.039	(0.069)	0.040	(0.063)	0.96	0.035	(0.064)	0.036	(0.057)	0.94

N.A.: Not available.
*excludes lung and myocardium, $^{\dagger}p<0.001$.

Table 3.2 shows the mean and standard deviation estimates of the 42 tissue-parameter pairs. LE estimates were strongly in agreement with JE methods for most tissues, where only five of 38 statistically significant comparisons had a Pearson's $r < 0.8$. The LE method did not agree with JE results only in a limited number of areas, including some liver and spleen ROIs when estimating v_b.

Table 3.2: Mean (s.d.) estimated kinetic parameters for healthy subjects (N=14) and GUC patients (N=7)

	Grey Matter					Liver					Lung				
Parameter	JE		LE		r*	JE		LE		r*	JE		LE		r*
v_b	0.030	(0.006)	0.030	(0.006)	0.98	0.001	(0.003)	0.001	(0.005)	N.S.	0.128	(0.039)	0.128	(0.039)	1.00
K_1	0.107	(0.017)	0.107	(0.018)	1.00	0.660	(0.286)	0.636	(0.291)	0.98	0.023	(0.012)	0.023	(0.012)	1.00
K_i	0.031	(0.007)	0.031	(0.007)	1.00	0.002	(0.002)	0.002	(0.001)	0.81	0.000	(0.000)	0.000	(0.000)	1.00
Delay	5.048	(0.805)	5.238	(0.944)	0.77	13.571	(3.723)	12.333	(2.536)	0.87	0.000	(0.000)	0.000	(0.000)	N.A.
k_2	0.165	(0.027)	0.163	(0.029)	0.95	0.765	(0.374)	0.737	(0.381)	0.98	0.205	(0.090)	0.205	(0.090)	1.00
k_3	0.067	(0.012)	0.066	(0.013)	0.99	0.002	(0.002)	0.002	(0.002)	0.84	0.001	(0.004)	0.001	(0.004)	1.00

	Muscle					Myocardium					Spleen				
Parameter	JE		LE		r*	JE		LE		r*	JE		LE		r*
v_b	2.3E-4	(4.7E-4)	0.001	(0.001)	0.69	0.190	(0.063)	0.192	(0.068)	0.98	0.044	(0.025)	0.083	(0.029)	N.S.
K_1	0.026	(0.012)	0.026	(0.012)	1.00	0.832	(0.307)	0.820	(0.356)	0.81	1.593	(0.556)	1.458	(0.467)	0.99
K_i	0.002	(0.000)	0.002	(0.000)	1.00	0.029	(0.024)	0.028	(0.024)	1.00	0.003	(0.001)	0.003	(0.001)	0.99
Delay	14.333	(3.812)	17.000	(3.715)	0.94	0.095	(0.301)	0.190	(0.512)	N.S.	4.905	(1.411)	6.333	(1.278)	0.71
k_2	0.249	(0.142)	0.249	(0.136)	1.00	2.651	(1.044)	2.597	(1.215)	0.78	2.867	(0.980)	2.709	(0.882)	1.00
k_3	0.016	(0.006)	0.016	(0.006)	1.00	0.099	(0.088)	0.098	(0.088)	1.00	0.006	(0.003)	0.006	(0.003)	0.99

	GUC lesions (N=28)				
Parameter	JE		LE		r*
v_b	0.089	(0.086)	0.089	(0.092)	0.93
K_1	0.609	(0.614)	0.605	(0.573)	0.92
K_i	0.017	(0.016)	0.018	(0.016)	0.99
Delay	4.429	(5.295)	4.250	(5.254)	0.90
k_2	1.496	(1.213)	1.443	(1.272)	0.79
k_3	0.071	(0.114)	0.062	(0.074)	0.97

N.A.: Not available. N.S.: Not significant.

* p<0.001.

3.3.3. Parametric Imaging

Voxel-wise LE results were assessed using datasets from one representative healthy volunteer and one representative GUC subject. Using a high-performance computational node (Intel Xeon Gold 2.6 GHz, 24-core processor), JE were produced at an approximate rate of 180 voxels/s, while LE parametric images were produced at an approximate rate of 1,200 voxels/s, representing a 6.7-fold increase in computational efficiency. Parametric results were in agreement with ROI-based methods, though were slightly overestimated for both JE (r=0.97, p<0.001, slope: 1.05) and LE (r=0.99, p<0.001, slope: 1.06) (supplemental figure A.5). Example delay and K_i maps are shown

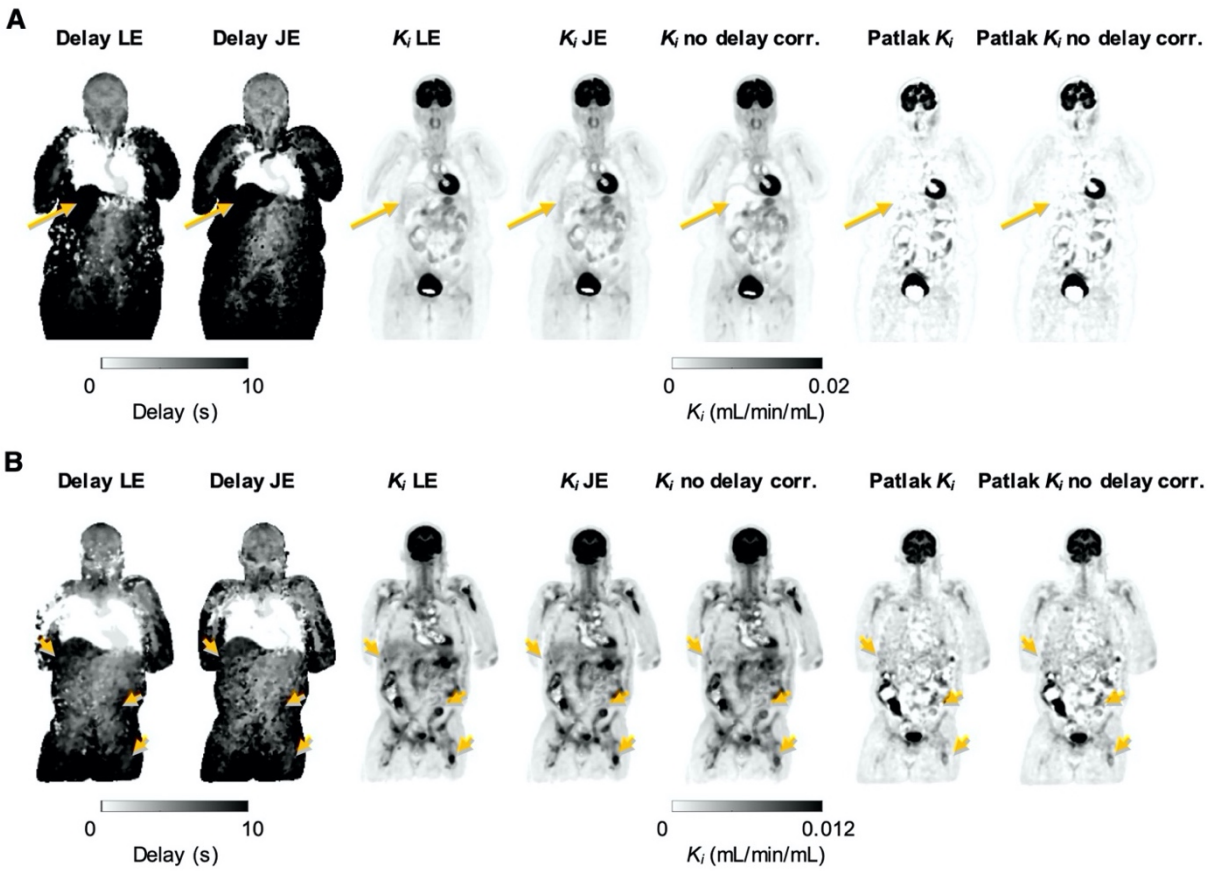

Figure 3.3: Maximum intensity projection (MIP) parametric images of delay and K_i

Figure 3.3: Maximum intensity projection (MIP) parametric images of delay and K_i for a representative healthy subject (A) and a GUC patient (B) generated using four coronal slices (1.6 cm thick). 10% LE threshold-derived delay maps showed some differences compared to JE delay maps, particularly close to the injection site in the right antecubital, but are broadly in agreement across the rest of the body. Compartment modeling-based K_i maps were similar with JE and LE methods of delay correction, and both methods resulted in improved liver signal (A, arrows) and lesion contrast (B, arrows) compared to Patlak results, or to when no delay correction was implemented.

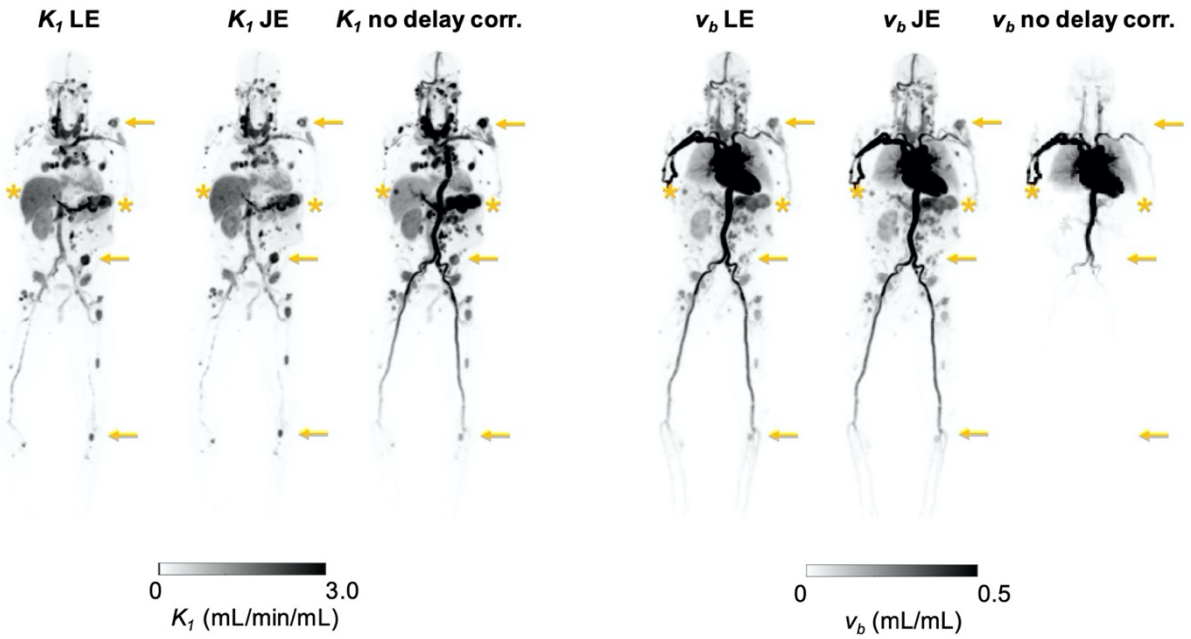

Figure 3.4: MIPs of K_1 and v_b parametric maps for a representative GUC patient

Figure 3.4: MIPs of K_1 (left) and v_b (right) parametric maps for a representative GUC patient. Overall, LE-derived parametric images were similar to JE-based images. Without delay correction, K_1 was increased while v_b was underestimated in much of the abdomen and lower body compared to JE-based v_b. Multiple GUC lesions (arrows) demonstrated increased K_1 and v_b when delay correction was applied, while vessels in the legs and some lesions in the upper abdomen and liver (asterisks) showed a reduction in K_1 and an increase in v_b.

in figure 3.3. LE-derived delay maps showed some artifacts near the injection site compared to JE delay maps, but results were broadly comparable across most tissues. K_i was similar between JE and LE, and demonstrated improved K_i contrast in the liver and GUC lesions (arrows) compared to K_i computed with no delay correction or via Patlak plot (figure 3.3, supplemental table A.4). GUC subject maximum intensity projection images of K_1 and v_b are shown in figure 3.4, where delay correction improved visualization of lesions in the thorax, lower torso, and legs. Like the ROI-based results in tables 3.1 and 3.2, relative to when no delay correction was performed, voxel-

level delay correction resulted in improved estimation of lesion v_b and K_1 (figure 3.4), which are both sensitive to the early phases of the scan.

Both representative subjects showed some disagreement of LE delay in the muscle and spleen relative to JE delay, though this did not greatly impact K_i or v_b estimates. Scatter plots comparing JE and LE results in a representative healthy subject (supplemental figure A.6) demonstrate agreement in the estimation of delay (r=0.99, p<0.001, slope: 1.01) across organs. Estimates of v_b (r=1.00, p<0.001, slope: 1.00) and K_i (r=1.00, p<0.001, slope: 0.99) were in strong agreement with JE results. Although not shown, K_1 LE-based estimates also agreed with JE, but were underestimated (r=0.97, p<0.001, slope: 0.91).

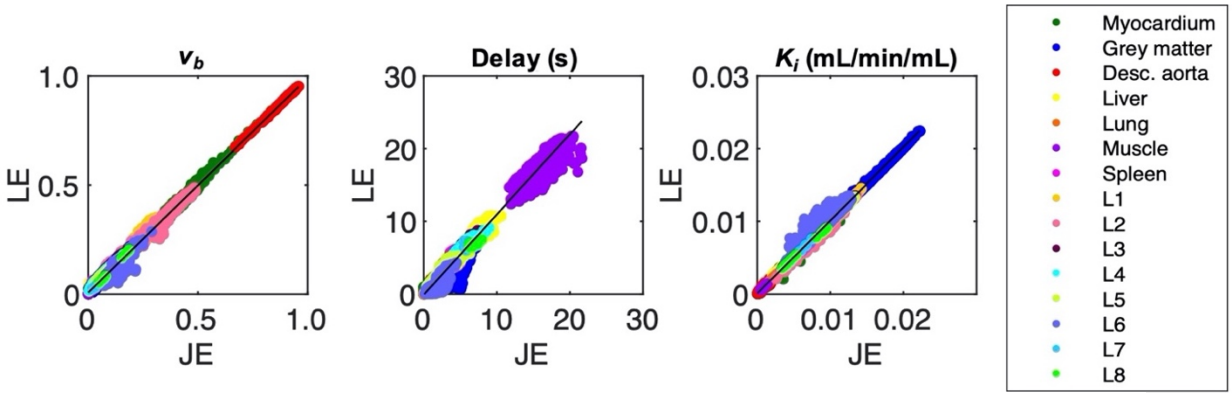

Figure 3.5: Parametric LE versus JE results for a GUC patient.

Figure 3.5: Parametric LE versus JE results for a GUC patient were compared across a number of regions including 8 lesions (L1-L8). Delay is slightly overestimated (r=0.99, p<0.001, slope: 1.10) overall, and is underestimated in a number of TACs, namely from muscle, lesions and grey matter. LE v_b (r=1.00, p<0.001, slope: 0.98) and K_i (r=1.00, p<0.001, slope: 1.00) estimates demonstrate nearly 1:1 ratios with JE.

GUC voxel-wise estimates of delay were similarly in disagreement in some muscle, spleen, and lesion voxels, and overall, delay was slightly overestimated (r=0.99, p<0.001, slope: 1.10) (figure 3.5). There was strong agreement for v_b (r=1.00, p<0.001, slope: 0.98) and K_i (r=1.00,

p<0.001, slope: 1.00). Although not shown, GUC subject K_1 estimates were also in agreement (r=0.99, p<0.001, slope: 0.97) between LE and JE methods.

3.4. Discussion

Here we demonstrate, at both the ROI and voxel level, the feasibility of using pulse timing methods (LE and CFD) as a surrogate for jointly estimating tracer delay using the first 120 seconds of data, across a wide range of tissue types present in total-body PET datasets. Noise, in addition to temporal framing, plays an important role in the choice of threshold in the LE method. In simulations, LE with a 10% threshold or greater provided satisfactory delay bias and standard deviation in short frames at most noise levels, but a 30% threshold resulted in the lowest measured bias and standard deviation at all noise levels. However, the shape of the TAC itself is important, and may explain the discrepancies between simulations and acquired TACs in determining the optimal LE threshold for grey matter. Further, tissues with a long rise-time such as the liver suffer from time walk, and spillover from the blood pool can cause early triggering and thus over and underestimation of delay respectively. Threshold optimization may be necessary for these tissues. Since the simulation data showed no advantage in using the CFD approach, the simpler LE method was used for human studies.

After assessing regional delay estimates from various LE thresholds, a 10% threshold was implemented for all human analyses. JE and LE methods were in agreement for all estimated kinetic parameters at both ROI and voxel levels. v_b and K_1 estimates were sensitive to delay correction, while K_i was only impacted by delay correction in the liver and GUC lesions of the parametric images. Improved estimation of v_b and K_1 has implications for perfusion imaging with radiotracers with rapid kinetics utilized for first-pass imaging (e.g., ^{15}O-water).

The bolus shape is another important consideration; the simulation results indicate that LE methods work well with a sharp bolus peak for the IF with respect to the frame length, such that there is as little timing walk in the tissue and IF curves as possible. Therefore, these methods are expected to be translatable to other tracers delivered via bolus injection, but may need further investigation for continuous infusion or dual-tracer injection paradigms.

Although we implemented model selection in our parametric analyses, special-case tissues (e.g., liver, lung) require additional models that consider dual input functions and dispersion which were not implemented here, but will be a part of our future work. Patient motion is another major challenge with total-body parametric imaging. Short frames capture respiratory and cardiac motion, while any gross motion throughout the scan is also captured. In practice, application of these methods will likely benefit greatly from incorporation of motion correction in total-body PET (Y. Wang et al., 2021). Here, we performed simple manual correction of motion for our ROIs, and selected image datasets with limited motion for parametric analysis.

While LE delay correction can be implemented with the Patlak analysis, delay correction has a limited impact on Patlak K_i, indicating that improved lesion contrast seen in this study was a result of implementation of full compartment modeling with delay correction.

3.5. Conclusions

In this work we apply pulse timing methods to dynamic PET images to estimate the arrival time of the radiotracer bolus in ROIs and in every voxel in the body. We have demonstrated that pulse timing methods can be an efficient surrogate for JE. Moreover, LE and JE methods of delay correction provided K_i, v_b, and K_1 estimates that were in good agreement and substantially improved parametric results compared to fitting results when no delay correction was performed, or compared to Patlak analysis. Further, at the voxel level, LE estimates were in agreement with

JE across a variety of tissue types for both healthy and GUC subjects. The results suggest delay correction should be implemented for total-body PET kinetic modeling using short (<5 second) frames, and implementing the LE method instead of JE will allow for efficient correction of delay.

4. Chapter 4: [^{11}C]-butanol total-body PET perfusion imaging

4.1. Introduction

Perfusion and blood flow imaging using positron emission tomography (PET) has been clinically utilized in the assessment of single-organ flow-related diseases such as stroke (Ackerman et al., 1981; Baron et al., 1982, 1984; Z. Wang et al., 2020) and myocardial ischemia (Chareonthaitawee et al., 2017; Marshall et al., 1983; Murthy et al., 2018; Schwaiger, 1994). Perfusion imaging of the myocardium is of particular importance for its role in assessing myocardial viability after the onset of ischemia in cases where revascularization, or reopening of the affected vasculature, is being considered. Patients typically undergo a resting flow study with a perfusion tracer such as [^{13}N]-NH_3, followed by an [^{18}F]-fluorodeoxyglucose (FDG) static acquisition. A mismatch of perfusion and metabolism (i.e., low levels of perfusion but high FDG uptake) is indicative of hibernating myocardium, in which revascularization can lead to full recovery of myocardial function (Marshall et al., 1983; Yamagishi et al., 1999, 2000). However, if no abnormalities are seen in the resting perfusion images, no FDG acquisition is recommended (Manapragada et al., 2021). Therefore, careful characterization of myocardial perfusion is necessary for assessing myocardial ischemia.

However, there are limitations with the more commonly used perfusion tracers such as [^{15}O]-water, [^{82}Rb]-RbCl, and [^{13}N]-ammonia. Not only do these tracers suffer from large positron ranges and reduced image quality relative to ^{18}F and ^{11}C-based tracers (Sánchez-Crespo et al., 2004), but also, due to the flow and tissue dependence of the extraction fraction, *E,* perfusion with these tracers is underestimated at high flow rates (Berridge et al., 1991; Glatting et al., 1997; Hack et al., 1983; Herscovitch et al., 1987; Phelps et al., 1981; Schelbert et al., 1981). *E* is dependent on the permeability-surface area coefficient, and is impacted by the size, structure and charge of the tracer molecule itself and its interactions with the tissue, as discussed in section 1.7.1. Reduced

extraction fraction even of [^{15}O]-water has been observed in the brain, due to the selectivity of the blood-brain barrier; when perfusion is above 0.60 ml·min^{-1}·cm^{-3}, CBF is underestimated (figure 1.4) (Berridge et al., 1991; Morris et al., 2004; Raichle et al., 1976). Despite this underestimation and its short half-life of 2 minutes, [^{15}O]-water has been used extensively for studying changes in cerebral blood flow (CBF) and has produced repeatable results in a number of studies with the subject at rest (Kaufmann et al., 1999; Puig et al., 2020; Siegrist et al., 2006). But perhaps the larger limiting factor in the clinical adoption of [^{15}O]-water in the US is that it is not FDA approved for myocardial perfusion studies, and thus has been utilized in research settings only (Murthy et al., 2018).

This flow-dependent extraction is a challenge for measuring high flow rates, which can occur either inherently due to organ-specific flow rates (e.g., kidney cortex, spleen), or due to a stress stimulation by an external pressor, such as exercise, injection of adenosine, increased partial pressure of CO_2, or a visual stimulus (Berridge et al., 1991; Murthy et al., 2018; Quarles et al., 1993). Thus, clinical perfusion studies involving a rest-stress paradigm may benefit from the introduction of a more highly extracted tracer, that will be able to further distinguish between high and low flow regions. One example of this is myocardial perfusion imaging, which utilizes paired acquisitions to obtain images at rest and during stress, to assess viability of the myocardium and calculate the myocardial flow reserve, which is the ratio of the stress to rest images.

Butanol has been used as a perfusion agent in both human (Berridge et al., 1991; Hack et al., 1983) and preclinical (Gjedde et al., 1980; Knapp et al., 1985; Takagi et al., 1984) settings. As discussed briefly in chapter 1, [^{11}C]-butanol is metabolized in a similar manner to ethanol (Carlson, 1994; Knapp et al., 1985; Raichle et al., 1976). Most of the metabolism occurs in the liver, where alcohol dehydrogenases break down [^{11}C]-butanol into [^{11}C]-butyric aldehyde and [^{11}C]-butyric

acid, the latter of which can be broken down via beta-oxidation to [^{11}C]-CO_2 (Knapp et al., 1985). Since these metabolites do not impact the first pass-kinetics of [^{11}C]-butanol (DiVincenzo & Hamilton, 1979; Knapp et al., 1985), it is possible to perform first-pass perfusion imaging of the entire body without the need to correct for tracer metabolism. Due to the short time of acquisition, the improved sensitivity and extended axial field of view (FOV) of total-body PET are vital to multi-organ [^{11}C]-butanol perfusion imaging.

In this work, baseline studies were utilized in the establishment of total-body PET [^{11}C]-butanol kinetic modeling methods. Then, the reproducibility and sensitivity of total-body PET to differences in perfusion was assessed in this work in three ways: (i) via baseline or resting test-retest studies, (ii) through a rest-stress paradigm generated via the cold pressor test (CPT), and (iii) by assessing regional ischemia in a patient with peripheral artery disease (PAD).

4.1.1. The cold pressor test (CPT)

The use of a cold stimulus has been previously assessed as a noninvasive alternative to pharmacologic or exercise-based stressors in the quantification of blood flow via PET (Di Piero et al., 1994; Kjaer et al., 2003; Petrovic et al., 2000; Prior et al., 2007; Schindler et al., 2007; Siegrist et al., 2006). More widely, CPT, which involves submerging a limb in cold or ice water for a short period of time, has been used to assess the sympathetic—or fight-or-flight response—to cold stimulus or pressor (Bachmann et al., 2018; Micieli et al., 1994; Velasco et al., 1997). In response to the CPT, norepinephrine is released into the blood via post-ganglionic sympathetic neurons, leading to increases in heart rate and blood pressure. Although many blood vessels undergo vasoconstriction as a result of the interaction between norepinephrine and alpha-1 adrenergic receptors, the blood vessels that supply blood to tissues that are more vital to survival (coronary artery, arteries supplying blood to skeletal muscle) benefit from the increased blood flow, due to

the activation of pro-vasodilatory beta-2 adrenergic receptors that counteract the effects of alpha-1 (Bangash et al., 2012; Belletti et al., 2020; McCarty, 2016). The response of various tissues to the CPT or a similar pressor are dependent on distribution of catecholamines like norepinephrine and their associated G-protein coupled receptors.

CPT has been shown to alter flow in a number of organs with perfusion PET imaging. In the myocardium, flow has been shown to increase by approximately 40-80% (Schindler et al., 2004; Siegrist et al., 2006). Small regional (<10%) increases (Di Piero et al., 1994; Petrovic et al., 2000) in cerebral blood flow are likely, but to our knowledge, no global increase has been observed in cerebral blood flow with the CPT (Wilson et al., 2005), likely due to cerebral autoregulation. Hepatic blood flow has been shown to increase by 80% in a rest-stress paradigm with [^{82}Rb]-RbCl and a pharmacological pressor, adenosine (Keramida et al., 2020). Renal blood flow has also been shown to drop slightly (Kannenkeril et al., 2021), and splenic blood flow has been shown to increase by approximately 40% (Galea et al., 2019) with the CPT, but will decrease with enough adenosine (Manisty et al., 2015). In this work, total-body PET was used to characterize organ-specific responses to the CPT.

4.1.2. Peripheral artery disease (PAD)

Patients with peripheral artery disease (PAD) have stenoses or occlusions in peripheral vessels that reduce blood flow to the limbs, cause local ischemia, and lead to differences in perfusion between muscle groups and opposing limbs. The classic symptom of PAD is muscle pain while exercising, which is called intermittent claudication. Severe PAD can lead to ulcers and amputation without appropriate intervention. PAD affects 6.5 million people in the US who are 40 years and older (Virani et al., 2021), and is typically diagnosed using a blood pressure cuff and the ankle-brachial index (ABI), which is defined as the ratio of the arterial blood pressure in the leg to that

of the arm. A lower index is indicative of more severe disease in the leg, while a ratio much greater than 1 would indicate disease in the arm. Despite the fact that the diagnosis of PAD is fast and accessible, it is thought to be underdiagnosed globally since many individuals are unaware of the existence of PAD and are either asymptomatic or do not experience traditional symptoms such as intermittent claudication (Fowkes et al., 2017; Virani et al., 2021). The risk of additional cardiovascular events and death is similar to that of other cardiovascular diseases, such as coronary artery disease (Virani et al., 2021), thus functional characterization of PAD may be beneficial to the clinical decision-making. Here, total-body PET is used to quantify regional differences in perfusion, but in future work could also be used to monitor disease progression and the effect of interventions.

As discussed in chapter 1, blood flow to all the tissues in the body can be measured simultaneously with total-body PET/CT systems. Further, using an image-derived input function (IDIF), quantitative total-body perfusion measurements can be made with minimal invasiveness. However, tissues of interest across the body have a wide range of possible perfusion values and kinetics. Here, the initial methodology and results for an ongoing [^{11}C]-butanol perfusion study are discussed, where methods are introduced to reliably and reproducibly estimate perfusion across a number of organs throughout the body. The sensitivity of these methods to intra-subject changes in total-body PET perfusion estimates was assessed in two individuals: one healthy volunteer using the CPT, and one patient with PAD at rest.

4.2. Underlying materials and methods:

4.2.1. Pilot study details

With Institutional Review Board approval and written informed consent, 6 healthy volunteers (2 male, 4 female, body mass index (BMI): 20.9-30.0 kg/m^2, 28-64 years) and 1 patient with PAD

(BMI: 23.4 kg/m^2, 66 years) were injected with a bolus of [^{11}C]-butanol (mean: 279.1, range: 190.6-348.6 MBq). The dynamic acquisitions on the uEXPLORER scanner (Spencer et al., 2021) were approximately 30 minutes in length, except for one acquisition that ended with a scan time of 10 minutes. A low-dose CT scan was acquired prior to the PET acquisition for attenuation correction and initial ROI delineation. Healthy volunteers underwent either two baseline studies to assess reproducibility (group 1) or underwent a baseline and a CPT study (group 2), while the PAD subject had a single visit (group 3). Visits occurred up to 2 weeks apart (table 4.1). All eight baseline studies from groups 1 and 2 were pooled for this work.

For group 2, CPT and baseline visits were randomly ordered. During the CPT visit, commercially available foot therapy pads (Polar Products, Ohio, USA) were applied to both feet of the subject prior to the CT acquisition. Starting after the CT scan but approximately 60 seconds prior to the start of the dynamic PET acquisition, ice water was continuously pumped through the conformable boots. The pump was allowed to run for up to five minutes, or until the subject expressed discomfort.

Table 4.1: [^{11}C]-butanol pilot study acquisition groupings

Group	Population	No. of subjects	No. of acquisitions	Days to second visit	Injected dose (MBq)
1	Healthy volunteers	3	6	9.7±3.8	284.8±35.7
2	Healthy volunteers	3	4*	7	267.8±55.3
3	PAD	1	1	-	290.4

Mean (s.d.) reported where appropriate.
* of the 3 subjects in group 2, 1 had a complete (baseline + CPT) series of studies, 1 completed the CPT visit only, and 1 completed the baseline study only.

Vendor-provided TOF-OSEM software was used to perform the reconstructions (20 subsets, 4 iterations) and corrections for attenuation, scatter, randoms, deadtime and decay (Leung, Berg, et al., 2021). No point spread function modeling was applied. To assess the impact of spatial and temporal resolution changes, images from three baseline acquisitions were reconstructed with a

variety of framing protocols and image matrix sizes (table 4.2). For each one of the three representative baseline acquisitions, eight reconstructed dynamic datasets—encompassing two voxel sizes (2.344x2.344x2.344 and 4.0x4.0x4.0 mm^3), and four framing protocols (5m12, 30m29, 5m52, 2m90)—were used to assess the impact of spatial and temporal resolutions on kinetic modeling. However, initial investigations—including TIDA plots and sensitivity and identifiability analysis of the kinetic parameters—were performed with images reconstructed with 30m29 framing and 4.0x4.0x4.0 mm^3 voxels.

Table 4.2: Temporal framing and reconstructed image sizes

Designation*	Shortest frame	Framing	Matrix size	Voxel size
5m12	10 s	6x10 s, 4x30 s, 2x60 s	150x150x486x12	4.0 x 4.0 x 4.0 mm^3
$5m12_{2.3}$	10 s	6x10 s, 4x30 s, 2x60 s	256x256x828x12	2.3438 x 2.3438 x 2.344 mm^3
30m29	5 s	12x5 s, 6x10 s, 6x30 s, 5x300 s	150x150x486x29	4.0 x 4.0 x 4.0 mm^3
$30m29_{2.3}$	5 s	12x5 s, 6x10 s, 6x30 s, 5x300 s	256x256x828x29	2.3438 x 2.3438 x 2.344 mm^3
5m52	2 s	30x2 s, 12x5 s, 6x10 s, 4x30 s	150x150x486x52	4.0 x 4.0 x 4.0 mm^3
$5m52_{2.3}$	2 s	30x2 s, 12x5 s, 6x10 s, 4x30 s	256x256x828x52	2.3438 x 2.3438 x 2.344 mm^3
2m90	1 s	60x1 s, 30x2 s	150x150x486x90	4.0 x 4.0 x 4.0 mm^3
$2m90_{2.3}$	1 s	60x1 s, 30x2 s	256x256x828x90	2.3438 x 2.3438 x 2.344 mm^3

*Notation XmY denotes acquisition length of X minutes with a total number of frames Y. A subscript of 2.3 indicates a voxel size of 2.3438 x 2.3438 x 2.344 mm^3

4.2.2. ROI delineation

Tissue time activity curves (TACs) were derived from large or whole-organ ROIs for grey matter, white matter, kidney, liver, lungs, skeletal muscle regions (splenius capitis, deltoid, psoas, left and right whole thighs, left and right whole calves), bone marrow, myocardium, pancreas, spleen, thyroid and rectum using PMOD (PMOD Technologies, Zurich, Switzerland). With the exception of the deltoid muscle, which demonstrated high spillover in the arm in which the bolus was

delivered, all regions were drawn bilaterally and averaged for kinetic modeling, where applicable. The CT scan was used for the initial delineation of the ROIs. The ROIs were further modified to account for the effects of subject motion in a tissue-dependent manner through two image visualization strategies: (i) the use of a 0-3.5 minute average image and (ii) avoidance of visible motion or spillover effects in high-contrast frames. ROI delineation was performed using the 30m29 images. For strategies implemented for different tissue types, see table 4.3.

A volumetric region of interest (ROI) was drawn in the descending aorta (DA) and the right ventricle (RV) for use as the IDIFs. The DA IDIF was used for all tissues except for the lungs, where the RV IDIF was used.

Table 4.3: Tissue-dependent ROI delineation strategies for [^{11}C]-butanol

Region	(i) Average image	(ii) High-contrast frames	Rationale
IDIF (DA, RV)	x	x	Gross cardiac motion and first-pass partial volume effects and can be visually assessed with (i) and (ii) respectively
Grey matter	x		Limited physiologic motion. Spillover can be avoided using thresholding and morphological operations of (i)
White matter	x		Limited physiologic motion. Spillover can be avoided using thresholding and morphological operations of (i)
Kidney	x	x	Respiratory motion may lead to overlap of the ROI with the liver or spleen, which may be noticed in (i) and (ii)
Liver	x	x	Respiratory motion may lead to overlap of the ROI with the lung or kidney, which may be noticed in (i) and (ii)
Lung	x	x	Respiratory motion may lead to overlap of the ROI with the myocardium, liver, or spleen, which may be noticed in (i) and (ii)
Skeletal Muscles	x	x	CT-based ROIs can be further adjusted via threshold to avoid large vessels with (ii), and also modified to account for any motion between CT and PET acquisitions using (i)
Bone Marrow	x		Limited physiologic motion. Spillover can be avoided using thresholding and morphological operations
Myocardium	x	x	Gross cardiac motion can be addressed primarily with (i). RV spillover was accounted for by (ii)
Pancreas	x	x	High signal in (i). (ii) was useful for reducing the impact respiratory motion
Spleen	x	x	High signal in (i). (ii) was useful for reducing the impact respiratory motion
Thyroid		x	Low signal, thus beneficial to use (ii) in addition to the CT
Rectum	x		CT can be used as primary reference, but limited physiologic motion and sufficient signal allows for further threshold-based adjustment with (i)

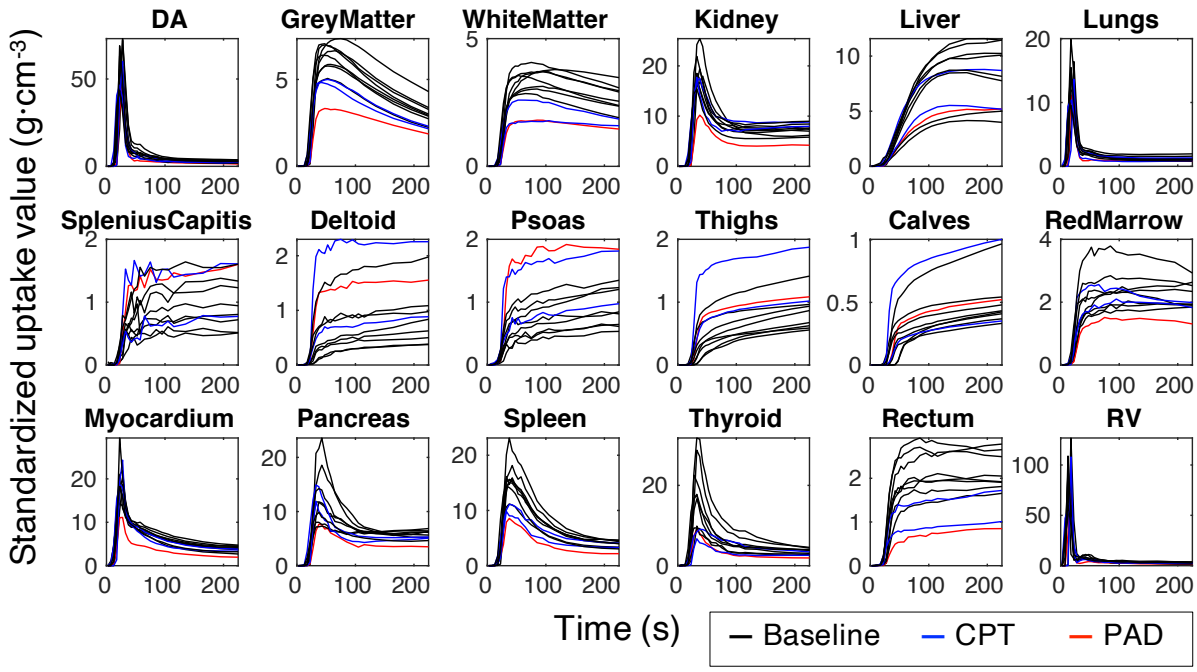

Figure 4.1: ROI-based [^{11}C]-butanol TACs for all acquisitions

Figure 4.1: ROI-based [^{11}C]-butanol TACs for all acquisitions, shown from 0 to 3.5 mins of the dynamic PET 30m29 reconstruction protocol. Baseline, CPT, and PAD acquisitions across all participants are shown in black, blue, and red lines respectively. The descending aorta (DA) was used as the IDIF for all tissues except the lungs, where the right ventricle (RV) was more appropriate. After performing the fitting process, parameter estimates in the skeletal muscle regions (splenius capitis, deltoid, psoas, left calf, and right calf) were averaged.

In figure 4.1, IDIFs and ROI-based TACs across acquisitions show consistency in shape from region to region, while the magnitude varies from subject to subject. TACs from PAD subject (figure 4.1, red lines) show the lowest uptake for many tissues, but have high uptake in the skeletal muscle regions.

4.2.3. Total image-derived activity (TIDA)

Total image-derived activity (TIDA), as discussed in chapter 2, can be used to assess the quantitative performance of a total-body PET/CT system like the uEXPLORER and also can be used to assess excretion of activity from the body. TIDA and TIDA bias for each frame *m* is defined as:

$$TIDA(m) = V \times \sum_i A_i\,(m) \tag{4.1}$$

$$TIDA\ bias(m) = 100\% \cdot \frac{TIDA(m) - i.d.}{i.d.} \tag{4.2}$$

where V is the voxel volume in milliliters, $A_i(m)$ (MBq/ml) is the activity concentration of pixel i in frame m and $i.d.$ is the injected dose in megabecquerels. Based on liquid chromatography, Knapp et al. found 3 metabolites present in the plasma fraction of the blood, the earliest of which was [^{11}C]-CO_2 at 3.7 minutes (1985). Since no blood sampling was performed in this study, TIDA curves for [^{11}C]-butanol were also used to verify a lack of early metabolism for the purposes of kinetic modeling.

As seen in figure 4.2, there was an approximately 10% drop in TIDA over the course of the 30-minute scan. This drop off is due to the exhalation of [^{11}C]-CO_2. However, the TIDA curves for the first five minutes of the butanol studies are relatively flat in comparison, and thus tracer metabolism during the first 4-5 minutes can be safely ignored, as demonstrated previously by others (DiVincenzo & Hamilton, 1979; Knapp et al., 1985). Thus, the first 4.5 minutes were used for kinetic modeling, and the metabolite fraction over this period was assumed to be negligible.

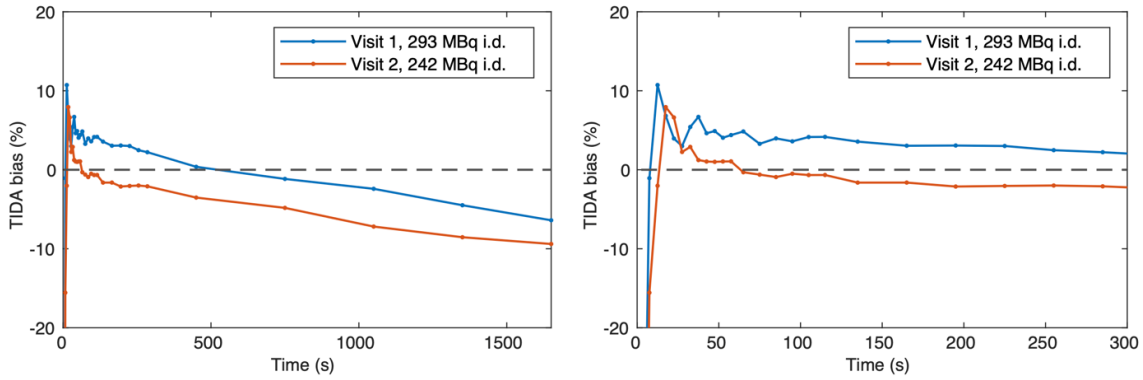

Figure 4.2: TIDA bias for test-retest [^{11}C]-butanol acquisitions

Figure 4.2: TIDA bias plots of a representative baseline test-retest subject who underwent 30-min dynamic [^{11}C]-butanol acquisitions. As shown in the left plot, the TIDA bias curve decreases over the course of a 30-minute study, reflecting the loss of activity through the exhalation of [^{11}C]-CO_2. However, as shown in the inset on the right, the TIDA bias curves remain flat in the first 3.5 minutes of the study, confirming that metabolic losses of carbon-11, at least in the form of exhaled [^{11}C]-CO_2 gas, is negligible during the first pass of the bolus as determined previously (DiVincenzo & Hamilton, 1979; Knapp et al., 1985).

4.2.4. Investigation of factors involved in kinetic modeling

For the fitting of individual tissue TACs, the following factors were considered in the subsequent sections to ensure confidence in the resulting parameter estimates: acquisition time (AT), or the delay-corrected total time of the TAC used for kinetic modeling; optimal temporal framing and reconstructed image size; and use of an appropriate compartment model and associated IDIF corrections.

An overarching understanding of the quality of the fitting results was first assessed through sensitivity and identifiability analyses in section 4.3, during which the compartment model was fixed for each tissue. Based on preliminary fitting results, a 1T4P model was implemented for all tissues except for the liver, where the 1T6P model was used. AT was investigated as part of the

sensitivity analysis and subsequently fixed. As will be described in section 4.4, a number of image reconstructions were performed in a subset of baseline acquisitions to investigate the impact of temporal framing and voxel size on kinetic parameter estimates.

Section 4.5 focuses on kinetic model selection. For each regional tissue TAC, three compartment models were implemented, where the more complicated models included additional corrections to the input functions: (*i*) a 1-tissue, 4-parameter (1T4P) model (v_b, K_1, k_2, delay correction), (*ii*) a 1-tissue, 5-parameter (1T5P) model (v_b, K_1, k_2, delay, dispersion) and (*iii*) a 1-tissue, 6-parameter (1T6P) model (v_b, K_1, k_2, delay, dispersion, and contribution from a second blood input function) (G. Wang et al., 2018). v_b is the unitless blood volume fraction of the tissue TAC, K_1 ($ml \cdot min^{-1} \cdot cm^{-3}$) represents blood flow, and k_2 (min^{-1}) represents the washout rate constant from the tissue back into systemic circulation. Delay correction was performed using the leading edge (LE) method (E. J. Li et al., 2021), where a trigger threshold based on a percent of the peak activity was used to determine the time delay between the bolus arrival in the IDIF and a given tissue. LE delay estimates were constrained to values between -10 and 50 seconds, allowing for negative delay to tissues such as the lung and the myocardium, where the bolus arrival occurs earlier in the acquisition than it does within the descending aorta IDIF. Since this method results in tissue type and frame-dependent biases of delay (E. J. Li et al., 2021), two sets of tissue-specific LE thresholds were implemented, to account for differences in TAC shape for the high (1 and 2 seconds) and low (5 and 10 seconds) temporal resolution reconstructions.

Model selection was performed at the ROI level by comparing the Akaike Information Criterion (AIC) and parameter estimates at two different minimal frame lengths from the 5m52 and 30m29 framing protocols (2 and 5 s minimum frame sizes respectively). As defined in chapter 1, AIC with a correction for small sample sizes was implemented as follows:

$$AIC = M \cdot \ln\left(\frac{WRSS}{M}\right) + 2N + \frac{2N(N+1)}{M-N-1}, \quad WRSS = \sum_m^M w_m (c_{m,fit} - c_m)^2 \tag{4.3}$$

where M is the number of frames, N is the number of parameters included in the modeling process, and WRSS is the residual sum of squares. For the WRSS, w_m represents a weighting factor, which in this work is equal to 1, and c_m and $c_{m,fit}$ represent the measured TAC and fitted model result respectively. Because AIC is heavily influenced by the number of frames, 2 and 5-second results were considered separately.

The optimal reconstruction protocol (i.e., the temporal framing) and choice of model were then fixed, and the kinetic parameter estimates for ROI-based TACs and voxel-level dynamic image data were assessed. For parametric imaging, dynamic image data were smoothed as described previously for parametric kinetic modeling of representative acquisitions for each study group (G. Wang & Qi, 2015). Since parametric images were generated with a minimum frame size of 5 seconds, a lower LE threshold of 1% was used for delay correction, as compared to chapter 3, where 2-second frames and a 10% LE were utilized for FDG image data. An AT of 3.5 minutes was used for all voxels. Parametric model selection was assessed with AIC.

4.2.5. Validation of methods

Baseline tissue-specific parameter estimates from this work were compared with previously published literature values. The literature search for K_1 was limited to reported values using PET/CT perfusion agents, and more specifically, [^{11}C]-butanol, [^{15}O]-water, and [^{15}O]-CO_2. v_b measurements were based on PET/CT blood volume agents whenever possible. Parameter values reported for healthy subjects were preferred over measurements made within healthy tissues from patient populations.

For assessment of test-retest reproducibility within group 1, correlation analysis was

performed. The correlation between visits was assessed with Pearson's *r*. A one-sample Kolmogorov-Smirnov (KS) test was used to test for normality. After testing for normality, Bland-Altman plots were generated with limits of agreement of 1.96 times the standard deviation. A significance level of 0.05 was used for assessments of test-retest reproducibility. Intra-subject regional comparisons of parameter estimates for groups 2 and 3 were made between dynamic acquisitions and between opposing limbs, respectively. In group 2, percent change of K_1, v_b, and delay was determined relative to baseline. Thus, for the paired baseline-CPT studies, percent change of K_1 for each tissue was: 100 % * ($K_{1,CPT} - K_{1,\text{baseline}}$) / $K_{1,\text{baseline}}$. For the PAD patient in group 3, whose popliteal stenosis was behind the left knee, percent change of K_1 comparing left and right calf muscles was: 100 % * ($K_{1,LCalf} - K_{1,RCalf}$) / $K_{1,RCalf}$.

4.3. Sensitivity and identifiability analysis

Sensitivity and identifiability analysis was performed to assess the relationship between parameter estimates and various factors that may impact the estimated parameter values. Sensitivity analysis and investigation of AT was performed, such that AT could be fixed for further investigation of parameter identifiability.

4.3.1. Sensitivity curves and acquisition time (AT)

To better understand the relationships between the estimated parameters v_b, K_1, and k_2, sensitivity and identifiability analysis was performed for each tissue type. Sensitivity is a measure of how much a small error in a parameter estimate perturbs the resulting model output C_{fit}. The normalized sensitivity of parameter k_i was calculated as follows:

$$Sens_{k_i}(t) = \frac{\partial C_{fit}(t)}{\partial k_i} \frac{k_i}{C_{fit}(t)} \tag{4.4}$$

where ∂k_i was set to 5% (Mankoff et al., 1998; Muzi et al., 2005; Wells et al., 2002; Zuo et al., 2019). For each of the tissue regions, IDIFs from a representative baseline study were used as the

plasma input, and the average kinetic parameters for the eight baseline 30m29 studies from groups 1 and 2 were used to generate C_{fit}. If a small change ∂k_i leads to a large impact on the error of the model output $\partial C_{fit}(t)$ at a given time *t*, the magnitude of $Sens_{k_i}$ will be larger, and therefore it is more likely that the parameter k_i can be estimated accurately during the fitting process. This allows for a visual assessment of the ATs that lead to a higher confidence in the parameter estimates.

As shown in figure 4.3, sensitivity plots for the first 4.5 minutes of the acquisitions were generated across the different regions. Sensitivity curves show that blood volume fraction v_b was challenging to estimate, in that only the first 30-60 seconds of most tissue TACs are sensitive to changes in v_b. As AT increased, K_1 became easier to estimate reliably for most tissues, as reflected by the plateauing of the K_1 sensitivity curves close to a value of 1 by approximately 60 seconds. In contrast to K_1, estimation of k_2 was challenging in most tissues, since most tissues did not reflect a high sensitivity to changes in k_2 until relatively late in the acquisition (> 3 minutes), if at all. However, for some tissues, such as the myocardium, spleen, and thyroid, the normalized sensitivity curve for k_2 approached -1 over time. Other tissues showed a peak absolute sensitivity for k_2; for the kidney, this reflects an optimal AT of approximately 90 seconds. The lung was the most challenging to fit, as it was evident from the sensitivity curve for K_1, which dropped to a value of approximately 0.25 as AT increased.

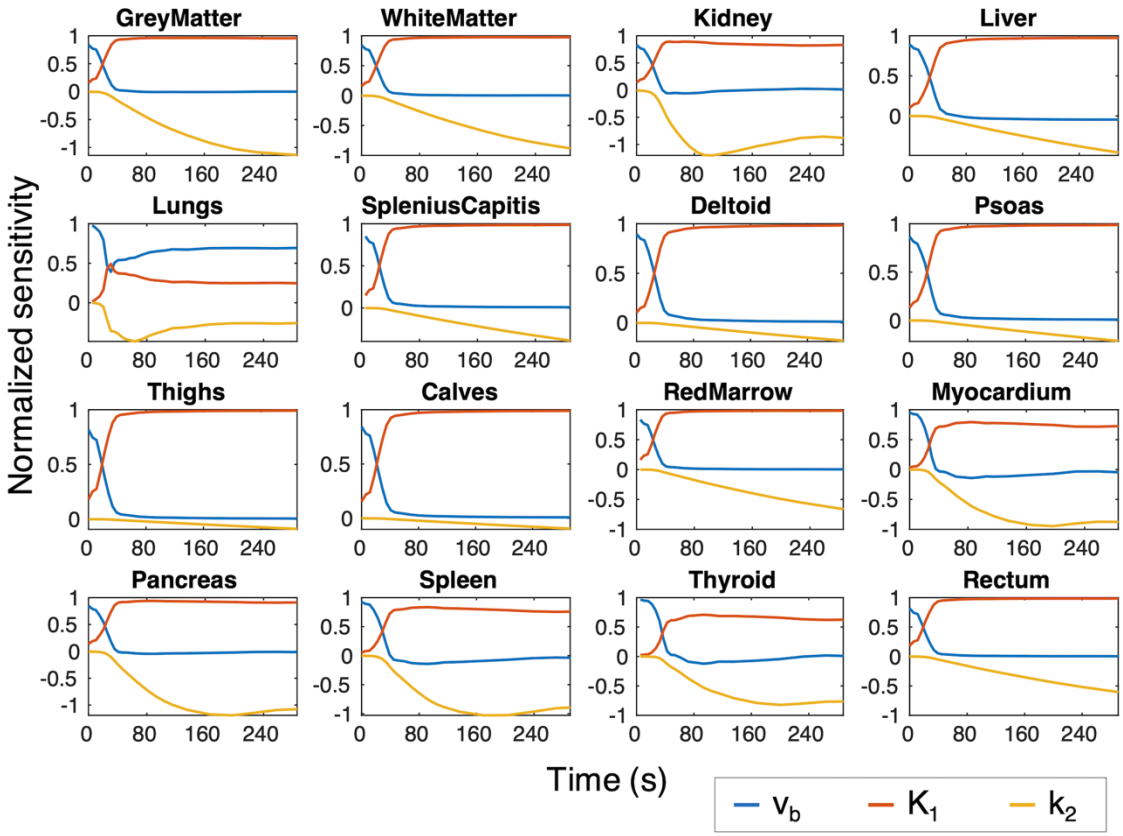

Figure 4.3: Normalized sensitivity curves

Figure 4.3: Normalized sensitivity curves for a baseline acquisition across different regions. The x-axis represents acquisition time (AT) over 5 minutes, where delay has been accounted for (e.g., time zero for grey matter does not represent time zero of the dynamic acquisition, but instead is equal to the start of the TAC used in the fitting process). v_b showed peak sensitivity in the first 30-60 seconds of most tissue TACs. K_1 can be reliably estimated in most tissues after approximately 60 seconds, as evidenced by the fact that the K_1 sensitivity curves approach 1 by 60 seconds for most tissues. k_2 was challenging to estimate, especially for short AT in the skeletal muscle. k_2 in some tissues, such as the kidney, show a peak in absolute sensitivity at certain timepoints, followed by a drop-off in magnitude towards zero.

4.3.2. Impact of acquisition time (AT) on parameter estimates

The sensitivity plots above provided useful information with regards to optimal AT. For example, the sensitivity plot for kidney showed that the magnitude of the normalized sensitivity of k_2 was maximized at 90 seconds, indicating this may be an appropriate AT for the kidney. But to further assess the impact of AT, the direct impact of AT on the parameter estimates was investigated. A series of 8 different ATs were assessed in increments of 30 seconds, from 1 to 4.5 minutes. Figure 4.4 shows the stability of estimates of K_1 and v_b across ATs. The kidney showed an inverse relationship between K_1 and v_b across ATs: K_1 decreased and v_b increased with AT. The liver estimates were unstable at short ATs, which agreed with the sensitivity curves in figure 4.3, where K_1 and v_b showed stable results with increasing AT. Estimates of k_2 also mirror the sensitivity curves, where k_2 was overestimated at short AT, especially for muscle TACs. While k_2 stabilized overall as AT increased, it nonetheless decreased in magnitude over time for most tissues, demonstrating a dependence on AT. The lung was a notable exception, which showed a wide range of values for k_2 across subjects (e.g., for an AT of 60 seconds, k_2 ranged from 0.7 to 7.2 min^{-1}) but was relatively flat across AT. Based on figures 4.3 and 4.4, optimal ATs were identified and fixed for each region for further analyses. For tissues that showed stability across ATs, 180 seconds was selected as the default AT. All subsequent fitting was performed with the issue-specific ATs listed in table 4.5.

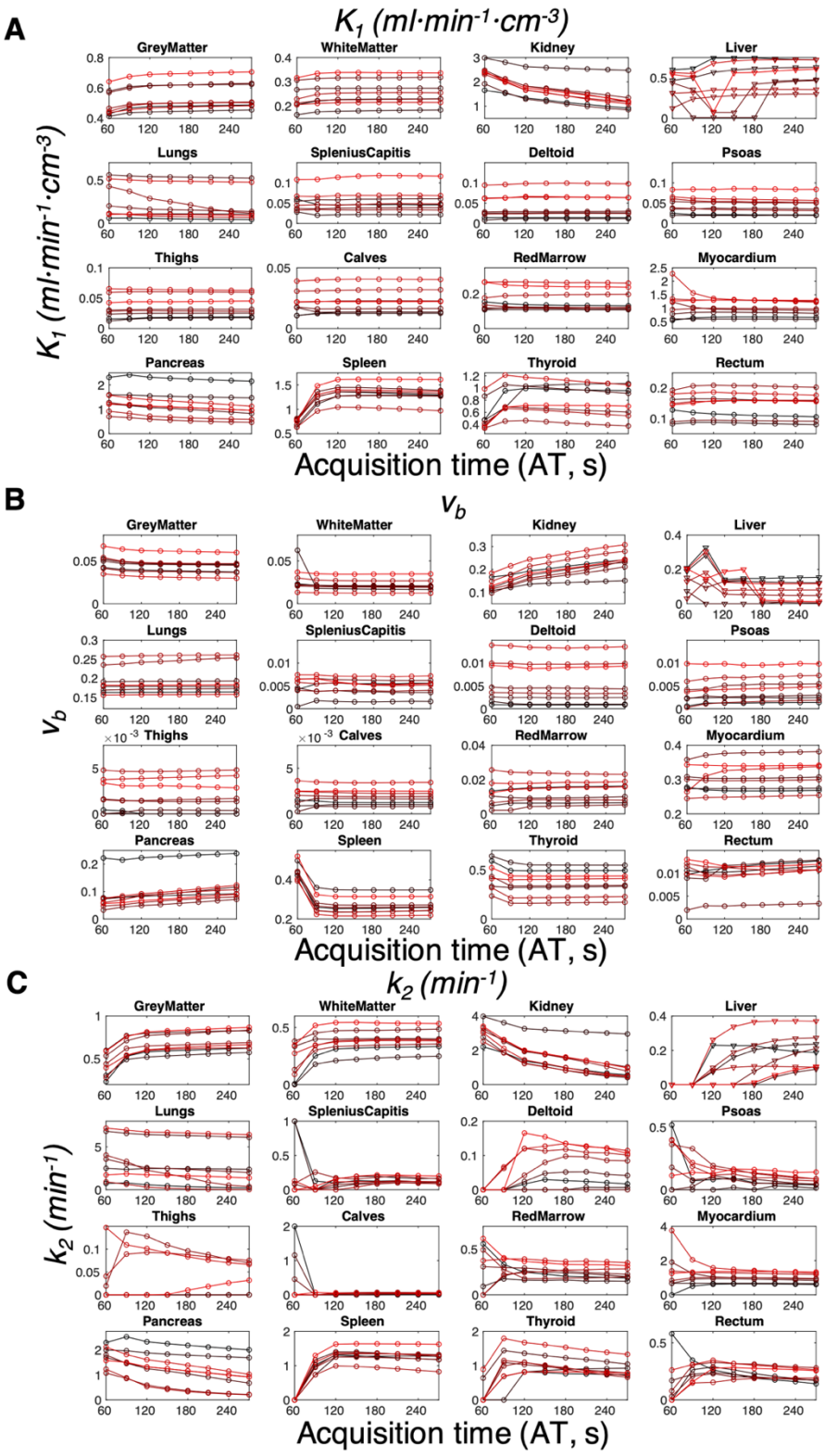

Figure 4.4: Impact of AT on parameter estimates

Figure 4.4: Impact of AT on parameter estimates. Different subjects are shown across a gradient of red to black lines. After assessing sensitivity changes over the first 4.5 minutes, the impact of the AT was directly assessed by performing the fitting TACs across ATs of 60 to 270 seconds, in 30 second increments. For most tissues, K_1 (A) and v_b (B) were stable across ATs. Notable exceptions were the kidney, where K_1 and v_b are inversely related across ATs, and the liver, where the fitting process resulted unstable estimates for shorter ATs. The grey matter, pancreas, and rectum estimates also showed slightly decreasing values for K_1 and increasing v_b with larger ATs. The spleen and thyroid also show an inverse relationship between changes in K_1 and v_b with AT, but only for the shortest ATs. In (C), estimates of k_2 fluctuate at shorter ATs, but show stabilization at longer ATs across tissues, except for the kidney.

Table 4.4: Tissue-specific ATs

AT (s)	Tissue region
180	Grey Matter
180	White Matter
90	Kidney
240	Liver
60	Lungs
180	Splenius Capitis
240	Deltoid
240	Psoas
270	Thighs
270	Calves
180	Red Marrow
180	Myocardium
180	Pancreas
180	Spleen
180	Thyroid
180	Rectum

4.3.3. Parameter identifiability: correlation matrix

The sensitivity curves above not only allow for assessment of the proper AT for different tissues, but also give an initial indication of the identifiability of individual parameters. For parameters to be considered identifiable, the sensitivity functions must be distinct from each other over time (Muzi et al., 2005). This was assessed by calculating the correlation matrix *CM*. The sensitivity matrix *SM*, the entries of which are equal to the integrated product of pairs of sensitivity functions produced with equation 4.4 for parameters k_i and k_j, can be inverted and rescaled to produce the *CM*:

$$SM_{k_i k_j} = \int_0^T Sens_{k_i}(\tau) Sens_{k_j}(\tau) d\tau \tag{4.5}$$

$$CM = \frac{1}{\sqrt{diag(SM^{-1})}} \begin{bmatrix} SM_{k_1k_1} & SM_{k_2k_1} & SM_{k_3k_1} \\ SM_{k_1k_2} & SM_{k_2k_2} & SM_{k_3k_2} \\ SM_{k_1k_3} & SM_{k_2k_3} & SM_{k_3k_3} \end{bmatrix}^{-1}. \tag{4.6}$$

The integration time *T* was fixed at 4.5 minutes. Highly correlated parameters, which would have values close to 1 in *CM*, may be difficult to estimate independently (Mankoff et al., 1998; Muzi et al., 2005; Wells et al., 2002).

As shown in table 4.5, K_1 and k_2 were highly correlated, with correlation coefficients of greater than 0.88 in all tissues. v_b was negatively and weakly correlated with K_1 and k_2. This agrees the assessment of different ATs in figure 4.4, especially for the kidney, pancreas, and rectum, which all showed an inverse relationship between K_1 and v_b across ATs, and show a negative correlation coefficient of 0.3 or greater.

Table 4.5: Correlation matrices across tissue regions

	v_b	K_1	k_2	v_b	K_1	k_2	v_b	K_1	k_2	v_b	K_1	k_2
	Grey Matter			**White Matter**			**Kidney**			**Liver**		
v_b	1	-	-	1	-	-	1	-	-	1	-	-
K_1	-0.30	1		-0.30	1		-0.42	1		-0.22	1	-
k_2	-0.28	0.93	1	-0.27	0.91	1	-0.42	0.98	1	-0.25	0.90	1
	Lung			**Splenius Capitis**			**Deltoid**			**Psoas**		
v_b	1	-	-	1	-	-	1	-	-	1	-	-
K_1	-0.42	1		-0.30	1		-0.30	1		-0.31	1	-
k_2	0.00	0.89	1	-0.25	0.89	1	-0.24	0.90	1	-0.25	0.89	1
	Thighs			**Calves**			**Red Marrow**			**Myocardium**		
v_b	1	-	-	1	-	-	1	-	-	1	-	-
K_1	-0.31	1		-0.31	1		-0.30	1		-0.10	1	-
k_2	-0.26	0.89	1	-0.25	0.89	1	-0.25	0.90	1	-0.17	0.95	1
	Pancreas			**Spleen**			**Thyroid**			**Rectum**		
v_b	1	-	-	1	-	-	1	-	-	1	-	-
K_1	-0.30	1		-0.15	1		-0.11	1		-0.31	1	-
k_2	-0.32	0.96	1	-0.22	0.96	1	-0.14	0.95	1	-0.27	0.90	1

4.3.4. Parameter identifiability: error landscapes

To better visualize [^{11}C]-butanol kinetic parameter identifiability initially explored via the correlation matrix above, error landscapes were produced, where the weighted residual sum of squares (WRSS) was determined across the parameter space. Basis functions were generated using logarithmic sampling for v_b, K_1, and k_2 with the following upper bounds: [1.0, 5.0 ml·min^{-1}·cm^{-3}, 5.0 min^{-1}] and lower bounds of zero. TACs from one baseline 30m29 dataset were used to generate the error landscapes, with a fixed, tissue-specific AT. If there is a global minimum in the error landscape, then the model output parameters are globally identifiable and can be uniquely determined. It is possible to have a local minimum, in which case the model parameters are considered locally identifiable. It is also possible to have a flat region in the error landscape where the error is relatively constant; in this case, gradient-based fitting algorithms, including the Levenberg-Marquart algorithm utilized in this work (G. Wang et al., 2021), can fail to converge in the requested number of iterations. In cases where the fitting process failed (i.e., the parameter

values hit the upper or lower bounds), the resulting WRSS was excluded from visualization in figure 4.5.

Error landscapes shown in figure 4.5 utilized the fixed ATs listed in table 4.4. Many tissues, such as grey matter and skeletal muscle regions, only showed successful fits in a small part of the parameter space, indicating the presence of a global minimum. In other tissues such as spleen and thyroid, the error landscape showed a flat region, resulting in a wider range of possible fits (corresponding to low WRSS) within the landscapes. This corresponds to the sensitivity curves in figure 4.3, where the myocardium, spleen, and thyroid showed a plateauing of the sensitivity curves for K_1 to approximately 0.7 - 0.8. The range of k_2 values in figure 4.5 also agree with the sensitivity plots. The value of k_2 was demonstrated to be less impactful in obtaining a reasonable fitting result of the TAC across most tissue types in the sensitivity plots of figure 4.3, and in figure 4.5, there are broad range of values for k_2 that result in a low WRSS as reflected by the dark blue regions. The lung was the most challenging to fit; based on the sensitivity curve for lung in figure 4.3, a higher temporal resolution (e.g., 2-second framing) may improve the fitting results. Together the sensitivity curves, correlation matrix, and the error landscapes show that for some tissues, a range of possible output solutions exist, and that less confidence can be placed in the resulting parameter estimates for myocardium, spleen, and thyroid, relative to results for tissues like grey matter, pancreas, and liver.

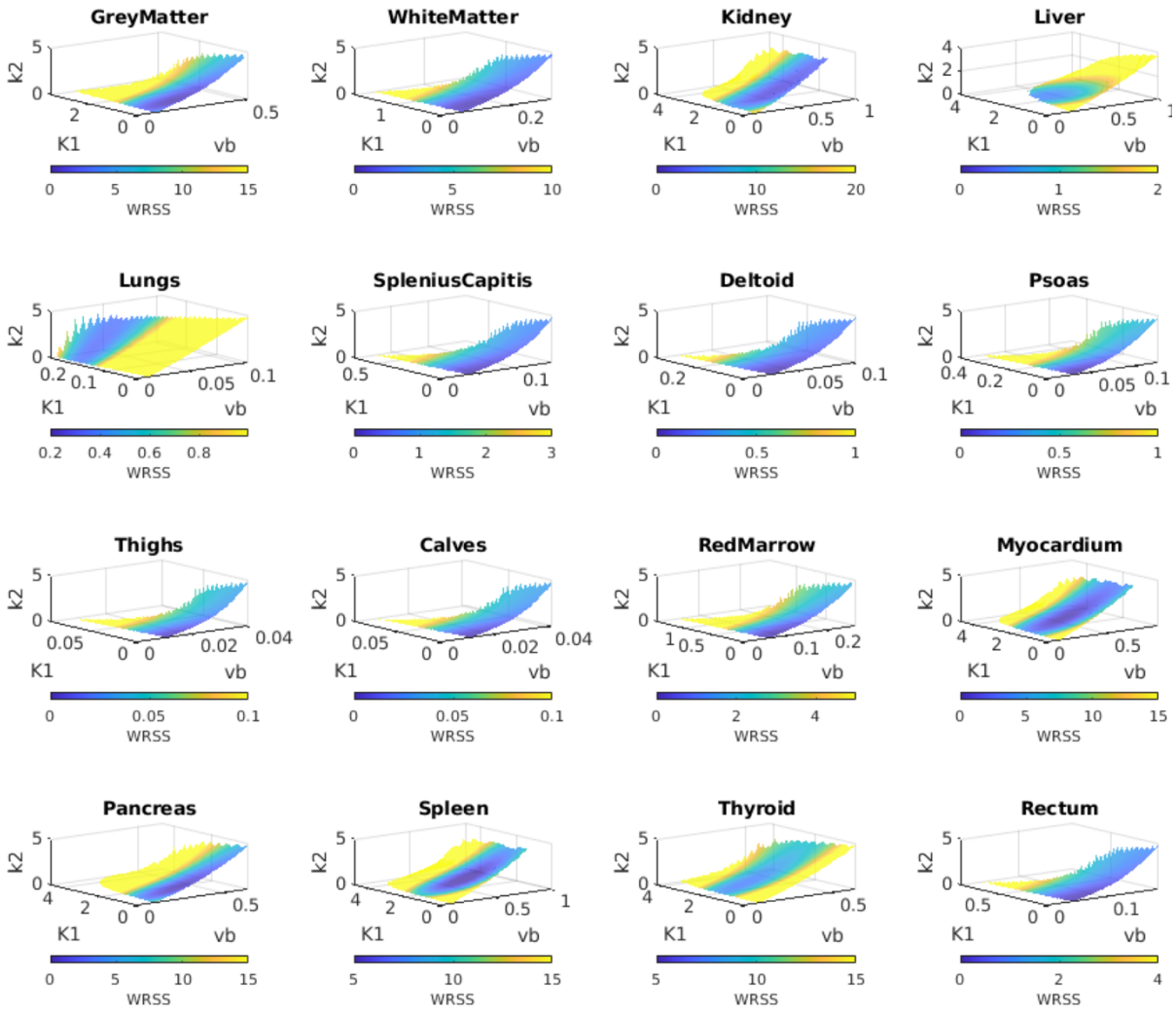

Figure 4.5: Error landscapes across all tissues

Figure 4.5: Error landscapes across all tissues. Error landscapes were generated using 30m29 framing, 4.0x4.0x4.0 mm^3 voxels, and tissue-specific ATs. The weighted residual sum of squares (WRSS) was used as the colormap, where dark blue represents the minimum error for the corresponding values of v_b, K_1 and k_2 that are plotted along the x, y, and z axes respectively. For many tissues, the model failed to fit k_2 and hit the lower bound of 0.0 or the upper bound of 5.0 when values of K_1 and v_b were far from the minimum WRSS; these data were excluded from the error landscapes. Some tissues show broad minima, such as the lungs and thyroid.

4.3.5. Parameter identifiability: Monte Carlo simulation

The previous two sections address parameter identifiability through measuring or visualizing the impact of different parameter values on the fitting error. Practical identifiability of the model (i.e., the impact of noisy TACs on the parameter estimates) was assessed through Monte Carlo simulations (Mankoff et al., 1998; Muzi et al., 2005; Wells et al., 2002; Zuo et al., 2019). As discussed above, initial sensitivity and identifiability results were used to determine the appropriate AT, which was fixed for each tissue (table 4.4) prior to the Monte Carlo simulation. For each tissue type and fixed AT, the average parameter set for v_b, K_1, and k_2 was determined across the eight healthy control baseline datasets reconstructed with the 30m29 dynamic framing scheme and a voxel size of 4.0x4.0x4.0 mm^3. IDIFs from each of the eight baseline studies were used to generate 1,000 noisy realizations per baseline acquisition. Delay was not implemented in the Monte Carlo simulations, since it was pre-determined via the leading-edge method (E. J. Li et al., 2021). Any IDIF-specific corrections (i.e., delay, dispersion) were performed for each baseline study prior to generating the clean TAC, denoted $\bar{C}$. For a post-delay frame m at time t_m, Gaussian-distributed noise (Wu & Carson, 2002) was added:

$$C(\mathrm{t}_m) \sim Gaussian(\bar{C}(\mathrm{t}_m), S_c\delta_m), \quad \delta_m = \sqrt{\frac{\bar{C}(\mathrm{t}_m)\cdot\exp(\lambda t_m)}{\Delta t_m}} \tag{4.7}$$

where S_c is a tissue-specific scaling factor for the standard deviation. The unscaled standard deviation, δ_m, scales with the radioisotope decay constant λ and the frame length Δt_m. To account for scatter and spillover prior to the bolus arrival to the tissue, equation 4.7 was modified (E. J. Li et al., 2021) to give δ_m a non-zero value for the tissue concentration $\bar{C}(\mathrm{t}_m)$:

$$C(\mathrm{t}_m) \sim Gaussian(\bar{C}(\mathrm{t}_m), S_c\delta_m), \quad \delta_m = \sqrt{\frac{0.01*\max(\overline{C_T})\cdot\exp(\lambda t_m)}{\Delta t_m}} \tag{4.8}$$

where $\max(\overline{C_T})$ is the maximum value of $\bar{C}$ in the first 0 to T seconds of delay-adjusted

acquisition. T is tissue-dependent, since the upslope of $\bar{C}$ depends on the shape of the IDIF and the parameter values. S_c was also set for each tissue type through visual assessment of the noisy realizations. The resulting 8,000 Monte Carlo simulation parameter estimates were averaged, and their standard deviation was estimated for comparison with the ground truth parameters.

The tissue-specific scaling factors for the standard deviation S_c and average simulation parameter estimates used in the simulation as ground truth are listed in table 4.6, along with simulation-based mean and standard deviation. Simulated-based estimates were in agreement with ground truth parameters, though some values (e.g., v_b and k_2 of the liver) were greatly over- or underestimated in the simulations, indicating more sensitivity to noise in these tissue-parameter pairs.

Table 4.6: Practical identifiability: ground truth and average (s.d.) simulation estimates

	Ground truth	Average	(s.d.)	Ground truth	Average	(s.d.)	Ground truth	Average	(s.d.)	Ground truth	Average	(s.d.)
	Grey Matter, S_c = 0.8			*White Matter, S_c = 0.6*			*Kidney, S_c = 1.0*			*Liver, S_c = 0.3*		
v_b	0.062	0.062	(0.011)	0.029	0.029	(0.007)	0.157	0.157	(0.031)	0.068	0.318	(0.153)
K_1	0.528	0.528	(0.085)	0.250	0.250	(0.050)	2.020	2.020	(0.393)	0.532	0.501	(0.567)
k_2	0.667	0.667	(0.107)	0.374	0.374	(0.090)	2.382	2.382	(0.600)	0.189	0.081	(0.153)
	Lungs, S_c = 0.5			*Splenius Capitis, S_c = 0.15*			*Deltoid, S_c = 0.15*			*Psoas, S_c = 0.15*		
v_b	0.191	0.185	(0.030)	0.005	0.005	(0.002)	0.006	0.006	(0.005)	0.004	0.004	(0.003)
K_1	0.261	0.251	(0.192)	0.054	0.054	(0.030)	0.042	0.042	(0.031)	0.044	0.044	(0.021)
k_2	3.441	3.476	(2.492)	0.140	0.140	(0.051)	0.063	0.064	(0.051)	0.073	0.073	(0.038)
	Thighs, S_c = 0.3			*Calves, S_c = 0.3*			*Red Marrow, S_c = 0.2*			*Myocardium, S_c = 0.5*		
v_b	0.002	0.002	(0.002)	0.002	0.002	(0.001)	0.018	0.018	(0.008)	0.306	0.305	(0.043)
K_1	0.036	0.036	(0.018)	0.022	0.022	(0.010)	0.159	0.159	(0.061)	0.994	0.996	(0.280)
k_2	0.030	0.031	(0.034)	0.034	0.035	(0.023)	0.240	0.241	(0.070)	1.034	1.036	(0.296)
	Pancreas, S_c = 1.5			*Spleen, S_c = 1.5*			*Thyroid, S_c = 0.5*			*Rectum, S_c = 0.3*		
v_b	0.149	0.149	(0.069)	0.267	0.267	(0.043)	0.368	0.368	(0.131)	0.010	0.010	(0.003)
K_1	1.074	1.075	(0.461)	1.341	1.341	(0.167)	0.816	0.816	(0.252)	0.144	0.144	(0.044)
k_2	1.062	1.064	(0.565)	1.305	1.305	(0.192)	0.997	0.998	(0.257)	0.238	0.238	(0.052)

Since the sensitivity and identifiability analyses of skeletal muscle ROIs (splenius capitis, deltoid, psoas, thighs, and calves) showed similar parameter estimates in baseline studies, these regions were fit separately, but were pooled for discussion of the results in the subsequent sections.

4.4. Reconstruction parameters: impact on parameter estimates

In addition to the sensitivity and identifiability analyses detailed above, a variety of reconstruction protocols (table 4.2) were performed in three representative baseline acquisitions to investigate the impact of framing and voxel size on ROI-based parameter estimates. Images were reconstructed with a number of reconstruction protocols to achieve high temporal resolution over the first pass of the bolus. One-second temporal resolution was achieved with a 2m90 framing scheme (table 4.2). To obtain ATs greater than 90 seconds, the 2m90 data were concatenated with the 2 to 5-minute period of the 5m52 images. Additional reconstructions utilized for assessing the impact of temporal resolution were 5m52 (2 second resolution), 30m29 (5 second resolution), and 5m12 (10 second resolution). Estimated values were compared to previously published works in table 4.7.

Table 4.7: Parameter values adapted from previous work for comparison

Tissue type	v_b	v_b *tracer*	v_b **ref.**	K_1	K_1 *tracer*	K_1 *ref.*	k_2	k_2 **ref.**
Grey matter	0.05	[^{11}C]-CO	(Leenders et al., 1990)	0.53-0.83	[^{11}C]-butanol; [^{15}O]-butanol; [^{15}O]-H_2O	(Berridge et al., 1991; Herzog et al., 1996; Ito et al., 2001)	0.78*	(Gjedde et al., 1980)
White matter	0.03	[^{11}C]-CO	(Leenders et al., 1990)	0.25	[^{11}C]-butanol	(Quarles et al., 1993)	0.32*	(Gjedde et al., 1980)
Kidney	0.15	[^{15}O]-CO	(Yamashita et al., 1989)	3.3	[^{15}O]-H_2O	(Alpert et al., 2002)	-	
Liver	0.2	[^{15}O]-H_2O	(Taniguchi et al., 1996)	1.25	[^{15}O]-H_2O	(Taniguchi et al., 1999)	-	
Lung	0.16-0.21	[^{11}C]-CO; [^{11}C]-CO; [^{15}O]-H_2O	(Brudin et al., 1987; Schober et al., 1985; Schuster et al., 1995)	1.20-1.40	[^{15}O]-H_2O; [^{15}O]-H_2O	(Matsunaga et al., 2017; Schuster et al., 1995)	-	
Bone marrow	0.02-0.03	[^{15}O]-CO; DCE-MRI†	(S. Iida et al., 1999; Liu et al., 2021)	0.10-0.18	[^{15}O]-H_2O; [^{15}O]-CO_2	(Kahn et al., 1994; Martiat et al., 1987)	-	
Skeletal muscle	0.003	[^{15}O]-CO	(Raitakari et al., 1995)	0.18-0.24	[^{15}O]-H_2O; [^{15}O]-H_2O	(Burchert et al., 1997; Nuutila et al., 1996)	-	
Myocardium	0.31	[^{15}O]-CO	(H. Iida et al., 1991)	0.94	[^{15}O]-H_2O	(Kaufmann et al., 1999)	-	
Pancreas	0.16	Perfusion CT	(Delrue et al., 2012)	1.14	[^{15}O]-H_2O	(Komar et al., 2009)	-	
Spleen	0.17-0.20	[^{18}F]-FEOBV; perfusion CT	(Horsager et al., 2022; Yan et al., 2022)	1.33-1.68	[^{15}O]-H_2O; [^{15}O]-H_2O	(Oguro et al., 1993; Taniguchi et al., 1999)	-	
Thyroid	0.14	Perfusion CT	(Rumboldt et al., 2005)	0.6	[^{15}O]-H_2O	(Fletcher et al., 2015)	-	
Rectum	0.034	Perfusion CT	(Sahani et al., 2005)	0.16	Perfusion CT	(Khan et al., 2012)	-	

Units for K_1 and k_2 are $ml \cdot min^{-1} \cdot cm^{-3}$ and min^{-1} respectively. * Calculated based on the partition coefficient ρ, where $\rho = K_1/k_2$. † Dynamic contrast-enhanced magnetic resonance imaging.

The estimated parameter values across framing protocols and voxel sizes are shown in figure 4.6. Voxel size was inconsequential for most tissues, but reconstructions with 2.344 mm voxels resulted in higher estimates for K_1 and delay in the thyroid compared to 4.0 mm reconstructions. Temporal resolution did not impact perfusion estimates in the brain, skeletal muscle, pancreas or marrow, but resulted in decreased K_1 with increasing frame length for the myocardium, thyroid, and spleen, while the liver showed increasing perfusion estimates with frame length. Delay estimates increased with frame duration particularly in the liver, where the slow rising edge of the liver TAC results in overestimation of delay, as observed previously (E. J. Li et al., 2021). Bone marrow, spleen, and thyroid also showed moderate (5-10s) changes in delay as frame length increases. Blood volume v_b was larger with increasing frame lengths, especially in the myocardium, thyroid, and spleen. The fitting process failed for the lungs; with short frames, v_b was small or equal to zero, and with long frames, K_1 was underestimated. In the pancreas, there was a shift in the estimation of delay with shorter (1-2 second) frames, and v_b was close to or equal to zero. Since better overall agreement with the values of K_1 and v_b in table 4.7 were achieved with 2 and 5-second frames, the impact of model choice was investigated with the 5m52 and 30m29 datasets with tissue-optimized ATs.

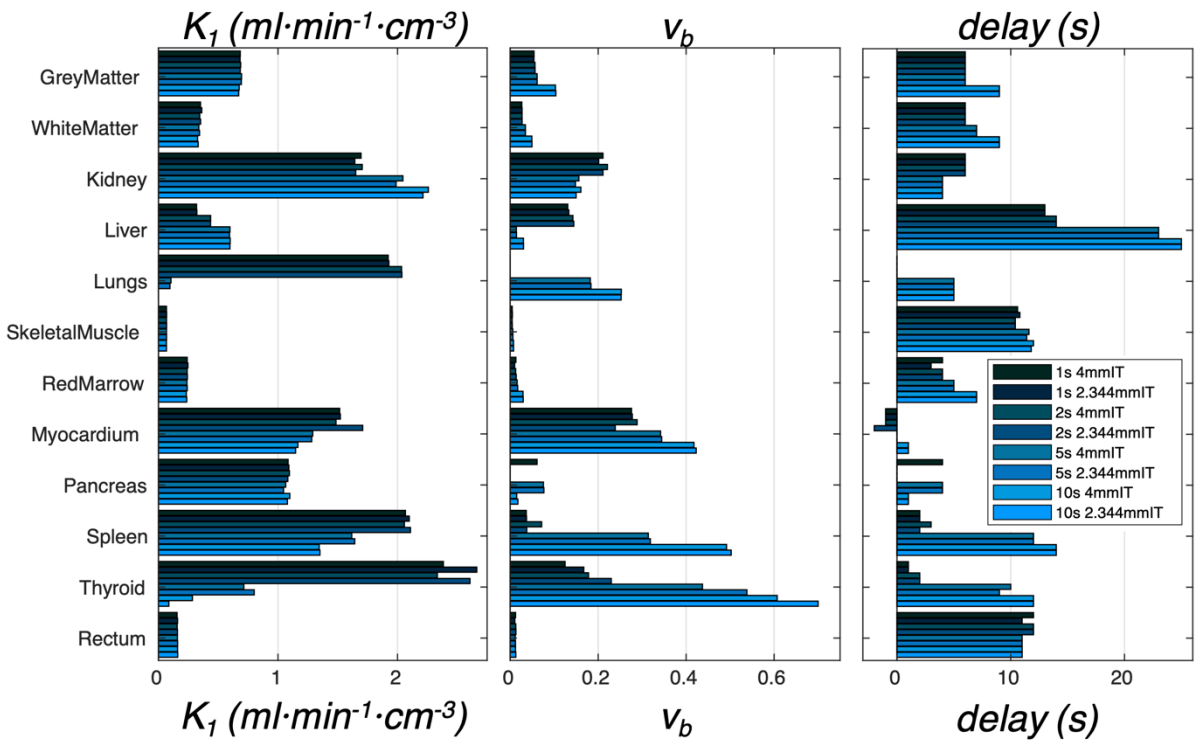

Figure 4.6: Impact of reconstruction parameters on ROI-based parameter estimates

Figure 4.6: Impact of reconstruction parameters on ROI-based parameter estimates. Average parameter estimates were determined across the different framing schemes and voxel sizes. Voxel size had less of an impact on parameter estimates than frame length, as evidenced by the higher K_1 and lower v_b in a number of tissues (e.g., myocardium, spleen, thyroid) with short (1-2s) frames. The kidney showed a unique relationship with framing, where K_1 increased and lower v_b decreased with frame length. The fitting process in the lungs and the pancreas resulted in underestimation of v_b with shorter frames. Delay estimates in the liver, spleen, and thyroid were highly dependent on the temporal framing.

4.5. Model impact on parameter estimates and AIC

After fixing AT, further investigation of the impact of the temporal resolution was performed. The three models implemented in this work (1T4P, 1T5P, and 1T6P) were tested across 2 and 5-second

reconstructed baseline datasets. As shown in figure 4.7, with a temporal resolution of 2 seconds, increased model complexity did not greatly improve AIC (where the most negative value indicates the superior model). As compared to the 1T4P model, AIC increased in most tissues with the 1T5P and 1T6P models. This was particularly evident for the kidney, myocardium, pancreas, spleen, and thyroid, where K_1 and v_b were also overestimated. In tissues where the AIC was very similar across models (grey matter, white matter, skeletal muscle, red marrow, and rectum), there was little impact on K_1 but the 1T6P model resulted in the overestimation of v_b in some tissues compared to literature values in table 4.7. The liver showed the greatest gain in model fit and resulted in parameter values that were closer to the values listed in table 4.7.

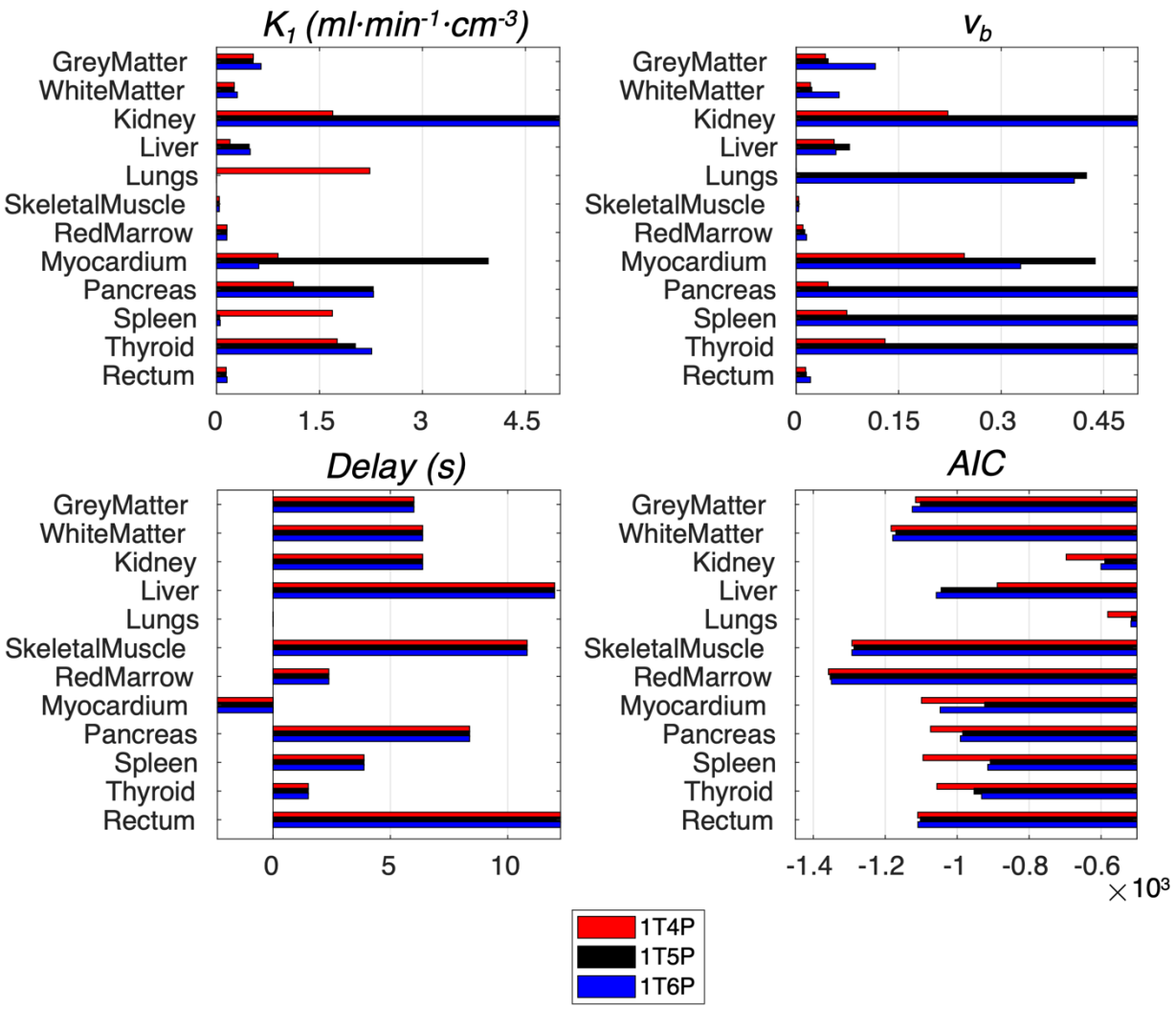

Figure 4.7: Impact of model choice on parameter estimates for 5m52 framing protocol

Figure 4.7: Impact of model choice on parameter estimates for 5m52 (2-second temporal resolution) framing protocol. The increased model complexity of the 1T5P and 1T6P models did not result in improved parameter estimates for the majority of tissues. Further, the 1T5P and 1T6P models overestimated values for v_b and K_1 in a number of tissues relative to literature values in table 4.7, including the kidneys and lungs. The 1T6P model was beneficial for fitting the liver TACs, where the 1T4P and 1T5P models showed underestimation of K_1 relative to literature value of 1.25 ml·min^{-1}·cm^{-3} (Taniguchi et al., 1996) from table 4.7.

Similar results were obtained with 5-second framing from the 30m29 datasets, where AIC favored the 1T4P model in all tissues except for the liver (figure 4.8). Based on these results and those from section 4.4 in which reconstruction parameters were investigated, an initial temporal resolution of 5 seconds, derived from the 30m29 protocol, was chosen for subsequent analyses.

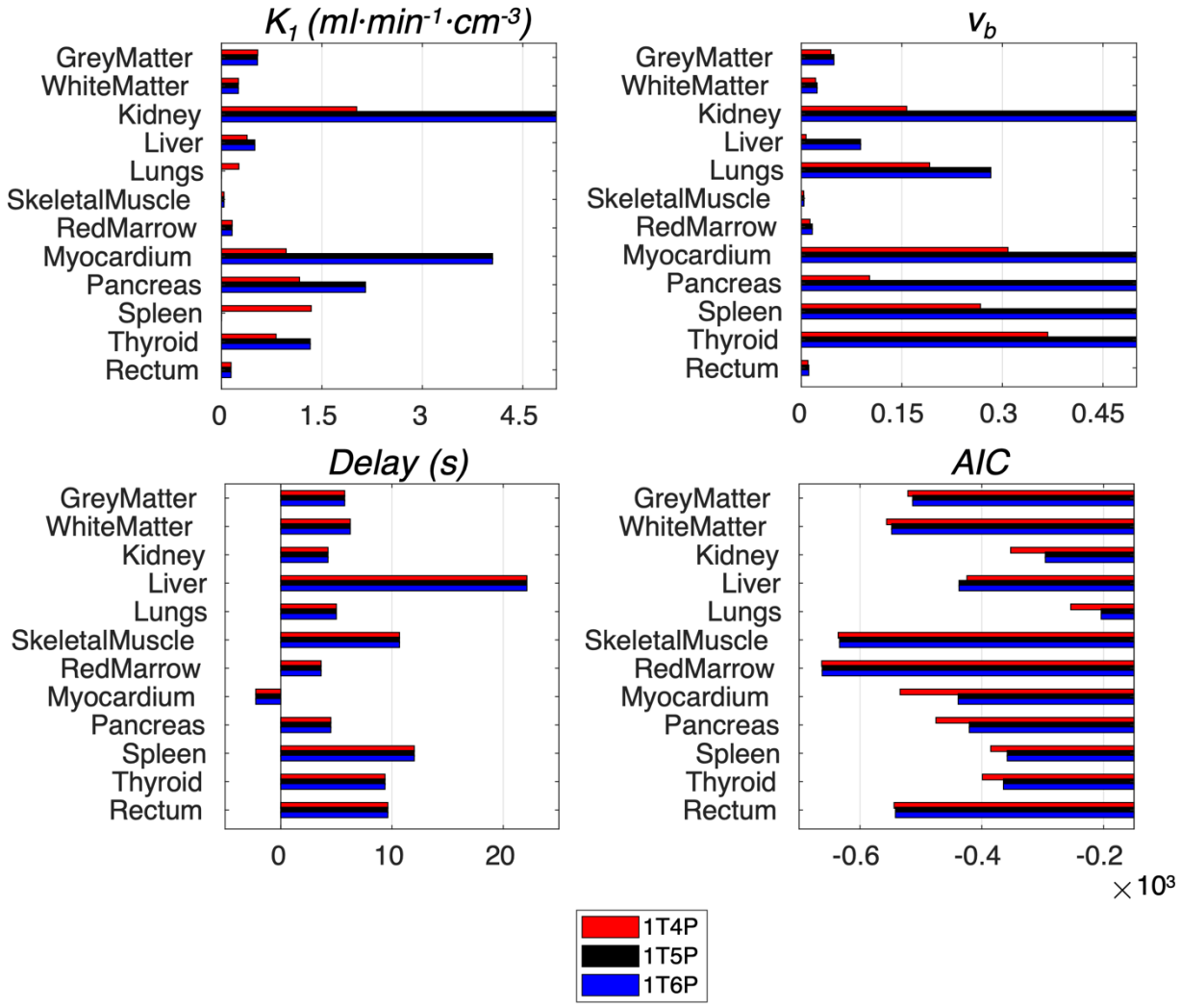

Figure 4.8: Impact of model choice on parameter estimates for 30m29 framing protocol

Figure 4.8: Impact of model choice on parameter estimates for 30m29 (5-second temporal resolution) framing protocol. The 1T4P model was the preferred model for all tissues except the liver. The 1T4P model resulted in underestimation of K_1 for the liver relative to the other models, while for other tissues, higher-complexity models resulted in failed estimates of K_1 in the lungs

and spleen, and over estimation of v_b for the myocardium, pancreas, spleen, and thyroid as compared to literature values in table 4.7. Based on the AIC and parameter estimates depicted here for 5-s frames, the 1T4P model was used for further analyses, except for in the liver, where the 1T6P model was used.

4.6. Baseline parameter estimates and test-retest reproducibility

After performing sensitivity and identifiability analyses and investigating the impact of reconstruction parameters and model selection, the optimal AT, reconstruction parameters, and model for each tissue, were fixed. Baseline parameter estimates were determined using the 30m29 framing protocol with 5-second temporal resolution and 4.0x4.0x4.0 mm^3 voxels (table 4.8). All tissues except for the liver were fit with a 1T4P model, while the liver was fit with the 1T6P model.

Kidney, liver, and lung regions showed underestimation of perfusion (K_1) compared to published work in table 4.7, while thyroid showed an overestimation of K_1 (0.8 in this work versus 0.6 $ml \cdot min^{-1} \cdot cm^{-3}$ by Fletcher et al. (2015)). Liver v_b was also 66% lower than reported (Taniguchi et al., 1996), and thyroid v_b was approximately double the value reported previously (Rumboldt et al., 2005). The wide range of estimated parameter values across the body are shown in figure 4.9.

Table 4.8: Parameter estimates in [^{11}C]-butanol baseline scans (N = 8)								
Parameter	**Grey Matter**		**White Matter**		**Kidney**		**Liver**	
v_b	0.044	(0.009)	0.021	(0.007)	0.157	(0.032)	0.068	(0.058)
K_1 (ml·min^{-1}·cm^{-3})	0.543	(0.089)	0.255	(0.052)	2.02	(0.393)	0.532	(0.162)
k_2 (min^{-1})	0.690	(0.111)	0.387	(0.093)	2.382	(0.601)	0.189	(0.102)
delay (s)	5.75	(0.71)	6.25	(1.17)	4.25	(0.71)	22.13	(0.83)
AT (s)	180	-	180	-	90	-	240	-
LE threshold (%)	5.0	-	5.0	-	1.0	-	15.0	-
Parameter	**Lungs**		**Skeletal Muscle**		**Red Marrow**		**Myocardium**	
v_b	0.191	(0.036)	0.004	(0.002)	0.013	(0.006)	0.306	(0.043)
K_1 (ml·min^{-1}·cm^{-3})	0.261	(0.204)	0.040	(0.012)	0.161	(0.062)	0.994	(0.280)
k_2 (min^{-1})	3.441	(2.486)	0.068	(0.044)	0.239	(0.071)	1.034	(0.297)
delay (s)	5.00	(0.00)	10.68	(5.18)	3.63	(1.41)	-2.25	(1.03)
AT (s)	60	-	240	-	180	-	180	-
LE threshold (%)	1.0	-	6.2*	-	3.0	-	1.5	-
Parameter	**Pancreas**		**Spleen**		**Thyroid**		**Rectum**	
v_b	0.102	(0.054)	0.267	(0.043)	0.368	(0.131)	0.01	(0.003)
K_1 (ml·min^{-1}·cm^{-3})	1.167	(0.539)	1.341	(0.167)	0.816	(0.251)	0.144	(0.044)
k_2 (min^{-1})	1.183	(0.636)	1.305	(0.191)	0.997	(0.257)	0.238	(0.052)
delay (s)	4.50	(0.76)	12.00	(0.93)	9.38	(1.30)	9.63	(1.51)
AT (s)	180	-	180	-	180	-	180	-
LE threshold (%)	2.0	-	25.0	-	20.0	-	1.5	-

*Average value across pooled muscle groups

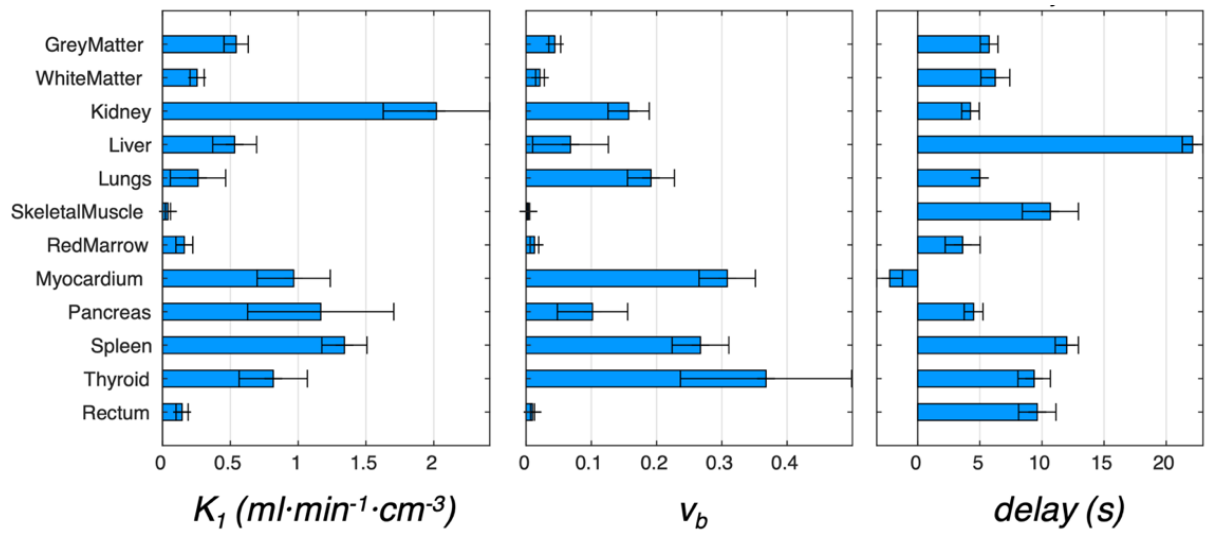

Figure 4.9: Baseline ROI-based kinetic parameter estimates across the body

Figure 4.9: Baseline ROI-based kinetic parameter estimates across the body. TACs were generated using the 30m29 framing protocol and 4.0x4.0x4.0 mm^3 voxels, with 5-second framing in the first 60 seconds. AT was fixed for individual tissues (table 4.4). Estimates were broadly consistent with the literature values included in table 4.7.

Correlation analysis of the three test-retest subjects (group 1) showed good agreement of K_1 (slope 0.99, $r = 0.91$, $p < 0.001$), v_b (slope 1.04, $r = 0.96$, $p < 0.001$), and delay (slope 1.03, $r = 0.97$, $p < 0.001$) across all tissue types (figure 4.10), where the muscle regions were represented as individual data points. K_1 outliers were from the kidney and pancreas for subject 1. v_b for the pancreas and spleen of subject 1 were also beyond the limits of agreement. The largest shift in delay, estimated via the LE method, was 4 seconds, which was observed in the deltoid of subject 3. k_2 was less in agreement due to large variations in lung estimates, with a slope of 0.57 and a Pearson's r of 0.77 ($p < 0.001$). When the lung values were ignored, k_2 was in better agreement between visits (slope 1.04, $r = 0.90$, $p < 0.001$), with the kidneys for subjects 1 and 3 as the outliers.

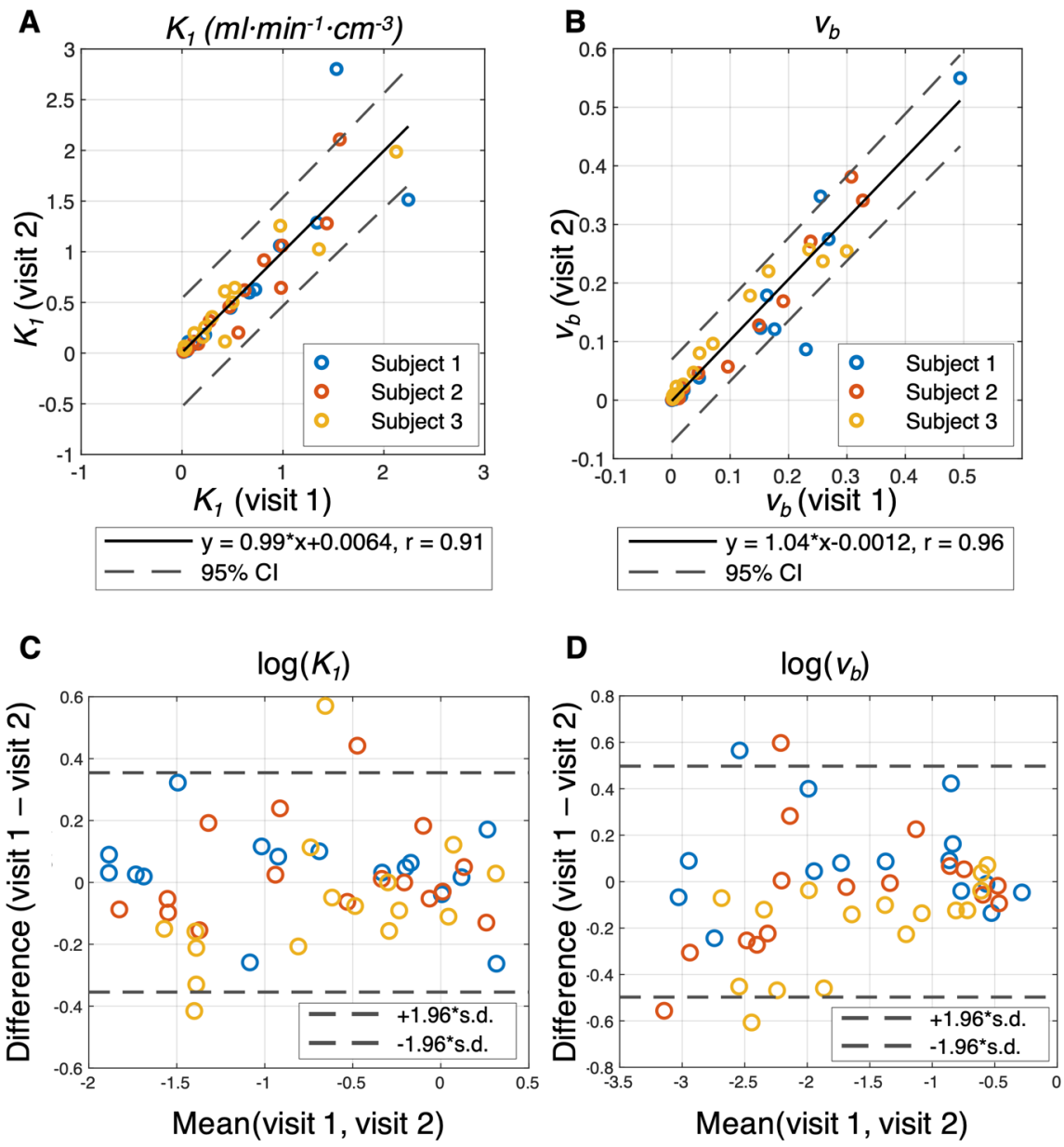

Figure 4.10: Correlation analysis of test-retest studies

Figure 4.10: Correlation analysis of test-retest studies for K_1 (A, C) and v_b (B,D). Three healthy volunteers underwent two dynamic 30-minute acquisitions no more than 2 weeks apart between visits 1 and 2. Correlation plots for K_1 (A) and v_b (B) showed strong agreement between the two visits. Normality was observed for the log-transformed data points shown in the Bland-Altman plots for K_1 (C) and v_b (D). A significance level of 0.05 was used. p values for plots (A) and (B) were less than 0.001.

4.7. Intra-subject comparisons: groups 2 and 3

As listed in table 4.1, there was a single completed group 2 study, for which a baseline study was paired with a CPT acquisition. The ROI-based results for this subject are shown in figure 4.11. CPT induced marked increases in perfusion in the myocardium and skeletal muscle (104% and 113% respectively) relative to baseline. A large decrease in the thyroid of -51% was observed. Slight increases in perfusion were observed in grey matter (22%) and the pancreas (9%), and slightly decreased perfusion was seen in the kidneys (-9%), liver (-13%), and spleen (-19%). Some tissues such as the thyroid exhibited large changes in v_b (0.41 at baseline, 0.11 with CPT), and the liver showed a decrease in blood delay of 7 seconds with the CPT.

Figure 4.11 showed an increase in the pooled skeletal muscle K_1; parameter estimates from individual muscle ROIs are shown in figure 4.12. Muscle regions showed various degrees of increased K_1. The overall range of K_1 for the CPT muscle groups was from 0.07 $ml \cdot min^{-1} \cdot cm^{-3}$ in the calves to 0.21 $ml \cdot min^{-1} \cdot cm^{-3}$ in the deltoid. For the baseline study, K_1 ranged from 0.04 $ml \cdot min^{-1} \cdot cm^{-3}$ in the calves to 0.10 $ml \cdot min^{-1} \cdot cm^{-3}$ in the deltoid. Regionally, the highest increase was in the psoas (157%), followed by the thigh muscles (137%), deltoid (117%), splenius capitis (111%), and calf muscles (75%). CPT-based delay values were smaller than baseline values; CPT-based delay was generally within 5 seconds of the baseline values, except for the calf, which exhibited a baseline delay of 16 s, and a CPT delay of 6 s.

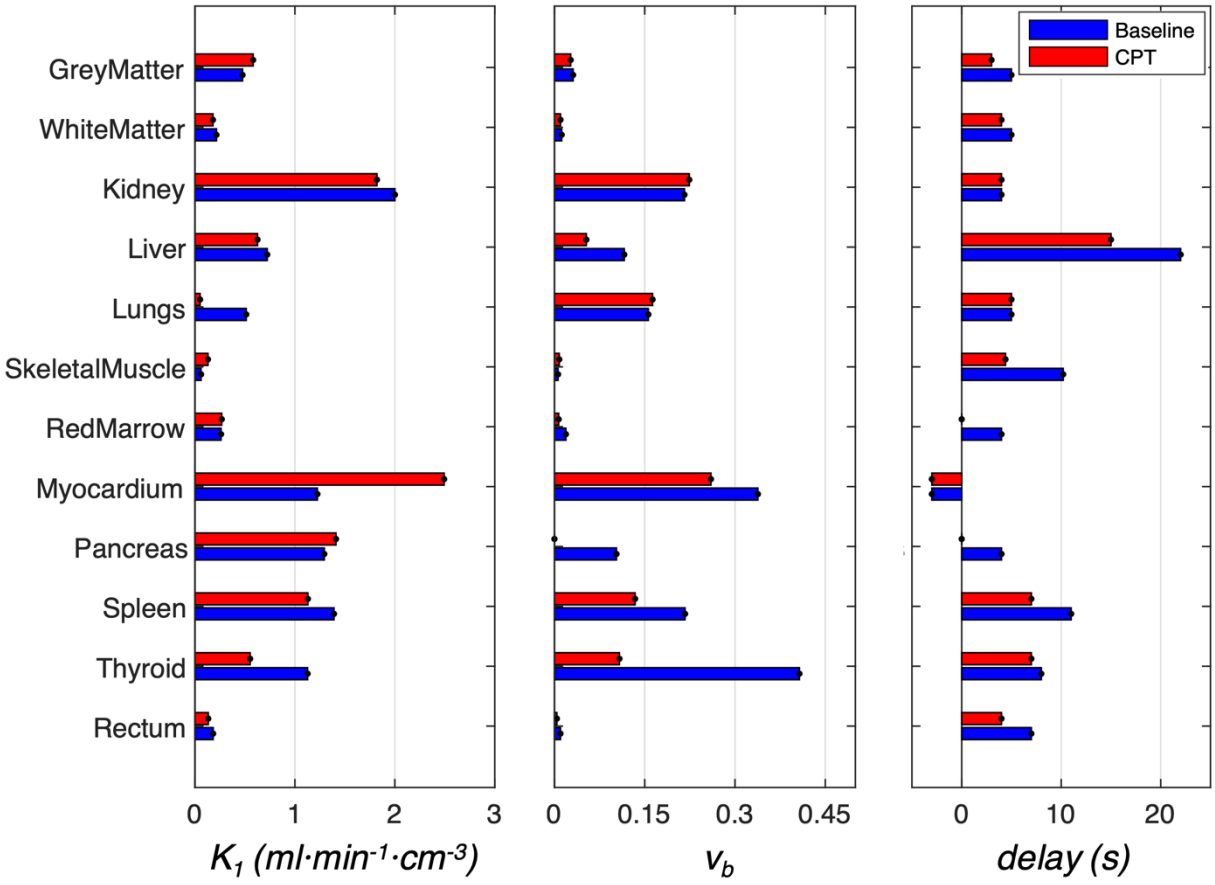

Figure 4.11: CPT intra-subject comparison

Figure 4.11: CPT intra-subject comparison between baseline (blue) and CPT (red) kinetic parameter estimates. Large increases in perfusion were observed when skeletal muscle regions were pooled (0.06 ml·min^{-1}·cm^{-3} at baseline; 0.13 ml·min^{-1}·cm^{-3} with CPT), and the myocardium (1.22 ml·min^{-1}·cm^{-3} at baseline; 2.49 ml·min^{-1}·cm^{-3} with CPT). There were also slight increases in K_1 for grey matter (0.48 ml·min^{-1}·cm^{-3} at baseline; 0.58 ml·min^{-1}·cm^{-3} with CPT) and the pancreas (1.29 ml·min^{-1}·cm^{-3} at baseline; 1.41 ml·min^{-1}·cm^{-3} with CPT). The thyroid showed a large decrease in perfusion (1.13 ml·min^{-1}·cm^{-3} at baseline; 0.55 ml·min^{-1}·cm^{-3} with CPT), and in the kidneys and spleen, perfusion was also slightly lower with the CPT. For the liver, myocardium, pancreas, spleen, and thyroid, v_b was lower for the CPT study. There were also large (>4s)

differences in delay estimates in the liver (22 s at baseline; 15 s with CPT) and skeletal muscle (average of 10.2 s at baseline; 4.4 s with CPT).

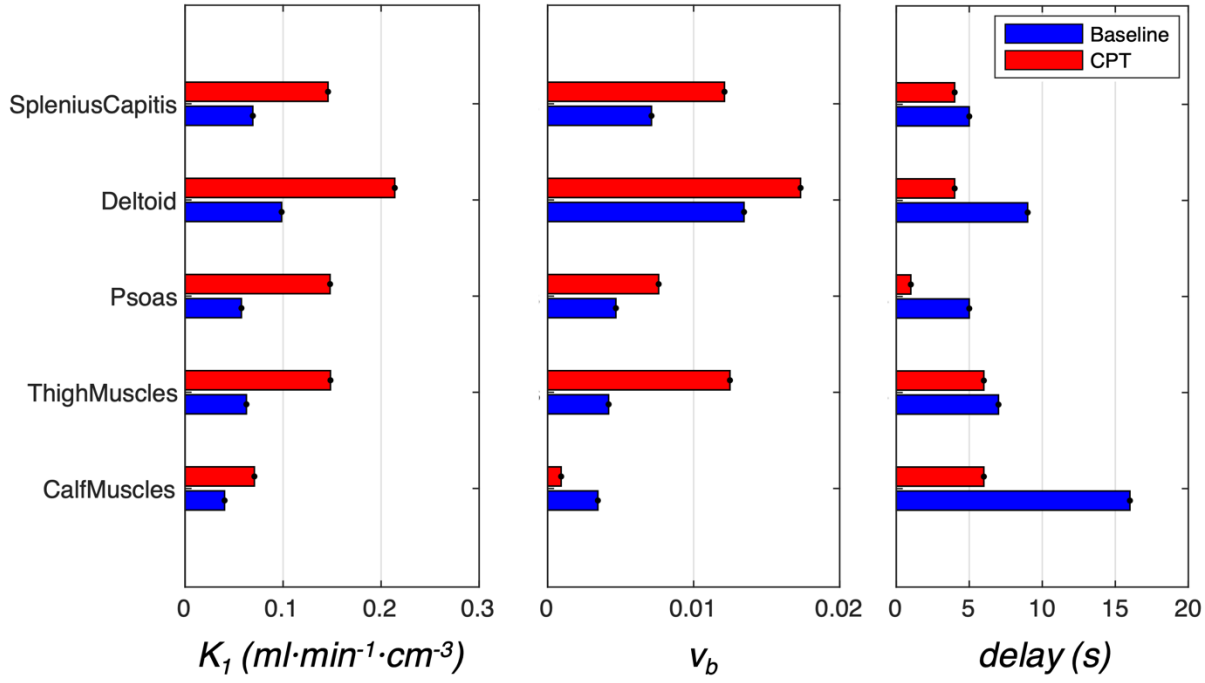

Figure 4.12: Parameter estimates across baseline and CPT acquisitions for skeletal muscle

Figure 4.12: Parameter estimates across baseline and CPT acquisitions for skeletal muscle ROIs. K_1 was approximately double across most muscle ROIs (average increase of 113%) for the CPT study compared to baseline. v_b was also higher (average increase of 33%) in most cases for the CPT data, whereas delay was longer in the baseline data compared to CPT (average decrease of 57%). The calf muscles showed a slight decrease in v_b (0.003 at baseline, to 0.0004 with CPT), though it should be noted that the magnitude of v_b in the calves was the smallest across all tissues.

Initial results for the group 3 PAD patient (N = 1) are shown in table 4.9 for a subset of tissues. Since the patient with PAD had a history of myocardial infarction, table 4.9 includes myocardial parameter estimates in addition to a variety of skeletal muscle regions. Myocardial perfusion for the PAD patient was 21% lower than baseline results in healthy volunteers in table 4.8. Pooled

skeletal muscle K_1 was 170% higher than baseline studies, and roughly 4 times that of the literature value listed in table 4.7.

Table 4.9: PAD parameter estimates (N = 1)

Parameter	Myocardium	Splenius Capitis	Deltoid	Psoas	L Thigh	R Thigh	L Calf	R Calf
v_b	0.237	0.015	0.020	0.019	0.005	0.004	0.002	0.002
K_1 ($ml \cdot min^{-1} \cdot cm^{-3}$)	0.781	0.133	0.140	0.177	0.087	0.086	0.041	0.034
k_2 (min^{-1})	0.940	0.130	0.137	0.150	0.086	0.083	0.053	0.040
delay (s)	-3.00	8.00	9.00	8.00	8.00	8.00	16.00	18.00
AT (s)	180	180	240	240	270	270	270	270

4.8. Representative parametric images

After assessing model selection at the ROI-level, AIC was used to perform voxel-wise model selection between 1T4P and 1T6P models only. Figure 4.13 includes representative cross sectional parametric images of K_1, v_b, and delay for groups 1, 2, and 3. The images in figure 4.13 match ROI-based results, which can be seen especially for skeletal muscle of the CPT subject and PAD patient, which show increased perfusion as compared to baseline or in the affected limb, respectively. Although there was a global increase with the CPT in most of the skeletal muscle groups included in this work (figure 4.12), figure 4.14A shows the large increase in specific muscle groups of the thigh. For the PAD subject, regional perfusion differences in the myocardium due to a history of myocardial ischemia can be observed. Comparison of the left and right calves of the PAD subject can be visualized in the K_1 image in figure 4.13, but cross-sectional views in figure 4.14B also illustrate this.

In figure 4.14B, cross sections of the calves illustrate the localized increases in perfusion in the left, relative to the right, calf muscle of the PAD subject. This was also shown with whole-calf ROIs in table 4.9, albeit with a smaller increase in perfusion across the entire calf. A local K_1 was measured by drawing ellipsoidal regions of interest within the area of increased perfusion and the

corresponding region in the right calf. In the left and right calves respectively, local K_1 values were 0.06 and 0.04 ml·min^{-1}·cm^{-3}, which represents an increase in perfusion of the affected limb of 80% increase relative to the opposing limb.

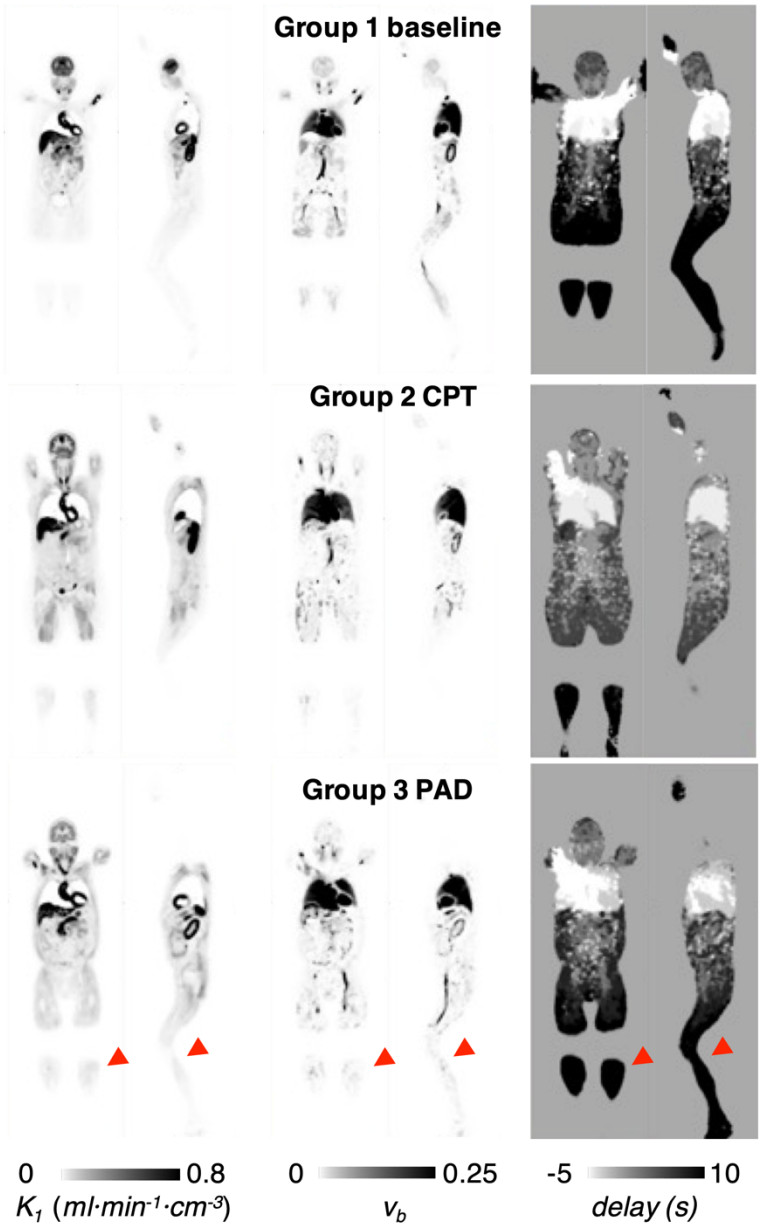

Figure 4.13: Parametric cross-sectional images of K1, vb, and delay for each study group

Figure 4.13: Parametric cross-sectional images of K_1, v_b, and delay for each study group. The red arrows indicate the affected limb of the group 3 PAD patient. Parametric maps were generated

using the 30m29 framing protocol and 4.0x4.0x4.0 mm^3 voxels. The cross-sectional views are centered in the left ventricle, allowing for visualization of many tissue types in the coronal plane, including grey matter, myocardium, liver, and skeletal muscle in the legs. In the sagittal plane, the renal cortex, in addition to the spleen and stomach, can be visualized. Delay maps show the early triggering of the leading edge threshold, or underestimation of delay near the deltoid, due to the bolus injections. As discussed in the text, the skeletal muscle of CPT (group 2) and PAD (group 3) studies exhibit increased K_1 compared to baseline (group 1) images.

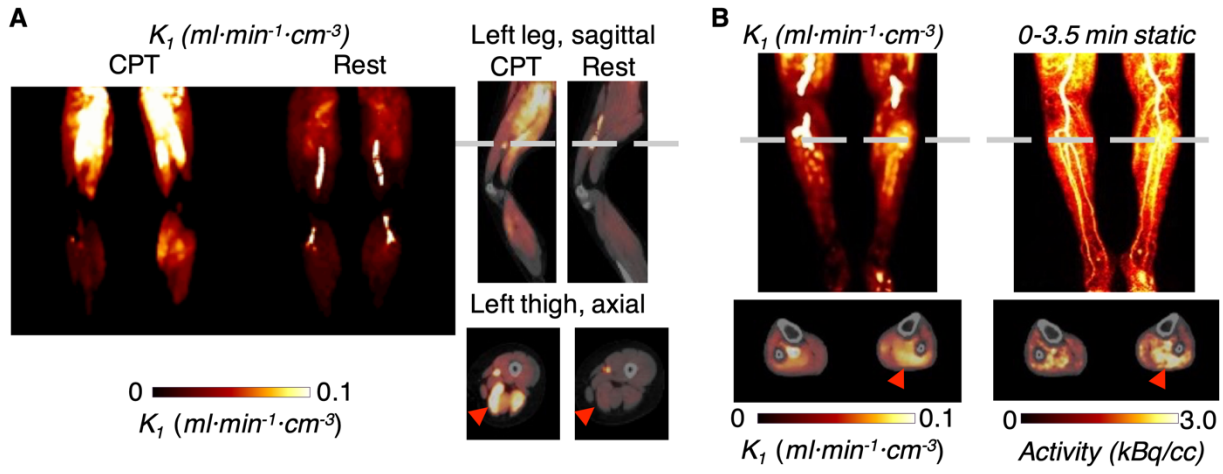

Figure 4.14: Perfusion maps of subjects from groups 2 and 3

Figure 4.14: Perfusion maps of subjects from groups 2 (A) and 3 (B). In (A), visual comparison of the maximum intensity projections (MIPs) of the CPT and baseline or rest K_1 show the increase in perfusion from baseline. Sagittal and axial cross sections illustrate that although there was a global increase in skeletal muscle K_1 in the leg muscle groups, there was a large increase in specific muscle groups of the thigh (arrows). In (B), K_1 and static MIPs show the increased perfusion to the skeletal muscle in the left leg as compared to the right (arrows), which can be visualized in the axial cross sections.

4.9. Discussion

Here we discuss the methods and analyses for [^{11}C]-butanol total-body PET kinetic modeling. As indicated by the sensitivity and AT analyses, AT was inconsequential to the fitting process for most tissues, with sufficiently long AT (>150 seconds). However, some tissues demonstrated a dependence on AT for the stability and estimated values of kinetic parameters. This was particularly evident for the liver, which resulted in unstable estimates at short AT, and the kidneys, which showed a consistent drop in both K_1 and k_2 with increasing AT. In the case of the liver, this dependence on long AT is likely due to the slow rising edges of the liver TACs, which do not peak until approximately 150 seconds (figure 4.1), and thus characterization of the parameter values investigated here require longer AT. AT was tested in 30-second increments, with a temporal resolution of 5 seconds; while the methods discussed here included a variety of ATs and reconstruction protocols, finer sampling of ATs at variable frame lengths may result in improved estimates in the lung, as indicated by figure 4.6. Further, shorter frame lengths may improve characterization of the IDIF and tissue TACs with the increased temporal resolution, especially for tissues with sharper peaks that show a dependence on the temporal resolution. Although not shown here, additional investigation of kidney kinetic parameter estimates with shorter (1 or 2 seconds) frame lengths showed improved parameter stability across ATs.

Additional sensitivity and identifiability analyses showed a strong positive correlation between K_1 and k_2, and a weak negative correlation of v_b with K_1 and k_2. It should be noted that a relationship between [^{11}C]-butanol K_1 and k_2 is not unexpected – based on the principles of fluid transport in the body, it is expected that the flow of fluid to and from the tissue is dictated by hydrostatic and osmotic pressure differences (Swartz & Fleury, 2007). Thus flow back into the blood pool from the tissue (k_2) will be larger or similar in value to the flow into the tissue (K_1), otherwise there

would be fluid accumulation or edema in the tissue. And since [^{11}C]-butanol is injected in trace amounts to investigate perfusion, the measured K_1 and k_2 are expected to follow these same transport principles, where k_2 is larger or similar in magnitude to K_1. Practical identifiability was assessed using Monte Carlo simulations, which showed robust estimation of parameter estimates in most tissues. Liver estimates were less robust to noise, which may be due to the need for additional parameters for modeling the dual blood supply to the liver.

Out of the variety of reconstruction settings tested, voxel size had little to no effect on the ROI-based parameter estimates, while a temporal resolution of 5 seconds for all tissues allowed for the highest agreement of parameter estimates with literature values. As shown in figure 4.6, longer frame lengths resulted in larger delay estimates for most tissues, and resulted in reduced K_1 estimates for most tissues with a sharp peak in figure 4.1 (e.g., thyroid, myocardium, spleen). This agrees with our previous work, in which we demonstrated that temporal resolution influences the LE delay estimates (E. J. Li et al., 2021). Although the estimates produced in this work were compared with existing literature values, it is important to note that the literature values were obtained across a range of methods (including different radiotracers) and scanners with range of temporal and spatial resolutions. While reported values serve as useful comparators for the results produced in this work, it may be the case that improved scanner technology has helped to produce improved estimates of these parameters. Accordingly, the extent of agreement between the 5-second temporal resolution results and literature values could be explained by the inability to perform high spatial and temporal resolution dynamic imaging with previous scanner generations. This may be especially true for v_b, a parameter which may depend more heavily on the partial volume effects imposed by the scanner, the reconstruction parameters, and analysis methods than other parameters; while larger blood vessels are avoided during ROI delineation, v_b represents the

activity present in the smaller blood vessels and capillaries within the tissue. Thus estimation of v_b will depend partially on the underlying magnitude of v_b, as well as the scanner sensitivity and reconstruction parameters to be able to recover this fraction of the activity (which is between 0.003 and 0.2 in table 4.7). Further, as evidenced by the sensitivity curves in figure 4.3, the early portions of the sensitivity curves provide show higher sensitivity to v_b, and thus, higher temporal resolutions may aid in the estimation of v_b.

ROI-based model selection with 5-second temporal resolution showed that correction of the internal dispersion of the IDIF was not necessary for the tissues tested here, with the exception of the liver. However, further investigation of dispersion correction is warranted for dynamic data with increased temporal resolution, since AIC balances the minimization of error with model complexity, and one- or sub-second resolution may better reflect the internal dispersion of the IF.

After fixing AT, reconstruction framing and voxel size, and choice of model, baseline parameter estimates were in agreement with values reported in the literature. Liver and thyroid both showed large discrepancies in v_b, which may be due to spillover from the lung and blood pool in early frames respectively, but investigations of reconstruction framing indicate that the temporal resolution also can lead to differences in the estimated parameters, especially for the liver and thyroid as well as the spleen. Baseline test-retest reproducibility indicated that estimates of perfusion, v_b, and delay are all highly reproducible (Pearson's $r > 0.9$) between visits. Outliers included the kidney, pancreas, spleen, which all may experience variable K_1 due to normal changes in perfusion over the day. The RV IDIF and 1T4P model implemented in this work may not be sufficient to estimate lung perfusion and blood volume, since k_2 exhibited a wide range of values across subjects (0.7-7.2 min^{-1} for 5 s frames and a fixed AT of 60 s). Further, even with high temporal resolution (1-2 s frames), lung v_b was underestimated, and with longer frames, lung K_1

was underestimated (figures 4.6, 4.7). Further investigation with a dual-blood input function for the lung is likely necessary, since the lung also receives blood from the bronchial artery in addition to the pulmonary artery.

With the CPT, a heterogeneous response across organs was expected; previous studies have shown that flow increases in the myocardium (Schindler et al., 2004; Siegrist et al., 2006), in certain regions of the cerebral cortex (Di Piero et al., 1994; Petrovic et al., 2000), in the liver (Keramida et al., 2020), and in the spleen (Galea et al., 2019), while blood flow decreases in the kidneys (Kannenkeril et al., 2021). To our knowledge, this is the first work to investigate changes in skeletal muscle blood flow with PET and the CPT combined, and moreover across multiple muscle groups. In the group 2 subject, K_1 increased substantially in the myocardium (104%) and skeletal muscle (113%) with the use of the CPT. Decreases were also observed in the kidney, thyroid and spleen. Similarly, there were regional differences in perfusion for the group 3 subject with PAD; there was lower myocardial perfusion (-21%) compared to baseline results in healthy volunteers, while skeletal muscle K_1 was higher than in baseline studies (170%). Localization and visualization of the highly perfused region of the left calf in the perfusion map allowed for quantitative assessment of the 80% increase in perfusion compared to the right calf. This increase may be due to increase flow through collateral vessels. Another explanation may be hyperemia (Depairon & Zicot, 1996), though the PAD study occurred when the subject was at rest, and no exercise or walk test was performed prior to the acquisition.

With parametric imaging of perfusion, increased perfusion of specific muscle groups was observed for groups 2 and 3. Voxel-wise delay maps were visually similar to the FDG-based delay maps in chapter 3. However there were three major differences in the methods. First, the minimum frame length for [^{11}C]-butanol reconstructions was 5 seconds, as compared to 2 seconds for FDG

image data. Second, the IDIFs for [^{11}C]-butanol and FDG datasets were derived from the descending aorta and left ventricle respectively. Finally, as discussed in chapter 3 and noted above in relation to the ROI-based delay estimates, frame length influences the delay estimates, and thus, to try and account for this, [^{11}C]-butanol LE delay estimates were determined with a LE threshold of 1%, as opposed to the 10% LE threshold utilized in chapter 3. Visual and quantitative comparisons of parametric LE delay maps from chapters 3 and 4 indicate that they were similar overall. However, [^{11}C]-butanol delay maps showed slightly longer delay estimates in the liver, by roughly 3 seconds. Since the participant, IDIF location, bolus shapes, and temporal framing are different for chapters 3 and 4, minor differences in the delay maps are expected. Nonetheless, in chapters 3 and 4, we demonstrated that LE delay methods can be applied to datasets with different radiotracers, reconstruction protocols, and IDIFs.

This study has several limitations. First, due to the limited number of enrolled subjects in groups 2 and 3, broader interpretations of the intra-subject perfusion values were not possible, since no statistical assessment of the significance of these differences was performed. Second, although the subjects were advised not to drink caffeine two hours prior to the study, there are many factors that may impact perfusion estimates—such as recent exercise and time of day—that may contribute to differences between visits. Third, although eight baseline studies provided reasonable results for K_1 and v_b, test-retest reproducibility was only performed with data from three subjects (and thus six acquisitions). Improved characterization of reproducibility would require increasing the number of subjects. Further intra-subject assessments that would allow for additional statistical analyses, are needed to further assess of the sensitivity of total-body PET/CT to investigate intra-subject changes in perfusion.

4.10. Conclusions

Despite the small number of subjects, the kinetic modeling methods and estimated parameters discussed here provide a basis future PET kinetic modeling work with [^{11}C]-butanol. While these methods were developed with [^{11}C]-butanol total-body PET applications in mind, this work can be implemented for short axial FOV PET/CT systems, assuming an input function, with limited PVE or corrections for PVE, is available, and the early phases of the [^{11}C]-butanol dynamic study capture the tissue of interest, such as the brain. TIDA-based quantification of the exhalation of [^{11}C]-CO_2 may provide a method of metabolite correction for a variety of carbon-11 tracers, which often result in the formation of [^{11}C]-CO_2, and serves as a potential future direction of this work. Based on sensitivity assessments, **AT only needed to be fixed in a tissue-specific manner for three (kidney, liver, lungs) of the twelve tissues**, where the majority of tissues showed stability across ATs. This is important for parametric imaging, since AT may need to be set independently for these tissues as part of the fitting process. Identifiability analyses showed that **reliable estimation of K_1 and k_2 was possible for many tissues,** though K_1 and k_2 estimates for some tissues (e.g., lung, spleen, and thyroid) exhibited broad error landscapes. **Parameter estimates at the ROI-level were stable with the addition of noise.** Higher temporal resolution resulted in over or underestimation of parameter values relative to literature in a few tissues, which warrants further investigation. After establishing methodologies to reproducibly estimate parameters using [^{11}C]-butanol, the final results in baseline studies showed that parameter estimates of K_1 (slope 0.99, r = 0.91, $p < 0.001$), v_b (slope 1.04, r = 0.96, $p < 0.001$), and delay (slope 1.03, r = 0.97, $p < 0.001$) were highly reproducible out to two weeks between acquisitions, and the changes in perfusion identified in the CPT and PAD cases illustrated the ability to perform intra-subject measurements of perfusion with these methods. These methods can be extended to other activation or pressor

methods, and to monitor pathophysiological progression of other perfusion-related diseases.

5. Chapter 5: [^{11}C]-butanol total-body PET dosimetry

5.1. Introduction:

The previous chapter focused on the methodology for total-body PET perfusion studies with [^{11}C]-butanol. Single-organ perfusion studies of specific organs such as the brain and heart to investigate ischemia are performed in humans with tracers such as [^{15}O]-water and [^{13}N]-ammonia (Baron & Jones, 2012; Murthy et al., 2018). However, there are a number of reasons that carbon-11 is a superior radioisotope to utilize for perfusion imaging. First, carbon-11 has a smaller positron range and thus will result in improved image quality relative to oxygen-15, nitrogen-13, and rubidium-82 (Sánchez-Crespo et al., 2004). Second, it has a half-life of 20.3 minutes, which is longer than that of oxygen-15, nitrogen-13, and rubidium-82, allowing for the radiotracer production to occur offsite (although still in close proximity to the scanner) without large increases in effective dose (Zanotti-Fregonara et al., 2021). Third and most importantly, for high flow rates or tissues with a low permeability, such as the heart and brain respectively, PET measurements of perfusion will be underestimated when using [^{13}N]-ammonia and [^{15}O]-water, since they both have been demonstrated to exhibit flow-limited first-pass extraction at high flow rates (>0.6 $ml \cdot min^{-1} \cdot cm^{-3}$) (Quarles et al., 1993; Schelbert et al., 1981). Of note also, is that [^{82}Rb]-RbCl has an extraction fraction of 2% across the blood-brain barrier (Brooks et al., 1984); since [^{82}Rb]-RbCl effectively does not cross the healthy blood-brain barrier, it is not a reasonable candidate for total-body PET perfusion imaging. Thus, we propose to use [^{11}C]-butanol because it is a carbon-11 tracer with a practical extraction fraction of 1 (figure 1.4). However, a limited number of perfusion and dosimetry studies have been performed to date using [^{11}C]-butanol.

Radiation dosimetry involves quantification of radiation dose to an individual and is the science of attempting to quantitatively relate that dose to the potential biological damage it may

cause. When new or investigational radiotracers are used, it is important to understand the radiation dose that may be received by any given subject. Although butanol-related dosimetry and biodistribution estimates have been performed previously, they were mostly performed either in animals (Knapp et al., 1985), or with oxygen-15 instead of carbon-11 labeled butanol (Herzog et al., 1994; Nordberg et al., 1995; Takagi et al., 1984). [^{15}O]-butanol, which involves labeling the hydroxyl group rather than the main carbon chain may have a different biodistribution of the radioisotope over time, and the labelling radionuclide is also different. Jackson and others published a comprehensive collection of their dose estimates, including those for [^{11}C]-butanol, but study details were limited (Jackson et al., 2020). Further, no carbon-11-based tracers had previously been utilized with the uEXPLORER PET/CT system at UC Davis. Since there is no cyclotron on-site for the uEXPLORER, careful consideration of the safety and timing of [^{11}C]-butanol production and delivery was needed. Thus, additional investigations of [^{11}C]-butanol dosimetry and of the study timing were first assessed in rhesus macaques at the California National Primate Research Center, which also required utilizing an off-site cyclotron, prior to moving forward with [^{11}C]-butanol in-human studies.

Total-body PET also allows a unique opportunity in the measurement of human dosimetry for radiotracers with rapid kinetics and short half-life. As discussed in sections 2.2 and 4.2.3, changes in the activity distribution throughout the entire body can be measured since most subjects fit within the imaging FOV of the scanner. Assuming accurate scanner calibration, any activity lost, such as through voiding, can be accounted for through the comparison of the total image-derived activity (TIDA) and the injected dose (i.d.). Large discrepancies between the assayed dose and TIDA can be identified, preventing large erroneous fluctuations in dose estimates. In this work, for example, decreases in activity that occur due to the exhalation of [^{11}C]-CO_2 can be accounted

for, enabling more quantitatively accurate dosimetry measurements, particularly for short-lived radioisotopes, such as carbon-11. In this chapter, dosimetry estimates were performed for [^{11}C]-butanol initially in rhesus macaques and subsequently in human subjects.

5.2. Materials and methods:

5.2.1. Image data

Preliminary studies in juvenile rhesus macaques were performed (N=2; male: 3.6 kg, female: 2.5 kg, 2-3 years) for extrapolation to human studies under the guidance and approval of an Institutional Animal Care and Use Committee. The male and female rhesus subjects were injected with 85.1 and 173.3 MBq of [^{11}C]-butanol respectively and scanned for 75 minutes on a prototype small-scale total-body PET scanner, the mini-EXPLORER I system (Berg et al., 2018), which was developed for the imaging of nonhuman primates and has an axial FOV of 46 cm. The mini-EXPLORER I images were reconstructed using in-house reconstruction software with 102 frames, as listed in table 5.1 under the designation 75m102. Standard corrections (attenuation, scatter, randoms, deadtime, and decay) were applied. OLINDA 2.0 (Stabin et al., 2005) was used for extrapolation of rhesus macaque data for human dosimetry estimates to the human adult ICRP 89 models.

Table 5.1: Temporal framing and reconstructed image sizes

Designation	Framing	Matrix size	Voxel size
75m102	30x2 s, 24x5 s, 15x20 s, 12x60 s, 16x120 s, 5x300 s	323x323x445x102	1.0 x 1.0 x 1.0 mm^3
30m29	12x5 s, 6x10 s, 6x30 s, 5x300 s	150x150x486x29	4.0 x 4.0 x 4.0 mm^3

Human studies were performed for 6 healthy volunteers (2 male, 4 female, body mass index (BMI): 20.9-30.0 kg/m^2, 28-64 years) and 1 subject with PAD (BMI: 23.4 kg/m^2, 66 years). The study was performed under the guidance and approval of an Institutional Review Board and a Radioactive Drug Research Committee, with informed consent from all participants. A subset of the healthy volunteers (N = 3) underwent two baseline acquisitions less than two weeks apart. As discussed in chapter 4, three healthy volunteers were enrolled for a rest-stress study with the cold pressor test (CPT). However, due to radiochemistry challenges, one subject participated in the CPT study only, while another was only imaged at rest. This resulted in a total of 11 [^{11}C]-butanol scans. Subjects were injected with a bolus of [^{11}C]-butanol (mean: 279.1, range: 190.6-348.6 MBq) at the start of a 30-minute dynamic acquisition on the uEXPLORER PET/CT system (Leung, Berg, et al., 2021; Spencer et al., 2021). Dynamic images were reconstructed with 29 frames using the reconstruction parameters listed under the label 30m29 in table 5.1. Vendor-provided reconstruction software was used to generate the 4-D images, and corrections for attenuation, scatter, randoms, deadtime, decay were applied. No point-spread function modeling was applied. One CPT study was ended at ten minutes post-injection due to failure of the cold pressor pump. Absorbed dose estimates were determined from pooled studies across groups, such that dose estimates for the PAD subject was included, and for subjects that had two visits, the first visit was used for calculating the average and standard deviation of the dose estimates.

5.2.2. TIDA

TIDA curves were generated for rhesus and human acquisitions to assess the loss of carbon-11 in the form [^{11}C]-CO_2 over the course of the study and its impact on dose estimates. However, since there is no ground truth in this context for the determination of TIDA bias since the loss of activity is expected, TIDA percent change was used instead, which is identical in calculation to TIDA bias:

$$TIDA(m) = V \times \sum_i A_i\,(m) \tag{5.1}$$

$$TIDA\ percent\ change\ (m) = 100\% \cdot \frac{TIDA(m) - i.d.}{i.d.} \tag{5.2}$$

where V is the voxel volume in milliliters, $A_i(m)$ is the activity concentration in frame m for pixel i (units MBq/ml) and *i.d.* is the injected dose (MBq).

5.2.3. Dosimetry estimates

After injection of the radiotracer, the overall distribution in the body is dependent on both the biodistribution and physical decay of tracer over time. Dose is typically reported in terms of absorbed dose D_k (units Gy) which can be reported per unit of administered activity with units Gy/MBq. D_k is a measure of how much energy, in joules, is absorbed per kilogram of absorbing tissue k. Dose deposited to and emitted from various organs can be calculated using OLINDA 2.0 and the Medical Internal Radiation Dose (MIRD) method from the Society of Nuclear Medicine (Stabin & Farmer, 2012). For an organ of interest (also called target) r_k, the total absorbed dose from h source organs is equal to:

$$\overline{D}(r_k) = \sum_h \overline{D}(r_k \leftarrow r_h) = \sum_h \frac{\tilde{A}}{m_k} \sum_i \phi_i(r_k \leftarrow r_h)\Delta_i = \sum_h \tilde{A} \times S \tag{5.3}$$

where $\tilde{A}$ is the cumulated activity (or integrated area under the time activity curve) in MBq·sec for r_h, m_k is the mass of r_k, $\phi_i(r_k \leftarrow r_h)$ is the fraction of energy absorbed from r_h by r_k, and Δ_i is the equilibrium absorbed dose constant with units (Gy·kg)/(MBq·sec), which accounts for the how much radiation energy is emitted from the ith type of emission (e.g., gamma or x-ray) (Cherry et al., 2012). ϕ has been determined for a number of simulated anthropomorphic phantoms by the International Commission of Radiological Protection (ICRP), which allows for equation 5.3 to be simplified by substituting in the mean dose per unit cumulated activity, or S factor (also called dose factor), for each source-target organ pair. The S factor thus represents the physical phenomena associated with absorbed dose, including the emission type and the physical distance between

source-target organ pairs, while the cumulated activity $\tilde{A}$ accounts for the half-life of the radioisotope and the uptake and distribution of the tracer in the body. $\tilde{A}$ can be determined using the dynamic image data and the following equation:

$$\tilde{A} = V_{r_k} \int_0^\infty A_{r_k}(t)dt \tag{5.4}$$

where A_{r_k} represents the time activity curve (TAC) for organ r_k at time t, and V_{r_k} is the volume of organ r_k based on the ICRP 89 male and female adult models (Valentin, 2002). $\tilde{A}$ is a similar to TIDA, since they both require converting from activity concentration (MBq/ml) to activity (MBq), except $\tilde{A}$ is also a cumulative measurement across time with units MBq·sec. Thus, for dose estimation for both rhesus macaques and human subjects, organ TACs (in kBq/cc) were the only information obtained based on the image data; the separate dose factors S for male and female adults models published in ICRP 89 were used to account for organ masses and volume, organ positioning, and the emission type.

TACs were used to determine the cumulated activity $\tilde{A}$ in equation 5.4 through trapezoidal integration and an exponential fit of the non-decay corrected tail out to infinity, or zero activity based on the half-life of carbon-11. The TACs were derived from tissue regions of interest (ROIs) delineated initially using the CT for anatomical reference. As discussed in chapters 2 and 4, an average image of the dynamic PET series was then used to minimize the effect of motion on ROI placement. However, to produce conservative estimates of the activity within organs, partial volume effects were ignored in that no morphologic operations (e.g., erosion) were applied to the dosimetry ROIs, resulting in higher activity due to spillover in tissues like the heart wall and thus more conservative estimation of absorbed dose in regards to radiation safety. It should also be noted that rhesus and human subjects were scanned for 3.7 and 1.5 half-lives of carbon-11. Since loss of carbon-11 occurs through the exhalation of [^{11}C]-CO_2 beyond the end of the acquisition,

extrapolation to infinity is a conservative method of dose estimation. After determining *D* at the organ level, the effective dose, *E* was also estimated. *E* has units of Sieverts (Sv), and is equal to the weighted summation of the organ-based absorbed doses, as show in the following equation:

$$E = \sum_k w_k w_R \bar{D}(r_k) \quad (5.5)$$

where w_k is the tissue-specific weighting factor to account for the organ-specific differences in dose risk as determined by the ICRP, and w_R is a weighting factor to account for the type of radiation, which for positron-emitting radionuclides, is equal to 1.

5.2.4. In-human test-retest reproducibility

For the three human subjects that were scanned twice at rest, test-retest reproducibility of the absorbed dose estimates was assessed through correlation analysis. Bland-Altman plots were generated with 95% limits of agreement, using the Kolmogorov-Smirnov (KS) test for normality. Pearson's *r* was used to assess the correlation of doses between visits.

5.3. Results:

5.3.1. Rhesus macaque dosimetry

Cross sectional views of one study are shown in figure 5.1. The tracer uptake peaked in the brain and heart by roughly 4 minutes. Over the course of the 75-minute study, there was rapid clearance in the brain and heart, and slower clearance from the gut and liver. Non-decay and decay corrected TACs for a subset of organs are included in figure 5.2. Organ absorbed doses are listed in table 5.2. The kidneys were found to have the highest absorbed dose (uGy/MBq) for both female (21.60 uGy/MBq) and male (17.70 uGy/MBq) rhesus monkeys. Additional critical organs were the right ascending colon (female: 15.60 uGy/MBq; male: 9.25 uGy/MBq) and left descending colon (female: 11.30 uGy/MBq; male: 9.18 uGy/MBq). Female and male effective doses were 4.35 and 3.00 uSv/MBq.

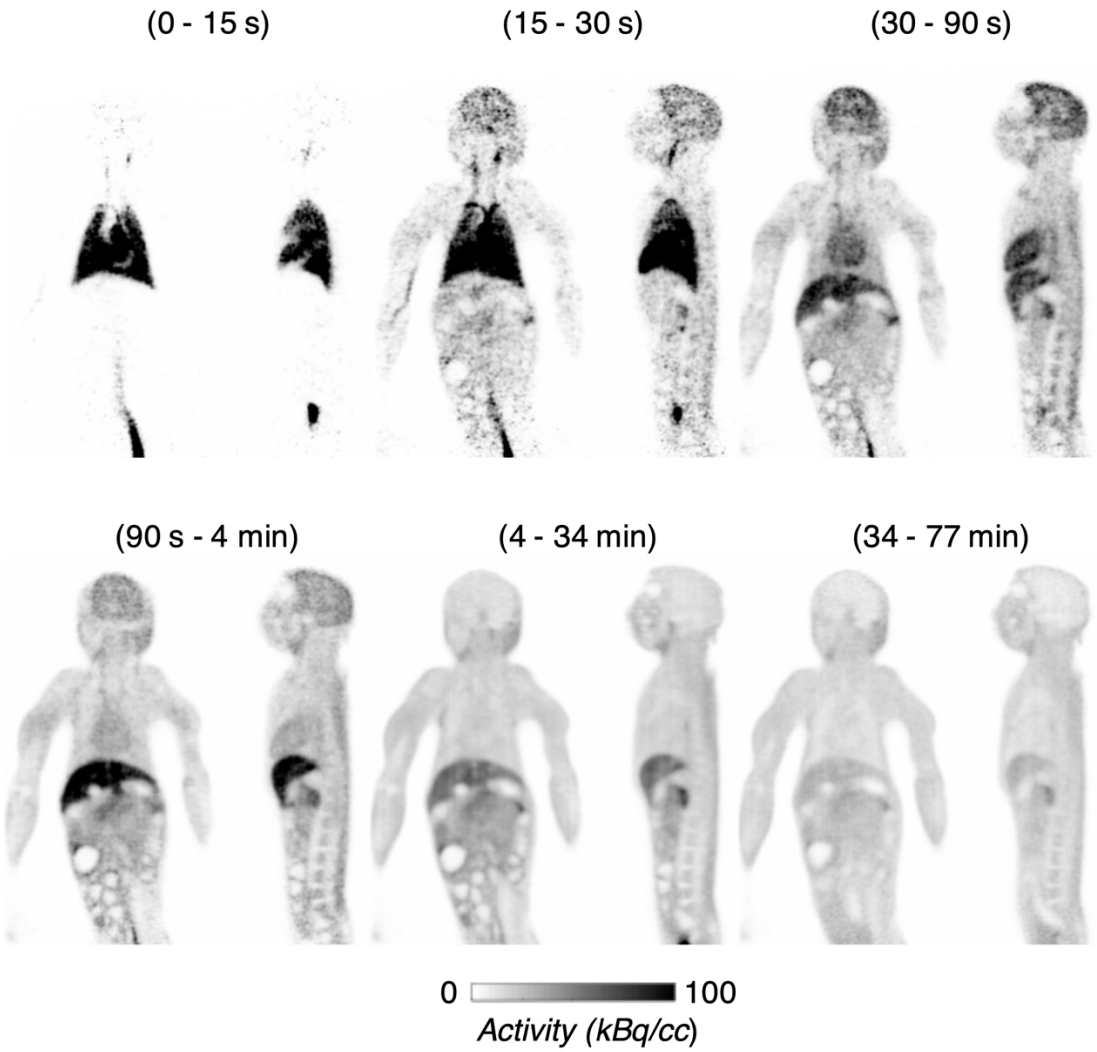

Figure 5.1: Coronal and sagittal cross sections of the male rhesus dynamic PET acquisition

Figure 5.1: Coronal and sagittal cross sections of the male rhesus dynamic PET acquisition over time. Image frames were reconstructed with the 75m102 protocol listed in table 5.1 and then rebinned. During the first few minutes of the study (top row), [^{11}C]-butanol was delivered to tissues throughout the body. Increased uptake was observed in the heart, brain and liver in the first 4 minutes of the study. By 34 to 77 minutes post-injection, the tracer distribution was lower in the brain compared to the liver and walls of the intestines. Images shown in this figure are corrected for decay and thus reflect tracer concentration and distribution rather than activity. Non decay-corrected activity images were used for dosimetry estimation.

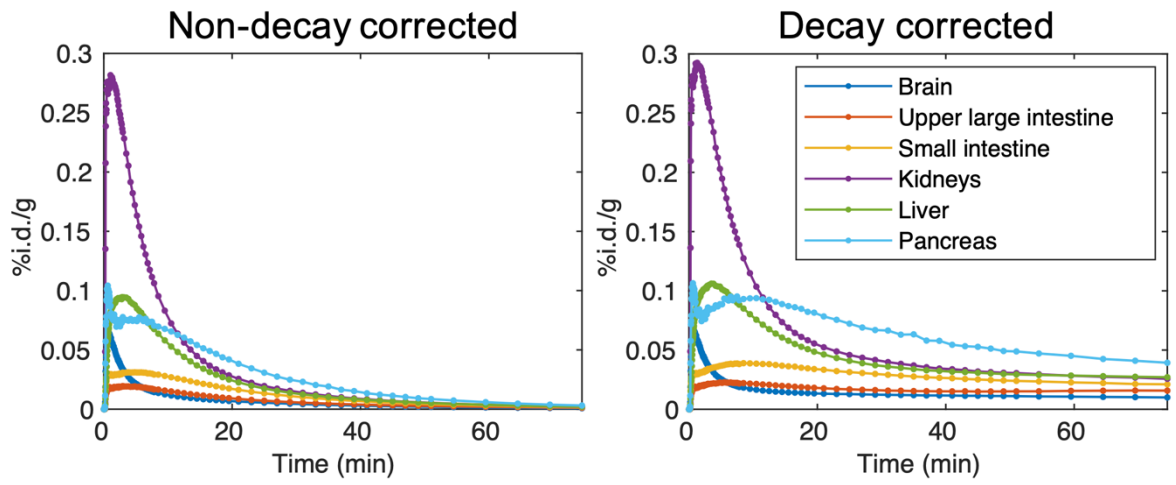

Figure 5.2: Non-decay corrected and decay corrected TACs

Figure 5.2: Non-decay corrected (left) and decay corrected (right) TACs from the male rhesus subject in a number of organs. By the end of the 75-minute acquisition, activity was the highest in the pancreas, which showed a non-decay corrected activity of 0.003 %i.d./g.

Compared to human TIDA plots, the rhesus TIDA plots showed a larger drop relative to injected dose over time, but TIDA drop-off was fairly linear in both species. TIDA plots for a representative rhesus macaque and a representative human subject are shown in figure 5.3. The total activity in the animal decreased by an average of 0.53% per minute, compared to 0.37% per minute for the human subject (figure 5.3, left). However, during the first 5 minutes the TIDA curve was relatively flat (figure 5.3, right) for both representative subjects. Since blood flow measurements and kinetic modeling only rely on the first 4 to 5 minutes of the scan, this loss of carbon-11 via the exhalation of [^{11}C]-CO_2 throughout the scan does not impact perfusion estimates.

Table 5.2: Absorbed doses of [^{11}C]-butanol in rhesus macaques		
	Absorbed dose (uGy/MBq)	
Target Organ	Adult Female	Adult Male

Adrenals	4.15	3.62
Brain	2.10	1.51
Breasts	1.88	-
Esophagus	2.51	1.88
Eyes	1.74	1.17
Gallbladder wall	4.99	3.65
Left colon	**11.30**	**9.18**
Small intestine	10.50	8.16
Stomach wall	3.06	2.07
Right colon	**15.60**	**9.25**
Rectum	2.42	1.77
Heart wall	2.38	1.61
Kidneys	**21.60**	**17.70**
Liver	7.05	4.77
Lungs	7.62	6.22
Ovaries	2.65	-
Pancreas	4.74	3.79
Prostate	-	1.72
Salivary glands	1.90	1.38
Red marrow	2.04	1.39
Osteogenic cells	1.72	1.29
Spleen	3.82	2.94
Testes	-	1.32
Thymus	2.63	1.67
Thyroid	2.14	1.62
Urinary bladder wall	2.21	2.04
Uterus	2.67	-
Total body	2.68	1.75
Effective dose (uSv/MBq)	**4.35**	**3.00**

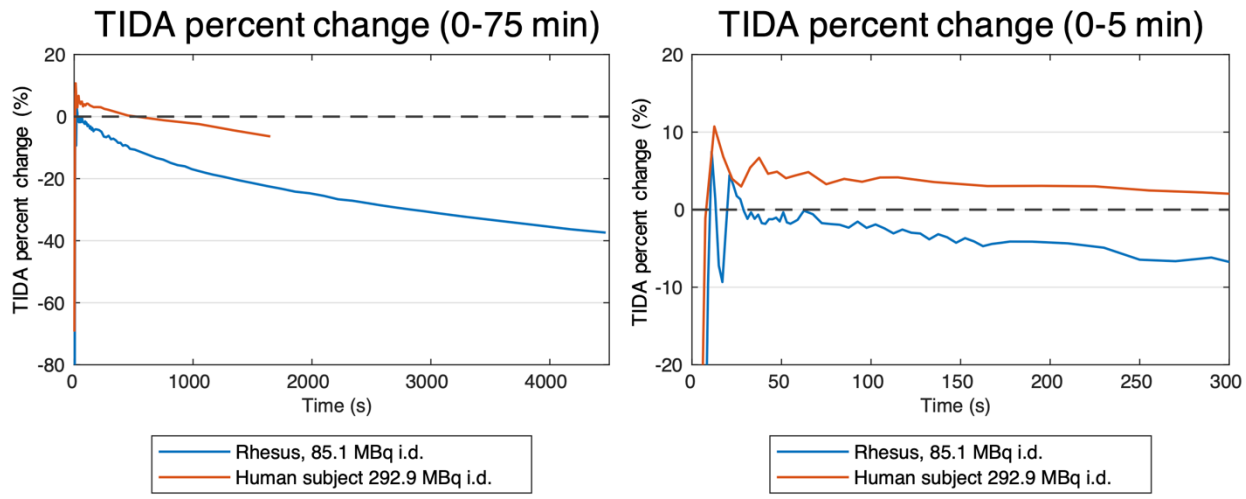

Figure 5.3: TIDA percent change in representative rhesus and human subjects

Figure 5.3: TIDA percent change in representative rhesus and human subjects relative to injected dose. As shown in the left plot, TIDA for the rhesus subject dropped by 40% over the course of the 75-minute study. Assuming a linear relationship based on the left plot, this corresponds to a rate -0.53% per minute. The human subject experienced a loss of approximately 11% over the 30-minute acquisition, or 0.37% per minute. However, the change in TIDA in the first five minutes (right) was relatively flat for both subjects, which is important for kinetic modeling. Although there exists a positive bias of the TIDA curve for the human subject, it is within the expected bias range of the system (Leung, Berg, et al., 2021).

5.3.2. Human dosimetry

Table 5.3 shows the average absorbed doses across one scan from each of the 7 human subjects included in this work for subjects scanned more than once, their first scan was included in table 5.3. Highlighted and in bold in table 5.3, the critical organs for both male and female subjects were the liver (male: 11.28 ± 2.95 uGy/MBq, female: 12.04 ± 6.14 uGy/MBq), pancreas (male: 9.51 ± 1.92 uGy/MBq, female: 12.42 ± 3.27 uGy/MBq), and kidneys (male: 9.08 ± 3.37 uGy/MBq,

female: 10.02 ± 1.97 uGy/MBq). Average male and female total effective doses were 3.24 ± 0.45 and 3.95 ± 0.66 uSv/MBq respectively.

Table 5.3: Average absorbed dose of [^{11}C]-butanol in 7 studies				
	Mean (s.d.) absorbed dose (uGy/MBq)			
Target organ	Female (N = 4)		Male (N = 3)	
Adrenals	4.83	(1.05)	4.30	(0.51)
Brain	3.48	(0.64)	2.70	(0.55)
Breasts	2.27	(0.23)	-	-
Esophagus	3.18	(0.52)	2.80	(0.09)
Eyes	2.27	(0.20)	1.90	(0.17)
Gallbladder wall	5.63	(1.85)	5.88	(0.32)
Left colon	4.64	(0.90)	4.52	(0.67)
Small Intestine	6.79	(1.42)	4.82	(0.90)
Stomach wall	3.75	(0.50)	3.65	(0.38)
Right colon	4.43	(0.72)	4.10	(0.31)
Rectum	4.47	(0.63)	3.36	(0.34)
Heart wall	8.76	(1.20)	7.61	(2.26)
Kidneys	**10.02**	**(1.97)**	**9.08**	**(3.37)**
Liver	**12.04**	**(6.14)**	**11.28**	**(2.95)**
Lungs	3.88	(0.94)	3.36	(0.67)
Ovaries	3.01	(0.26)	-	-
Pancreas	**12.42**	**(3.27)**	**9.51**	**(1.92)**
Prostate	-	-	4.41	(0.63)
Salivary glands	2.39	(0.21)	2.18	(0.21)
Red marrow	4.06	(0.54)	3.21	(0.43)
Osteogenic cells	3.94	(0.42)	3.42	(0.29)
Spleen	7.94	(1.53)	6.74	(1.32)
Testes	-	-	2.33	(0.96)
Thymus	3.00	(0.31)	2.62	(0.06)
Thyroid	5.20	(1.34)	4.59	(0.86)
Urinary bladder wall	3.48	(1.54)	2.69	(0.28)
Uterus	3.05	(0.25)	-	-
Total Body	3.14	(0.42)	2.57	(0.08)
Effective dose (uSv/MBq)	**3.95**	**(0.66)**	**3.24**	**(0.45)**

5.3.3. Test-retest reproducibility

Correlation and Bland-Altman plots assessing the reproducibility for the estimated absorbed doses of the three test-retest human subjects are shown in figure 5.4A and 5.4B respectively. Absorbed doses were highly correlated (slope 0.9, $r = 0.97$, $p < 0.001$), and after confirming normality using

the KS test, a Bland-Altman plot showed agreement at lower absorbed doses, with increasing variability at higher average dose. In order of decreasing absolute difference in absorbed dose, the liver, pancreas, and heart wall for subject 2, and the liver and heart wall for subject 3 were outliers.

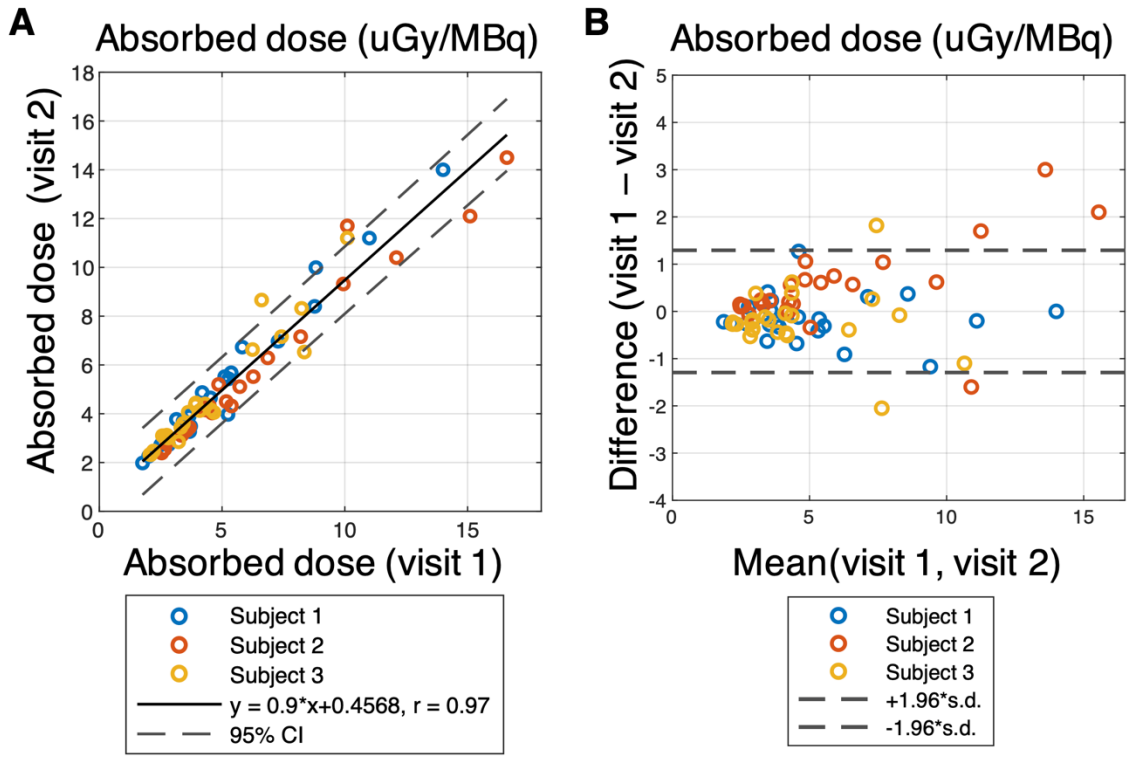

Figure 5.4: Correlation analysis of test-retest dosimetry estimates

Figure 5.4: Correlation analysis of test-retest dosimetry estimates. Dose estimates to individual organs (A) were highly correlated, with a slope of 0.9 and a Pearson's r of 0.97 ($p < 0.001$). Bland-Altman plot of the dose estimates in (B) showed larger differences for tissues with higher absorbed dose estimates. Outliers included the liver, pancreas and heart wall for subject 2, as well as the liver and heart wall for subject 3. A KS test confirmed normality of the absorbed dose estimates.

5.4. Discussion

In this chapter, total-body PET dosimetry was assessed for [^{11}C]-butanol. With the long axial FOV

of total-body PET/CT system, dosimetry estimates can be made for any short-lived radiotracer like carbon-11 without moving the bed or loss of information due to the axial FOV. Initial studies in nonhuman primates, specifically rhesus macaques, demonstrated the feasibility of off-site [^{11}C]-butanol production for the subsequent work in humans. Additionally, these rhesus datasets were used to assess the radiation dosimetry associated with [^{11}C]-butanol, which was not previously investigated in total-body PET settings. The total effective doses determined from both rhesus monkey- and human-derived cumulated activities were very similar (rhesus average: 3.67 uSv/MBq, human average: 3.65 uSv/MBq). The critical organs for the rhesus subjects were the kidneys, left colon, and right colon, with average absorbed doses of 19.3, 12.4, and 10.24 uGy/MBq, respectively. However, human-based results showed the liver (male: 11.28 ± 2.95 uGy/MBq, female: 12.04 ± 6.14 uGy/MBq), pancreas (male: 9.51 ± 1.92 uGy/MBq, female: 12.42 ± 3.27 uGy/MBq), and kidneys (male: 9.08 ± 3.37 uGy/MBq, female: 10.02 ± 1.97 uGy/MBq) as the critical organs. Since there was greater loss of [^{11}C]-CO_2 over time for the rhesus subjects (figure 5.2), sedation and species-related differences in the metabolism and breakdown of [^{11}C]-butanol may play role in the differences in absorbed doses to different organs.

Additionally, the rhesus monkeys were juveniles as noted above. Juvenile rhesus monkey organ-level activities A were utilized to extrapolate the rhesus datasets to the human adult ICRP 89 models under the assumption that there were no age- or size- related differences in the activity concentration distribution over time, and that there was no need for corrections for organ mass differences, as is considered necessary for human dose estimates from rat and mouse cumulated activities, where organ masses and body sizes differ by two orders of magnitude or more (Macey et al., 2001; Tian et al., 2011). Although only 3.7 and 1.5 half-lives were accounted for during the rhesus and human acquisitions respectively, effective doses were similar to those reported for other

carbon-11 tracers as well as the limited number of [^{11}C]-butanol dosimetry tables available (Jackson et al., 2020).

Absorbed dose estimates in humans with up to two weeks between baseline visits were strongly in correlated (slope 0.9, $r = 0.97$, $p < 0.001$). Outliers included the liver, pancreas, and heart wall, which all may play a role in the metabolism of [^{11}C]-butanol either through the action of alcohol dehydrogenases, or fatty acid metabolism (Carlson, 1994). The higher doses observed for females were expected and have been observed with other radiotracers (Stabin & Siegel, 2018; Tian et al., 2011), due to sex-based differences in basal metabolic rates, body mass, height, as well as differences in the activity of alcohol dehydrogenases in the liver (Chrostek et al., 2003; Soldin & Mattison, 2009).

5.5. Conclusions

In this work, radiation dose for [^{11}C]-butanol was assessed using total-body PET in rhesus macaques and humans. TIDA percent change curves were useful for assessing the dose loss observed in both species through exhalation of [^{11}C]-CO_2. Total effective doses for rhesus monkeys were 4.35 and 3.00 uSv/MBq for female and male subjects respectively. The results were similar in humans, where for female and male subjects, the total effective doses were 3.95 ± 0.66 and 3.24 ± 0.45 uSv/MBq respectively. Test-retest assessments demonstrated that these methods are repeatable with the second visit occurring out to two weeks. Total-body PET is an effective tool for radiation dosimetry estimates to all organs and tissues for tracers with rapid kinetics and short half-life which could not be simultaneously captured on a conventional PET scanner.

6. Conclusions and future directions

This thesis focused on quantitative methods for total-body PET kinetic modeling, in particular, the development of methods to quantitatively and reproducibly assess the various organs present in the FOV of total-body dynamic PET images. The physiological goal of these developments was to use a non-invasive, central IDIF in the left ventricle or descending aorta (or the right ventricle for lung tissue) to assess total-body glucose transport and metabolism using the tracer [^{18}F]-FDG, and perfusion using the radiotracer [^{11}C]-butanol. Prior to model fitting, quantification-related challenges that are associated with improved system sensitivity of the uEXPLORER total-body PET/CT needed to be addressed. In chapter 2 we introduced *in vivo* metrics to quantitatively assess biases between software updates, including methods based on total image-derived activity. In addition, motion compensation strategies during ROI delineation were developed for a wide range of organs, where organ-specific motion and partial volume effects can lead to large discontinuities in the measured TACs.

In chapter 3, we took inspiration from pulse-timing methods in PET instrumentation and implemented a leading-edge method for delay correction between the IDIF and tissue of interest in fourteen healthy volunteers and seven genitourinary cancer patients. Compared to the conventional joint estimation method, the leading-edge method resulted in improved computational efficiency of parametric imaging by a factor of 6.7. This increase in computational efficiency was obtained without a major loss in accuracy in estimating delay, as shown for ROI-based TACs (slope 1.00, Pearson's $r = 0.96$, $p < 0.001$) and for parametric imaging of representative subjects (healthy subject: slope 1.01, $r = 0.99$, $p < 0.001$; GUC subject: slope 1.10, $r = 0.99$, $p < 0.001$). Thus, the leading-edge method was demonstrated to be an efficient surrogate

of joint estimation for accurate ROI-based and voxel-wise kinetic modeling, accounting for a range of delay values seen across the body.

In chapter 4, the methods developed in chapters 2 and 3 were extended to [^{11}C]-butanol total-body PET perfusion imaging. Sensitivity and identifiability analyses were used to assist in the setting of optimal acquisition time and temporal framing. After assessing the impact of reconstruction settings and performing model selection, [^{11}C]-butanol K_1, v_b, and delay were estimated in all studies. Test-rest assessments showed that these methods were reproducible in most tissues throughout the body, the major exception being the lungs, though accounting for the dual-blood input and finer assessment of the acquisition time may improve reproducibility. Intra-subject assessment with the CPT showed heterogenous responses across organs, with the largest changes in perfusion in the myocardium (104%) and skeletal muscles (113%). For the PAD subject, there was a localized increase in perfusion of 80% compared to the same region in the opposing limb. The PAD subject also showed increased perfusion across muscle groups as compared to resting healthy volunteers (170%), and decreased perfusion in the myocardium (-21%). Together, these results suggest that [^{11}C]-butanol total-body perfusion imaging is reproducible and sensitive to changes in perfusion due to a rest-stress paradigm as well as PAD-related changes in perfusion from limb to limb. However, additional subjects are needed to confirm these findings.

The dosimetry estimates produced in chapter 5 showed consistency across species for estimation of effective dose, but slight differences in the dose distribution to different organs between species. With the total-body PET FOV, we were able to account for the loss of [^{11}C]-CO_2 during the studies using TIDA plots, which showed a faster rate of exhalation of [^{11}C]-CO_2 in rhesus compared to human subjects. Thus, careful interpretation of [^{11}C]-butanol dose estimates from nonhuman primates such as rhesus macaques is needed to extrapolate the results to humans.

Validation of [^{11}C]-butanol dosimetry was further performed in human subjects. Test-retest reproducibility also showed agreement (slope 0.9, $r = 0.97$, $p < 0.001$) of dosimetry for visits less than 2 weeks apart.

Due to the large number of tissue types interrogated in this work, comprehensive literature searches for perfusion and v_b in a variety of organs were performed, and values were aggregated which may serve as a useful unified resource of v_b and K_1 for perfusion tracers such as [^{11}C]-butanol. Moreover, the ROI-based estimates and parametric maps produced in this work (v_b, delay, FDG K_1, FDG K_i, and [^{11}C]-butanol K_1) were obtained at a variety of temporal resolutions, and may serve as tracer-specific references for these parameters moving forward.

Throughout chapters 2, 3, and 4, methods that assessed the impact of reconstruction software updates, and perturbations of various model parameters (e.g., leading edge threshold, model complexity) were developed, resulting in an improved understanding of how these factors affect kinetic parameter estimates. This is especially important as the sensitivity and image resolution of PET/CT systems continue to improve, since quantification at higher spatial and temporal resolutions can result in large differences in the estimated kinetic parameter values compared to previously published work. Additionally, further generational improvements in long axial FOV scanner technology may require further improvements to the computational efficiency of parametric imaging to increase the clinical utility of quantitative PET kinetic modeling. Future directions of this work, which are discussed in more detail in the following sections, are fivefold: (1) incorporation of ROI-based information for total-body PET parametric image generation and motion correction, (2) incorporation of more complex models, and an in-depth investigation of the relationship between delay and dispersion corrections, (3) further human evaluation of [^{11}C]-butanol perfusion imaging, with additional rest-stress and PAD acquisitions, (4) additional

permutations over combinations of acquisition-related variables and their impact on total-body PET kinetic modeling (e.g., injected dose, finer sampling of acquisition times for [^{11}C]-butanol), and (5) dual tracer studies with both FDG and [^{11}C]-butanol, the radiotracers evaluated in this thesis.

6.1. Incorporation of ROIs for parametric imaging or motion correction

As discussed in chapters 3 and 4, the leading edge method for delay correction is sensitive to changes in the noise levels and temporal framing, which can lead to biases in the estimated parameters. At the voxel level and with shorter frames, noise levels are increased, which can lead to artifacts in the estimation of delay (e.g., from the injection, figure 3.3, figure 4.13). With limited subject motion, the strategies listed in tables 2.2 and 4.3 to delineate various organs can be used to create masks to set tissue-specific delay values, select the kinetic model implemented, or fix other parameters such as v_b for entire organs. These techniques will improve parametric image quality and further reduce the computational burden of these methods. While only a single fixed ROI (e.g., ROI of the kidney cortex delineated using an averaged image) can be used for mask-based parameterization, evaluation of the appropriate ROI for this task is another possible application of this work. This may be especially challenging to implement in organs or large tumor lesions that show heterogeneity in delay estimates (e.g., kidney cortex versus medulla), since spatial resolution and ROI size may play a role in the resulting delay estimates.

Additionally, motion correction methods for total-body PET are actively being investigated in our group (T. Li et al., 2020, 2021). The manual ROI strategies included in chapters 2 and 4 may be used to determine motion-compensated TACs to serve as a ground truth dataset for evaluation of automated motion correction algorithms that use image registration, machine learning, or list-

mode information for motion correction. The methods utilized here to assess changes in parameter estimates due to technical considerations, such as changes in the temporal framing or leading edge threshold, may be leveraged to assess motion correction results and encourage quantitative data fidelity.

6.2. Investigation of additional models, dispersion

To compare results to literature values, this dissertation implemented compartment models and modeling methods commonly used in single-organ studies. However, with the increased temporal resolution made possible with total-body PET, models that incorporate additional corrections to the input function can be included, such as dispersion correction. Dispersion correction was found only to be necessary for the liver in chapter 4, where a dual-blood input function was also beneficial. But with additional investigations of AT and temporal framing, dispersion correction may prove to be important to the stability of parameter estimates for other tissues such as skeletal muscles or the lungs. Similar to the liver, the lungs receive additional blood supply from the bronchial arteries. Thus, modeling of the pulmonary dual-blood input function and dispersion may also improve the stability of perfusion estimates.

Additional tissue compartments can also be included to better account for the underlying physiology. For example, K_1 in this work represents the rate of transport of the radiotracer from the blood to the inside of individual cells, but the traversal of the tracer through the extracellular space between the blood vessel and the cell membrane can possibly be modeled as a separate compartment with sufficiently high temporal resolution (e.g., 2 s). This additional compartment may be particularly important in diseases that can result in regions of necrosis such as cancer, where the vasculature becomes disorganized, or the distance between vessel walls and the tumor cell membranes becomes so large that the tumor cells experience hypoxia (Dewhirst & Secomb,

2017; Krogh, 1919). Others in our group are actively investigating the potential of such models (Tran et al., 2022; Y. Wang et al., 2020).

6.3. Additional CPT, PAD studies for [^{11}C]-butanol sensitivity assessments

As discussed in chapter 4, only single-subject assessments for groups 2 and 3 (CPT rest-stress and PAD groups respectively) have been performed to date. Additional subjects are needed to understand the inter-subject variability of these responses, and whether the results discussed here are generalizable to larger study populations. Although ischemia was expected in the region downstream of the stenotic region, the PAD subject showed increased perfusion to the affected limb, suggesting that collateral vessels may have compensated for the stenotic region (figure 4.14B). Since the sensitivity of total-body PET to the presence of ischemia outside the myocardium could not be assessed with this subject, additional subjects are needed to assess low perfusion values that may be present in non-myocardial ischemia that may present in the limbs or other organs.

6.4. Permutations over combinations of acquisition-related variables

While chapters 3 and 4 assess the impact of the reconstruction protocol and framing on parameter estimates, additional variables can be considered to broaden the applicability of quantitative modeling across clinical scenarios. One important optimization challenge, for pediatric studies in particular, is the determination of the lower limit for injected dose, which will impact image quality and ultimately kinetic parameter estimates. Thus, similar methods to those discussed in this dissertation can be used to assess the impact of lower dose on estimates of perfusion, either through subsampling of the events prior to image reconstruction, or through higher temporal resolution to increase the noise levels. Also, as discussed above, finer sampling of the acquisition times, and

further evaluation of temporal and spatial resolution extremes could be tested to better account for tissues that were challenging to fit in this work (e.g., lung).

6.5. Dual tracer studies

As discussed above, baseline values of a number of kinetic parameters were established in this work, including FDG K_1, FDG K_i, and [^{11}C]-butanol K_1 (tables 3.2 and 4.8). With an understanding of these parameters and the methods developed in chapters 2 through 4, dual tracer studies (Kadrmas & Hoffman, 2013; Roth et al., 2022; Vraka et al., 2022), where two boluses of radiotracer are delivered during a single acquisition, can be performed. The delivery of the second bolus occurs after a sufficient amount of time has passed, such that TACs from the first bolus can be fit to a compartment model with confidence while still leaving enough time for the second bolus to be distributed throughout the body for a second round of modeling. Thus, sensitivity and identifiability methods used here, in addition to determining the optimal time between injections, careful temporal framing for the reconstruction of the dynamic acquisition, and consideration of differential injected activity levels, can be used to design a reasonable imaging protocol prior to performing an initial dual injection study.

A dual tracer study with [^{11}C]-butanol for the first bolus, followed later by a bolus of FDG, would allow for imaging of perfusion ([^{11}C]-butanol K_1) in addition to glucose transport (FDG K_1) and metabolism (K_i or SUV). As discussed in section 1.9, perfusion-metabolism mismatches can occur, particularly in ischemic regions of the myocardium (Marshall et al., 1983; Yamagishi et al., 1999, 2000). Myocardial viability studies are performed to identify regions with this mismatch, since revascularization may improve myocardial function.

Mismatches between perfusion and metabolism have also been observed in tumor lesions (Dewhirst & Secomb, 2017; Krogh, 1919). Since delivery to the tissue is a major factor in the

success of chemotherapy (Gray et al., 1953; Rankin & Giaccia, 2008; Shannon et al., 2003) and radiotherapy (Busk et al., 2020; Harada, 2011; Moeller et al., 2004), dual tracer studies may aid in treatment planning as well as assessment of treatment response. Although tumor lesions were only characterized with FDG in this work, quantitative assessment of cancerous lesions using [^{11}C]-butanol is feasible with the methods developed in chapters 2 through 4.

One potential limiting factor of a dual tracer study is the need to separate the two injections by a sufficient length of time. Since dynamic FDG studies are typically long (e.g., 60 minutes) to allow for better estimation of the kinetic parameters, it may not be a suitable tracer to pair with [^{11}C]-butanol, as it would lead to long scan durations. However, with a dual tracer total-body PET study of FDG and [^{11}C]-butanol, the tissue-specific extraction of FDG can be evaluated through the comparison of FDG-based K_1 and [^{11}C]-butanol-based K_1 in various organs throughout the body for use of FDG-based K_1 as a measure of perfusion. Another attractive alternative is [^{11}C]-acetate, a tracer that has been used to investigate myocardial aerobic metabolism and perfusion, and scan times of 30 minutes can be utilized (Akinboboye & Bergmann, 2000). However, since this tracer also results in the formation of [^{11}C]-CO_2, metabolite correction of the plasma curve may be necessary.

Appendix: Supplemental data for chapter 3

Supplemental table A.1: Initialization parameters for non-linear least squares fitting

Parameter	v_b (mL/mL)	K_1 (mL/min/mL)	k_2 (min^{-1})	k_3 (min^{-1})	k_4 (min^{-1})	Delay (s)
Initial value	0.01	0.01	0.01	0.01	-	0
Upper bound	1.0	5.0	5.0	1.0	-	50
Lower bound	0.0001	0.0	0.0	0.0	-	0

Supplemental table A.2: Absolute bias (s.d.) in seconds of LE and CFD delay estimates for 2- and 10-second frame lengths

	LE								CFD							
Noise Level	0.03		0.1		0.2		0.3		0.03		0.1		0.2		0.3	
Threshold/ Attenuation fraction	**LE, 2 s frames**								**CFD, 2 s frames**							
2.5%	1.49	(0.38)	1.54	(0.39)	1.61	(0.63)	5.93	(9.99)	5.24	(13.14)	13.71	(19.38)	22.28	(20.22)	27.97	(18.52)
5%	1.23	(0.33)	1.25	(0.34)	1.29	(0.35)	1.33	(0.37)	0.74	(2.85)	5.63	(13.71)	11.75	(18.46)	16.62	(19.99)
10%	0.88	(0.24)	0.89	(0.25)	0.91	(0.27)	0.93	(0.29)	0.62	(0.41)	0.64	(0.98)	2.43	(8.30)	5.53	(13.29)
15%	0.61	(0.21)	0.62	(0.22)	0.63	(0.23)	0.64	(0.26)	0.67	(0.46)	0.69	(0.47)	0.71	(0.82)	1.19	(4.31)
20%	0.39	(0.17)	0.40	(0.18)	0.40	(0.20)	0.41	(0.22)	0.80	(0.53)	0.79	(0.52)	0.79	(0.52)	0.79	(0.72)
25%	0.20	(0.13)	0.21	(0.14)	0.22	(0.15)	0.24	(0.17)	0.87	(0.55)	0.87	(0.55)	0.87	(0.55)	0.86	(0.55)
30%	**0.11**	**(0.05)**	**0.11**	**(0.07)**	**0.14**	**(0.10)**	**0.18**	**(0.13)**	0.94	(0.56)	0.93	(0.56)	0.93	(0.56)	0.93	(0.57)
40%	0.32	(0.09)	0.32	(0.12)	0.34	(0.17)	0.35	(0.21)	1.00	(0.56)	1.04	(0.57)	1.06	(0.58)	1.07	(0.59)
50%	0.63	(0.09)	0.63	(0.12)	0.65	(0.19)	0.67	(0.25)	1.18	(0.58)	1.18	(0.58)	1.20	(0.60)	1.20	(0.61)
Threshold/ Attenuation fraction	**LE, 10 s frames**								**CFD, 10 s frames**							
2.5%	8.46	(2.34)	8.64	(2.39)	8.95	(2.65)	15.13	(11.40)	4.27	(7.53)	7.36	(11.87)	14.44	(16.73)	20.69	(17.57)
5%	7.70	(2.22)	7.81	(2.25)	7.99	(2.28)	8.20	(2.32)	2.73	(1.59)	5.16	(9.26)	6.65	(11.03)	10.10	(14.31)
10%	6.65	(2.04)	6.74	(2.06)	6.86	(2.08)	6.99	(2.10)	2.78	(1.66)	2.78	(1.67)	4.08	(6.63)	5.02	(8.36)
15%	5.84	(1.94)	5.91	(1.96)	6.00	(1.99)	6.09	(2.00)	2.94	(1.86)	2.95	(1.86)	2.94	(1.86)	3.06	(2.59)
20%	5.14	(1.82)	5.20	(1.84)	5.28	(1.86)	5.35	(1.88)	3.01	(1.94)	3.01	(1.94)	3.01	(1.93)	3.01	(1.93)
25%	4.47	(1.71)	4.52	(1.73)	4.59	(1.75)	4.65	(1.77)	3.05	(1.98)	3.06	(1.98)	3.06	(1.98)	3.06	(1.98)
30%	3.80	(1.64)	3.85	(1.65)	3.91	(1.67)	3.96	(1.69)	3.10	(2.02)	3.10	(2.02)	3.09	(2.01)	3.09	(2.01)
40%	2.50	(1.59)	2.54	(1.60)	2.59	(1.62)	2.63	(1.63)	3.10	(2.02)	3.10	(2.02)	3.10	(2.02)	3.12	(2.04)
50%	1.58	(1.30)	1.61	(1.31)	1.64	(1.33)	1.66	(1.34)	3.21	(2.12)	3.18	(2.10)	3.21	(2.12)	3.25	(2.15)

Supplemental table A.3: Absolute bias (s.d.) of delay estimates (s) across different LE thresholds, framing protocols, noise levels

Noise Level (Sc)	0.03		0.1		0.2		0.3	
Framing (s)				**5% LE**				
0.1 (Native)	0.03	(0.01)	0.03	(0.02)	1.83	(6.89)	11.06	(15.0)
1	0.54	(0.14)	0.55	(0.15)	0.56	(0.17)	0.58	(0.27)
2	1.23	(0.33)	1.25	(0.34)	1.29	(0.35)	1.33	(0.37)
5	3.58	(0.85)	3.64	(0.86)	3.73	(0.90)	3.82	(0.94)
10	7.70	(2.22)	7.81	(2.25)	7.99	(2.28)	8.20	(2.32)
				10% LE				
0.1 (Native)	0.01	(0.01)	0.03	(0.03)	0.06	(0.06)	0.08	(0.09)
1	0.32	(0.10)	0.32	(0.11)	0.32	(0.13)	0.32	(0.16)
2	0.88	(0.24)	0.89	(0.25)	0.91	(0.27)	0.93	(0.29)
5	2.88	(0.72)	2.92	(0.74)	2.97	(0.76)	3.04	(0.78)
10	6.65	(2.04)	6.74	(2.06)	6.86	(2.08)	6.99	(2.10)
				20% LE				
0.1 (Native)	0.08	(0.02)	0.13	(0.07)	0.18	(0.12)	0.21	(0.15)
1	0.06	(0.04)	0.06	(0.05)	0.09	(0.07)	0.12	(0.09)
2	0.39	(0.17)	0.40	(0.18)	0.40	(0.20)	0.41	(0.22)
5	1.89	(0.65)	1.92	(0.66)	1.95	(0.67)	2.00	(0.69)
10	5.14	(1.82)	5.20	(1.84)	5.28	(1.86)	5.35	(1.88)
				25% LE				
0.1 (Native)	0.14	(0.03)	0.21	(0.09)	0.26	(0.15)	0.30	(0.19)
1	0.09	(0.05)	0.10	(0.06)	0.14	(0.09)	0.16	(0.13)
2	0.20	(0.13)	0.21	(0.14)	0.22	(0.15)	0.24	(0.17)
5	1.51	(0.64)	1.53	(0.64)	1.56	(0.65)	1.60	(0.67)
10	4.47	(1.71)	4.52	(1.73)	4.59	(1.75)	4.65	(1.77)
				30% LE				
0.1 (Native)	0.22	(0.04)	0.30	(0.11)	0.36	(0.18)	0.40	(0.22)
1	0.19	(0.05)	0.21	(0.07)	0.24	(0.12)	0.26	(0.16)
2	0.11	(0.05)	0.11	(0.07)	0.14	(0.10)	0.18	(0.13)
5	1.16	(0.61)	1.18	(0.61)	1.21	(0.63)	1.23	(0.64)
10	3.80	(1.64)	3.85	(1.65)	3.91	(1.67)	3.96	(1.69)
				40% LE				
0.1 (Native)	0.40	(0.05)	0.50	(0.14)	0.58	(0.24)	0.64	(0.30)
1	0.40	(0.04)	0.42	(0.07)	0.46	(0.14)	0.50	(0.21)
2	0.32	(0.09)	0.32	(0.12)	0.34	(0.17)	0.35	(0.21)
5	0.64	(0.40)	0.65	(0.42)	0.66	(0.45)	0.67	(0.48)
10	2.50	(1.59)	2.54	(1.60)	2.59	(1.62)	2.63	(1.63)
				50% LE				
0.1 (Native)	0.61	(0.06)	0.74	(0.18)	0.85	(0.31)	0.93	(0.40)
1	0.61	(0.05)	0.63	(0.09)	0.69	(0.17)	0.75	(0.27)
2	0.63	(0.09)	0.64	(0.12)	0.65	(0.19)	0.67	(0.25)
5	0.50	(0.30)	0.51	(0.30)	0.52	(0.30)	0.54	(0.32)
10	1.58	(1.30)	1.61	(1.32)	1.64	(1.33)	1.67	(1.35)

Supplemental table A.4: Impact of delay correction on mean parametric Patlak K_i (mL/min/100 mL) for representative GUC patient

Tissue	JE	LE	No delay correction
Grey matter	1.253	1.250	1.249
Liver	0.118	0.116	0.113
Lung	0.094	0.094	0.094
Muscle	0.051	0.050	0.049
Myocardium	0.252	0.252	0.252
Spleen	0.302	0.302	0.301
L1	0.300	0.300	0.299
L2	0.187	0.187	0.186
L3	0.309	0.308	0.306
L4	0.214	0.213	0.211
L5	0.270	0.269	0.268
L6	0.317	0.316	0.316
L7	0.130	0.129	0.128
L8	0.277	0.277	0.276

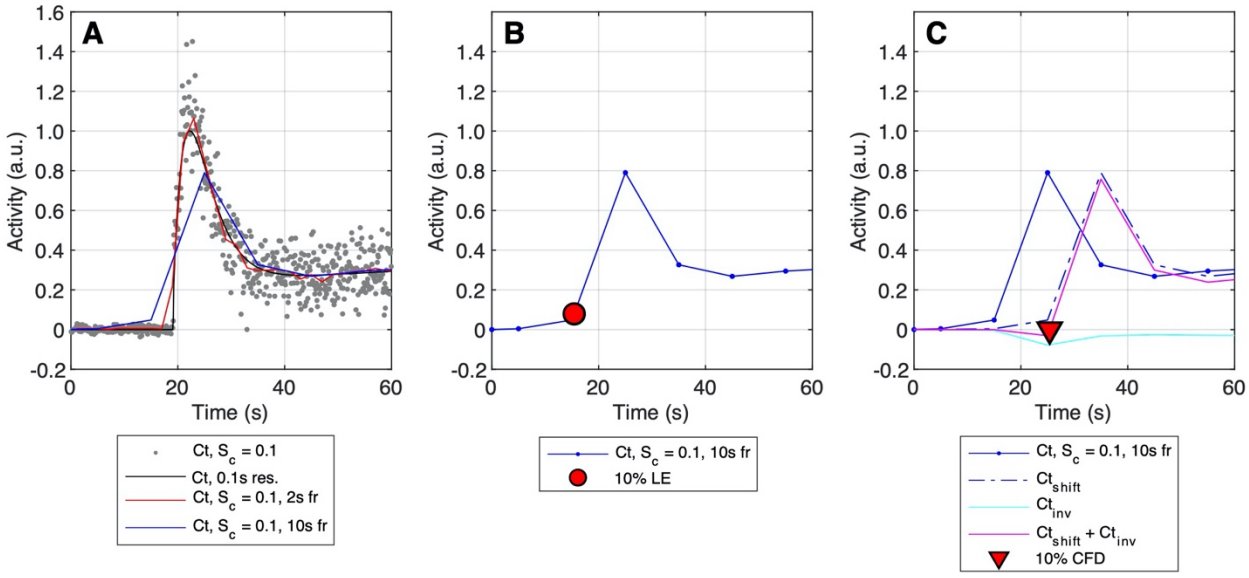

Supplemental figure A.1: Time activity curves for simulations, example LE and CFD delay estimates

Supplemental figure A.1: Time activity curves (TACs) for simulations (A), example LE (B) and CFD (C) delay estimates. In the left panel, a delay of 19.2 seconds was used to shift the IF and generate the ground truth TAC (—). In this example noisy realization (∘), the scaling factor of the standard deviation S_c is equal to 0.1. The TACs were then re-binned to reflect different frame lengths. Shown here are 2 (—) and 10 (—) second frames, with example LE (B, ●) and CFD (C, ▼) delay estimates for the 10-second frames. For the LE delay estimation in (B), a 10% LE trigger threshold was selected to mark the time at which the signal amplitude passes the trigger value, which is recorded as the arrival time. For the CFD method in (C), the following three steps were performed: (i) TACs were shifted in time by 2 seconds for shorter framing, or 1 frame when the frame length was greater than 2 seconds (C, Ct_{shift}). (ii) Attenuated and inverted versions of the TAC (attenuated to between 2.5 and 50% of the peak activity) (C, Ct_{inv}) were added to the shifted TAC. (iii) The zero-crossing point, or the timepoint at which the TAC sign changes from negative to positive marks the arrival time (C, ▼).

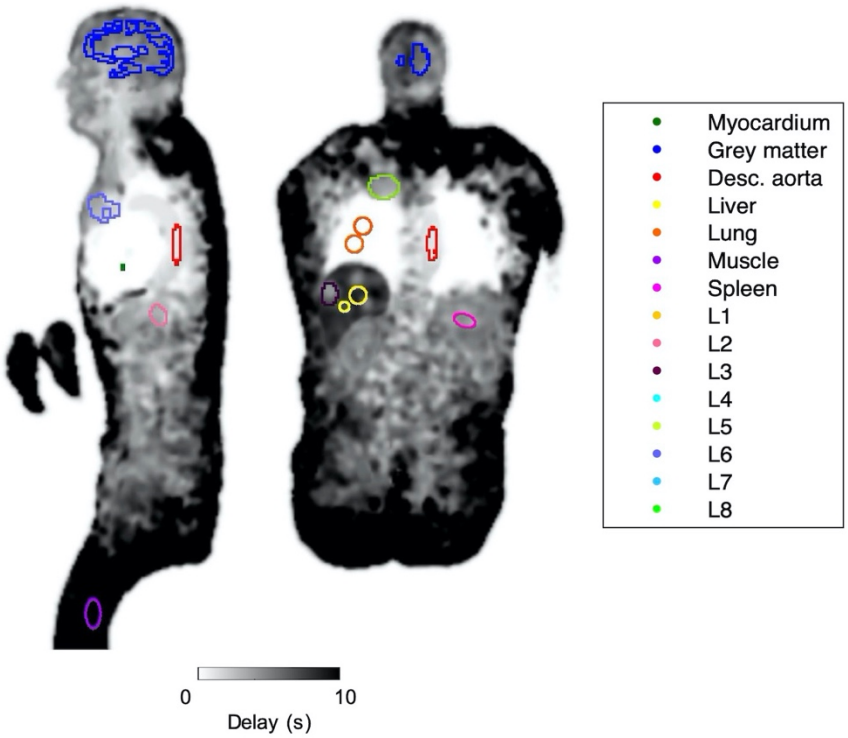

Supplemental figure A.2: Cross sectional delay maps

Supplemental figure A.2: Cross sectional delay maps with overlay of regions of interest (ROIs) from a number of GUC patient tissues selected for parametric kinetic analysis. As noted in the text, an additional vascular ROI was delineated in order to assess the impact of delay correction within the blood pool. The descending aorta, as shown above, reflects a positive delay value with respect to the left ventricle.

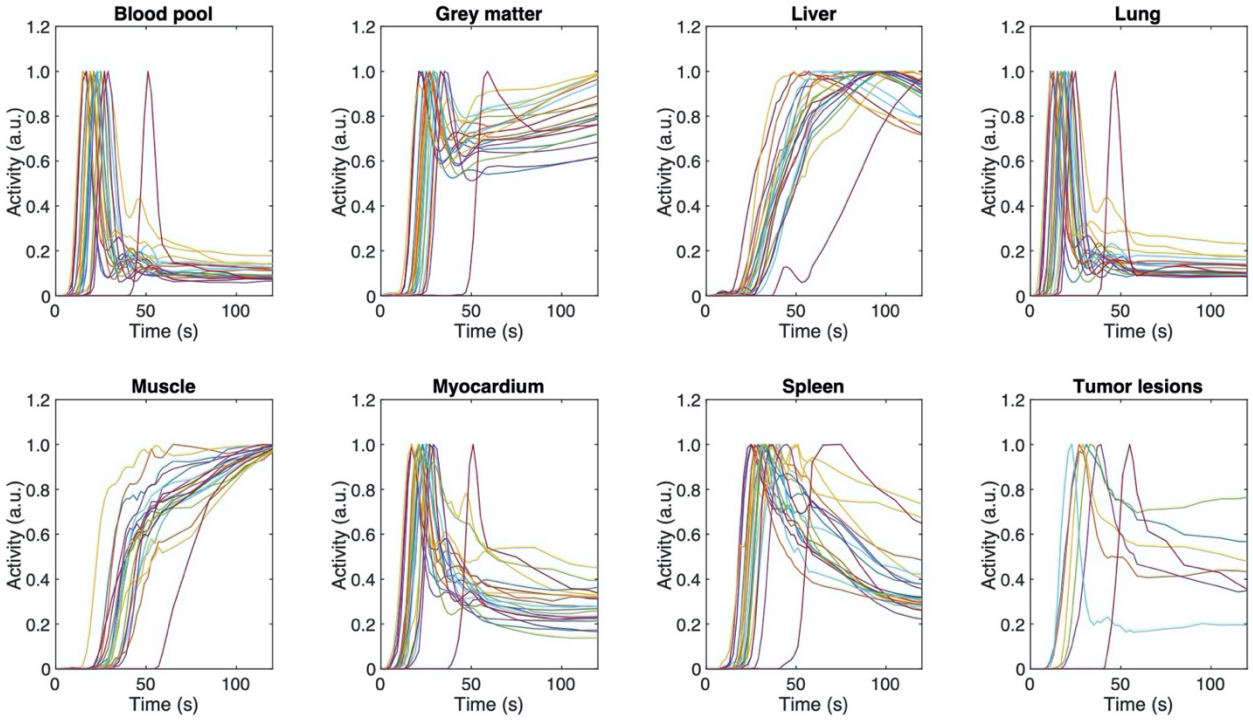

Supplemental figure A.3: TACs in a number of healthy subject and GUC patient tissues

Supplemental figure A.3: TACs in a number of healthy subject and GUC patient tissues. As noted in the caption for figure 3.1, a single lesion is shown per GUC patient for ease of visualization.

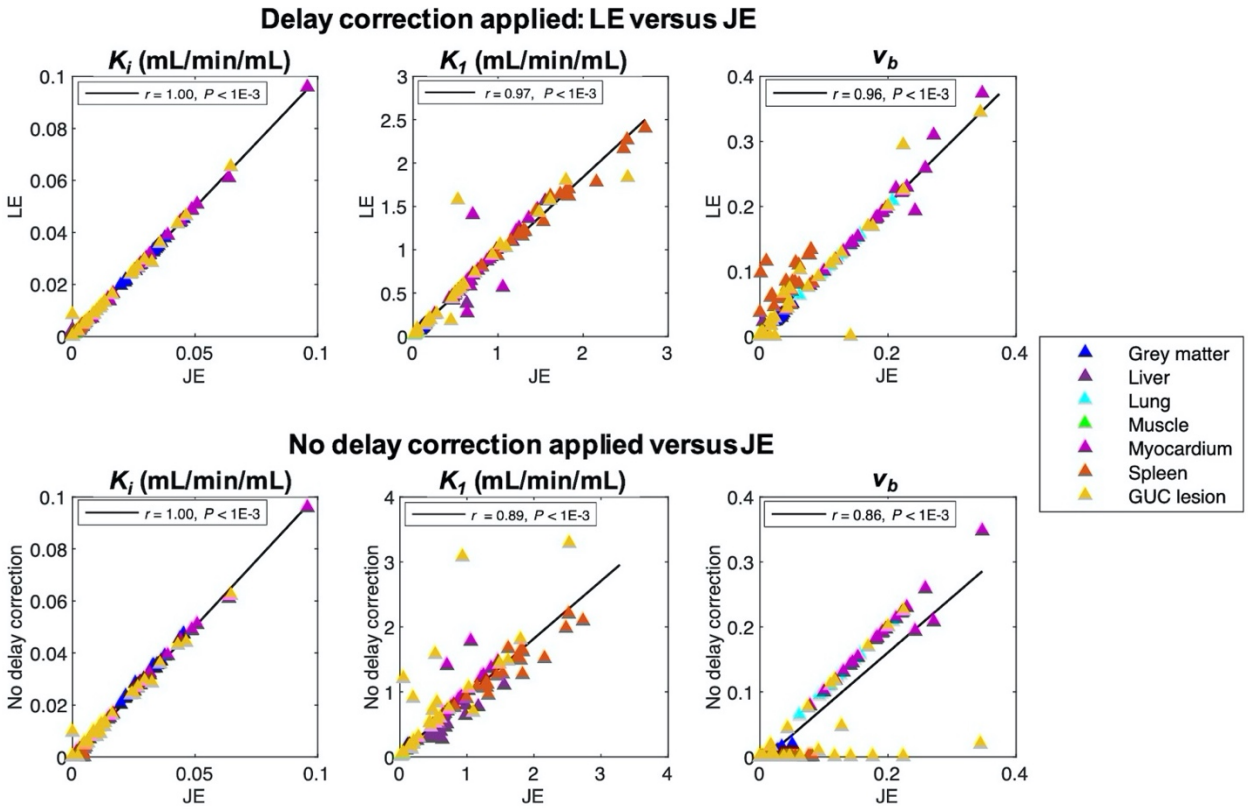

Supplemental figure A.4: Parameter estimates as compared to JE

Supplemental figure A.4: Parameter estimates as compared to JE. Linear fits were performed on pooled ROI-based results. *Top:* LE estimates for K_i (r=1.00, p<0.001, slope: 0.99), K_1 (r=0.97, p<0.001, slope: 0.91), and v_b (r=0.96, p<0.001, slope: 0.98), were in strong agreement with JE. *Bottom:* Without delay correction, K_i results were not affected (r=1.00, p<0.001, slope: 1.02). However, estimates for K_1 (r = 0.89, p<0.001, slope: 0.89) and v_b (r=0.86, p<0.001, slope: 0.85) were poorer in some tissues when delay correction was not applied, notably in the spleen and GUC lesions.

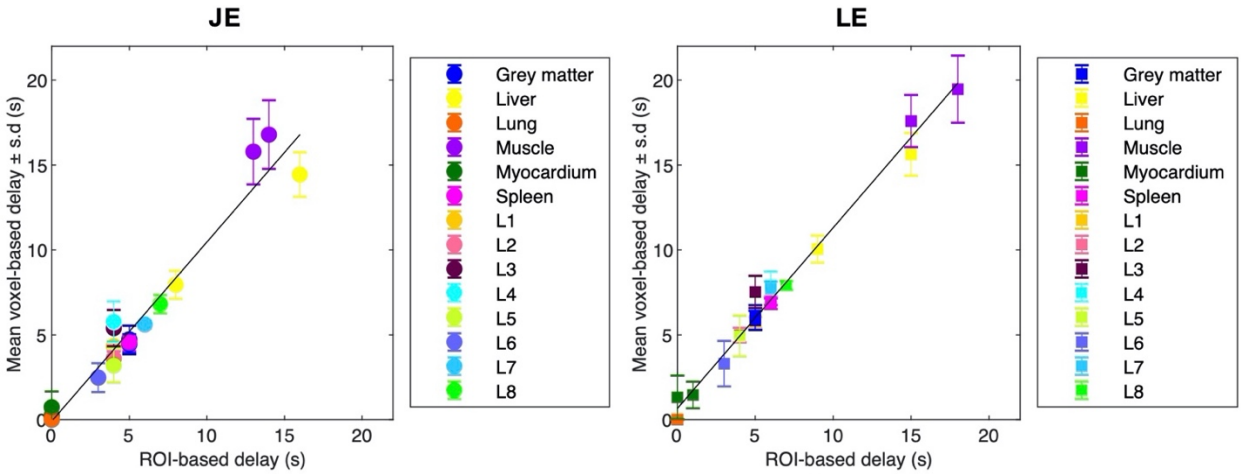

Supplemental figure A.5: Average parametric delay estimates versus ROI-based estimates

Supplemental figure A.5: Average parametric delay estimates as compared to ROI-based estimates. *Left:* JE estimates for delay (r=0.97, p<0.001, slope: 1.05), were in strong agreement with ROI-based TAC results. *Right:* LE estimates for delay (r=0.99, p<0.001, slope: 1.06) were also in strong agreement with ROI-based TAC results. To generate this figure, parametric delay values were averaged across all voxels per tissue. Delay estimates for both representative subjects were included.

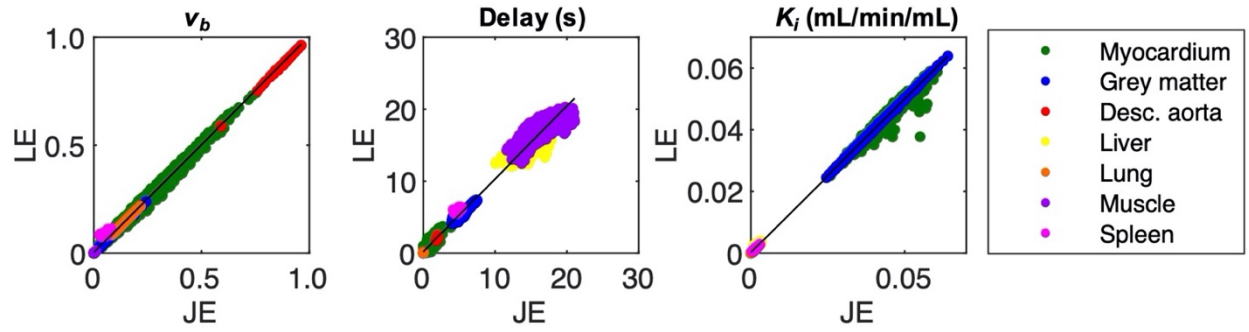

Supplemental figure A.6: Parametric LE versus JE results: representative healthy subject

Supplemental figure A.6: Parametric LE versus JE results for a representative healthy subject. LE delay was in agreement with JE results (r=0.99, p<0.001, slope: 1.01), but demonstrated a spread of delay values in the liver and muscle for both methods. LE estimates of v_b (r=1.00, p<0.001, slope: 1.00) and K_i (r=1.00, p<0.001, slope: 0.99) were in agreement with JE results.

References

Ackerman, R. H., Correia, J. A., Alpert, N. M., Baron, J. C., Gouliamos, A., Grotta, J. C., Brownell, G. L., & Taveras, J. M. (1981). Positron imaging in ischemic stroke disease using compounds labeled with oxygen 15: initial results of clinicophysiologic correlations. *Archives of Neurology*, *38*(9), 537–543. https://doi.org/10.1001/archneur.1981.00510090031002

Akinboboye, O., & Bergmann, S. R. (2000). Use of carbon 11-acetate for the measurement of myocardial oxygen consumption. *Journal of Nuclear Cardiology*, *7*(3), 282–285. https://doi.org/10.1016/S1071-3581(00)70019-5

Allman, K. C. (2013). Noninvasive assessment myocardial viability: Current status and future directions. *Journal of Nuclear Cardiology*, *20*(4), 618–637. https://doi.org/10.1007/S12350-013-9737-8

Alpert, N. M., Rabito, C. A., Correia, D. J. A., Babich, J. W., Littman, B. H., Tompkins, R. G., Rubin, N. T., Rubin, R. H., & Fischman, A. J. (2002). Mapping of local renal blood flow with PET and H215O. *Journal of Nuclear Medicine*, *43*(4), 470–475.

Ametamey, S. M., Honer, M., & Schubiger, P. A. (2008). Molecular imaging with PET. In *Chemical Reviews* (Vol. 108, Issue 5, pp. 1501–1516). American Chemical Society. https://doi.org/10.1021/cr0782426

Bachmann, P., Zhang, X., Larra, M. F., Rebeck, D., Schönbein, K., Koch, K. P., & Schächinger, H. (2018). Validation of an automated bilateral feet cold pressor test. *International Journal of Psychophysiology*, *124*, 62–70. https://doi.org/10.1016/j.ijpsycho.2017.10.013

Badawi, R. D., Shi, H., Hu, P., Chen, S., Xu, T., Price, P. M., Ding, Y., Spencer, B. A., Nardo, L., Liu, W., Bao, J., Jones, T., Li, H., & Cherry, S. R. (2019). First human imaging studies with the EXPLORER total-body pet scanner*. *Journal of Nuclear Medicine*, *60*(3), 299–303. https://doi.org/10.2967/JNUMED.119.226498

Bangash, M. N., Kong, M. L., & Pearse, R. M. (2012). Use of inotropes and vasopressor agents in critically ill patients. *British Journal of Pharmacology*, *165*(7), 2015–2033. https://doi.org/10.1111/j.1476-5381.2011.01588.x

Baron, J. C., & Jones, T. (2012). Oxygen metabolism, oxygen extraction and positron emission tomography: Historical perspective and impact on basic and clinical neuroscience. In *NeuroImage* (Vol. 61, Issue 2, pp. 492–504). Academic Press. https://doi.org/10.1016/j.neuroimage.2011.12.036

Baron, J. C., Lebrun-Grandie, P., Collard, P., Crouzel, C., Mestelan, G., & Bousser, M. G. (1982). Noninvasive measurement of blood flow, oxygen consumption, and glucose utilization in the same brain regions in man by positron emission tomography: Concise communication. *Journal of Nuclear Medicine*, *23*(5), 391–399.

Baron, J. C., Rougemont, D., Soussaline, F., Bustany, P., Crouzel, C., Bousser, M. G., & Comar, D. (1984). Local interrelationships of cerebral oxygen consumption and glucose utilization in normal subjects and in ischemic stroke patients: A positron tomography study. *Journal of Cerebral Blood Flow and Metabolism*, *4*(2), 140–149. https://doi.org/10.1038/jcbfm.1984.22

Belletti, A., Landoni, G., Lomivorotov, V. V., Oriani, A., & Ajello, S. (2020). Adrenergic downregulation in critical care: molecular mechanisms and therapeutic evidence. In *Journal of Cardiothoracic and Vascular Anesthesia* (Vol. 34, Issue 4, pp. 1023–1041). W.B. Saunders. https://doi.org/10.1053/j.jvca.2019.10.017

Berg, E., Zhang, X., Bec, J., Judenhofer, M. S., Patel, B., Peng, Q., Kapusta, M., Schmand, M., Casey, M. E., Tarantal, A. F., Qi, J., Badawi, R. D., & Cherry, S. R. (2018). Development and evaluation of mini-EXPLORER: a long axial field-of-view pet scanner for nonhuman primate imaging. *Journal of Nuclear Medicine*, *59*(6), 993–998. https://doi.org/10.2967/jnumed.117.200519

Berridge, M. S., Adler, L. P., Nelson, A. D., Cassidy, E. H., Muzic, R. F., Bednarczyk, E. M., & Miraldi, F. (1991). Measurement of human cerebral blood flow with [^{15}O]butanol and positron emission tomography. *Journal of Cerebral Blood Flow and Metabolism*, *11*(5), 707–715. https://doi.org/10.1038/jcbfm.1991.127

Billett, H. H. (1967). Hemoglobin and hematocrit. *Anesthesiology*, *28*(4), 763–763. https://doi.org/10.1097/00000542-196707000-00028

Boellaard, R., Delgado-Bolton, R., Oyen, W. J. G., Giammarile, F., Tatsch, K., Eschner, W., Verzijlbergen, F. J., Barrington, S. F., Pike, L. C., Weber, W. A., Stroobants, S., Delbeke, D., Donohoe, K. J., Holbrook, S., Graham, M. M., Testanera, G., Hoekstra, O. S., Zijlstra, J., Visser, E., … Krause, B. J. (2015). FDG PET/CT: EANM procedure guidelines for tumour imaging: version 2.0. In *European Journal of Nuclear Medicine and Molecular Imaging* (Vol. 42, Issue 2, pp. 328–354). Springer. https://doi.org/10.1007/s00259-014-2961-x

Boellaard, R., Van Lingen, A., & Lammertsma, A. A. (2001). Experimental and clinical evaluation of iterative reconstruction (OSEM) in dynamic PET: Quantitative characteristics and effects on kinetic modeling. *Journal of Nuclear Medicine*, *42*(5), 808–817.

Bohm, C., Kesselberg, M., & Hovander, B. (1988). Automated blood sampling systems for positron emission tomography. *IEEE Transactions on Nuclear Science*, *35*(1), 703–707. https://doi.org/10.1109/23.12815

Brambilla, C. R., Scheins, J., Issa, A., Tellmann, L., Herzog, H., Kops, E. R., Shah, N. J., Neuner, I., & Lerche, C. W. (2021). Bias evaluation and reduction in 3D OP-OSEM reconstruction in dynamic equilibrium PET studies with ^{11}C-labeled for binding potential analysis. *PLoS ONE*, *16*(1 January). https://doi.org/10.1371/journal.pone.0245580

Brooks, D. J., Beaney, R. P., Lammertsma, A. A., Leenders, K. L., Horlock, P. L., Kensett, M. J., Marshall, J., Thomas, D. G., & Jones, T. (1984). Quantitative measurement of blood-brain barrier permeability using rubidium-82 and positron emission tomography. *Journal of Cerebral Blood Flow and Metabolism : Official Journal of the International Society of Cerebral Blood Flow and Metabolism*, *4*(4), 535–545. https://doi.org/10.1038/jcbfm.1984.78

Brosius, F. C., Liu, Y., Nguyen, N., Sun, D. Q., Bartlett, J., & Schwaiger, M. (1997). Persistent myocardial ischemia increases GLUT1 glucose transporter expression in both ischemic and non-ischemic heart regions. *Journal of Molecular and Cellular Cardiology*, *29*(6), 1675–1685. https://doi.org/10.1006/jmcc.1997.0405

Brudin, L. H., Rhodes, C. G., Valind, S. O., Wollmer, P., & Hughes, J. M. B. (1987). Regional lung density and blood volume in nonsmoking and smoking subjects measured by PET. *Journal of Applied Physiology*, *63*(4), 1324–1334. https://doi.org/10.1152/jappl.1987.63.4.1324

Burchert, W., Schellong, S., Van Den Hoff, J., Meyer, G. J., Alexander, K., & Hundeshagen, H. (1997). Oxygen-15-water PET assessment of muscular blood flow in peripheral vascular disease. *Journal of Nuclear Medicine*, *38*(1), 93–98.

Busk, M., Overgaard, J., & Horsman, M. R. (2020). Imaging of tumor hypoxia for radiotherapy: current status and future directions. *Seminars in Nuclear Medicine*, *50*(6), 562–583. https://doi.org/10.1053/J.SEMNUCLMED.2020.05.003

Carlson, G. P. (1994). In vitro esterification of fatty acids by various alcohols in rats and rabbits. *Toxicology Letters*, *70*(1), 57–61. https://doi.org/10.1016/0378-4274(94)90144-9

Chareonthaitawee, P., Beanlands, R. S., Chen, W., Dorbala, S., Miller, E. J., Murthy, V. L., Birnie, D. H., Chen, E. S., Cooper, L. T., Tung, R. H., White, E. S., Borges-Neto, S., Di Carli, M. F., Gropler, R. J., Ruddy, T. D., Schindler, T. H., Blankstein, R., Bateman, T. M., Cerqueira, M. D., … Soman, P. (2017). Joint SNMMI-ASNC expert consensus document on the role of 18F-FDG PET/CT in carDiac sarcoid detection and therapy monitoring writing group. *Journal of Nuclear Medicine*, *58*(8), 1341–1353. https://doi.org/10.2967/jnumed.117.196287

Cherry, S. R., Badawi, R. D., Karp, J. S., Moses, W. W., Price, P., & Jones, T. (2017). Total-body imaging: Transforming the role of positron emission tomography. In *Science Translational Medicine* (Vol. 9). https://doi.org/10.1126/scitranslmed.aaf6169

Cherry, S. R., Jones, T., Karp, J. S., Qi, J., Moses, W. W., & Badawi, R. D. (2018). Total-body PET: Maximizing sensitivity to create new opportunities for clinical research and patient care. *Journal of Nuclear Medicine*, *59*(1), 3–12. https://doi.org/10.2967/jnumed.116.184028

Cherry, S. R., Sorenson, J. A., & Phelps, M. E. (2012). Physics in Nuclear Medicine, 4th Edition. In *Physics in Nuclear Medicine* (4th ed.). Elsevier Inc. https://doi.org/10.1097/hp.0b013e31828a8fa1

Chin, B. B., Green, E. D., Turkington, T. G., Hawk, T. C., & Coleman, R. E. (2009). Increasing uptake time in FDG-PET: Standardized uptake values in normal tissues at 1 versus 3 h. *Molecular Imaging and Biology*, *11*(2), 118–122. https://doi.org/10.1007/s11307-008-0177-9

Chrostek, L., Jelski, W., Szmitkowski, M., & Puchalski, Z. (2003). Gender-related differences in hepatic activity of alcohol dehydrogenase isoenzymes and aldehyde dehydrogenase in humans. *Journal of Clinical Laboratory Analysis*, *17*(3), 93–96. https://doi.org/10.1002/JCLA.10076

Cori, C. F., & Cori, G. T. (1925). The carbohydrate metabolism of tumors: II. Changes in the sugar, lactic acid, and CO_2-combining power of blood passing through a tumor. *Journal of Biological Chemistry*, *65*(2), 397–405. https://doi.org/10.1016/S0021-9258(18)84849-9

Crone, C. (1963). The permeability of capillaries in various organs as determined by use of the 'indicator diffusion' method. *Acta Physiologica Scandinavica*, *58*(4), 292–305. https://doi.org/10.1111/j.1748-1716.1963.tb02652.x

Delrue, L., Blanckaert, P., Mertens, D., van Meerbeeck, S., Ceelen, W., & Duyck, P. (2012). Tissue perfusion in pathologies of the pancreas: Assessment using 128-slice computed tomography. *Abdominal Imaging*, *37*(4), 595–601. https://doi.org/10.1007/s00261-011-9783-0

Depairon, M., & Zicot, M. (1996). The quantitation of blood flow/metabolism coupling at rest and after exercise in peripheral arterial insufficiency, using PET and ^{15}O-labeled tracers. *Angiology*, *47*(10), 991–999. https://doi.org/10.1177/000331979604701008

Dewhirst, M. W., & Secomb, T. W. (2017). Transport of drugs from blood vessels to tumour tissue. *Nature Reviews Cancer*, *17*(12), 738–750. https://doi.org/10.1038/nrc.2017.93

Di Piero, V., Ferracuti, S., Sabatini, U., Pantano, P., Cruccu, G., & Lenzi, G. L. (1994). A cerebral blood flow study on tonic pain activation in man. *Pain*, *56*(2), 167–173. https://doi.org/10.1016/0304-3959(94)90091-4

DiVincenzo, G. D., & Hamilton, M. L. (1979). Fate of n-butanol in rats after oral administration and its uptake by dogs after inhalation or skin application. *Toxicology and Applied Pharmacology*, *48*(2), 317–325. https://doi.org/10.1016/0041-008X(79)90038-3

Dvorak, H. F., Nagy, J. A., Dvorak, J. T., & Dvorak, A. M. (1988). Identification and characterization of the blood vessels of solid tumors that are leaky to circulating macromolecules. *The American Journal of Pathology*, *133*(1), 95.

Efthimiou, N. (2020). New challenges for PET image reconstruction for total-body imaging. In *PET Clinics* (Vol. 15, Issue 4, pp. 453–461). Elsevier. https://doi.org/10.1016/j.cpet.2020.06.002

Everett, B. A., Oquendo, M. A., Abi-Dargham, A., Nobler, M. S., Devanand, D. P., Lisanby, S. H., Mann, J. J., & Parsey, R. V. (2009). Safety of radial arterial catheterization in PET research subjects. In *Journal of Nuclear Medicine* (Vol. 50, Issue 10, p. 1742). NIH Public Access. https://doi.org/10.2967/jnumed.109.063206

Feig, S. A., Segel, G. B., Shohet, S. B., & Nathan, D. G. (1972). Energy metabolism in human erythrocytes. II. Effects of glucose depletion. *The Journal of Clinical Investigation*, *51*(6), 1547–1554. https://doi.org/10.1172/JCI106951

Feng, D., Huang, S. C., & Wang, X. (1993). Models for computer simulation studies of input functions for tracer kinetic modeling with positron emission tomography. *International Journal of Bio-Medical Computing*, *32*(2), 95–110. https://doi.org/10.1016/0020-7101(93)90049-C

Feng, D., Wong, K. P., Wu Chi-Ming, & Siu, W. C. (1997). A technique for extracting physiological parameters and the required input function simultaneously from PET image measurements: Theory and simulation study. *IEEE Transactions on Information Technology in Biomedicine*, *1*(4), 243–254. https://doi.org/10.1109/4233.681168

Feng, T., Zhao, Y., Shi, H., Li, H., Zhang, X., Wang, G., Price, P. M., Badawi, R. D., Cherry, S. R., & Jones, T. (2021). Total-body quantitative parametric imaging of early kinetics of ^{18}F-FDG. *Journal of Nuclear Medicine*, *62*(5), 738–744. https://doi.org/10.2967/jnumed.119.238113

Fletcher, J. W., Logan, T. F., Eitel, J. A., Mathias, C. J., Ng, Y., Lacy, J. L., Hutchins, G. D., & Green, M. A. (2015). Whole-body PET/CT evaluation of tumor perfusion using generator-based ^{62}Cu-ethylglyoxal bis(Thiosemicarbazonato) copper(II): Validation by direct comparison to ^{15}O-water in metastatic renal cell carcinoma. *Journal of Nuclear Medicine*, *56*(1), 56–62. https://doi.org/10.2967/jnumed.114.148106

Fowkes, F. G. R., Aboyans, V., Fowkes, F. J. I., McDermott, M. M., Sampson, U. K. A., & Criqui, M. H. (2017). Peripheral artery disease: Epidemiology and global perspectives. *Nature Reviews Cardiology*, *14*(3), 156–170. https://doi.org/10.1038/nrcardio.2016.179

Galea, N., Cundari, G., Borrazzo, C., Pambianchi, G., Bracci, A., Rosato, E., Francone, M., Carbone, I., & Catalano, C. (2019). Splenic blood flow increases after hypothermic stimulus (cold pressor test): A perfusion magnetic resonance study. *BioMed Research International*, *2019*. https://doi.org/10.1155/2019/8437927

Gallagher, B. M., Fowler, J. S., Gutterson, N. I., MacGregor, R. R., Wan, C. N., & Wolf, A. P. (1978). Metabolic trapping as a principle of radiopharmaceutical design: Some factors

responsible for the biodistribution of [^{18}F] 2-deoxy-2-fluoro-D-glucose. *Journal of Nuclear Medicine*, *19*(10), 1154–1161.

Gambhir, S. S., Schwaiger, M., Huang, S. C., Krivokapich, J., Schelbert, H. R., Nienaber, C. A., & Phelps, M. E. (1989). Simple noninvasive quantification method for measuring myocardial glucose utilization in humans employing positron emission tomography and fluorine-18 deoxyglucose. *Journal of Nuclear Medicine*, *30*(3), 359–366.

Girard, A., Saint-Jalmes, H., Chaboub, N., Le Reste, P. J., Metais, A., Devillers, A., Le Jeune, F., & Palard-Novello, X. (2020). Optimization of time frame binning for FDOPA uptake quantification in glioma. *PLoS ONE*, *15*(4). https://doi.org/10.1371/journal.pone.0232141

Gjedde, A. (1982). Calculation of cerebral glucose phosphorylation from brain uptake of glucose analogs in vivo: A re-examination. In *Brain Research Reviews* (Vol. 4, Issue 2, pp. 237–274). Brain Res. https://doi.org/10.1016/0165-0173(82)90018-2

Gjedde, A., Hansen, A. J., & Siemkowicz, E. (1980). Rapid simultaneous determination of regional blood flow and blood-brain glucose transfer in brain of rat. *Acta Physiologica Scandinavica*, *108*(4), 321–330. https://doi.org/10.1111/j.1748-1716.1980.tb06540.x

Glatting, G., Weller, R., & Reske, S. N. (1997). Determination of the Myocardial Rubidium Extraction Fraction: Theoretical Investigation. In *Radioactive Isotopes in Clinical Medicine and Research* (pp. 457–461). Birkhäuser, Basel. https://doi.org/10.1007/978-3-0348-7772-5_74

Gray, L. H., Conger, A. D., Ebert, M., Hornsey, S., & Scott, O. C. (1953). The concentration of oxygen dissolved in tissues at the time of irradiation as a factor in radiotherapy. *The British Journal of Radiology*, *26*(312), 638–648. https://doi.org/10.1259/0007-1285-26-312-638

Gunn, R. N., Gunn, S. R., & Cunningham, V. J. (2001). Positron emission tomography compartmental models. *Journal of Cerebral Blood Flow & Metabolism*, *21*(6), 635–652.

Gunn, R. N., Ranicar, A., Yap, J. T., Wells, P., Osman, S., Jones, T., & Cunningham, V. J. (2000). On-line measurement of exhaled [^{11}C]-CO_2 during PET. *Journal of Nuclear Medicine*, *41*, 605–611.

Hack, S. N., Bergmann, S. R., Eichling, J. O., & Sobel, B. E. (1983). Quantification of regional myocardial perfusion by exponential infusion of ^{11}C-butanol. *IEEE Transactions on Biomedical Engineering*, *BME-30*(11), 716–722. https://doi.org/10.1109/TBME.1983.325185

Häggström, I., Axelsson, J., Schmidtlein, C. R., Karlsson, M., Garpebring, A., Johansson, L., Sörensen, J., & Larsson, A. (2015). A Monte Carlo study of the dependence of early frame sampling on uncertainty and bias in pharmacokinetic parameters from dynamic PET. *Journal of Nuclear Medicine Technology*, *43*(1), 53–60. https://doi.org/10.2967/jnmt.114.141754

Häggström, I., Schmidtlein, C. R., Karlsson, M., & Larsson, A. (2014). Compartment modeling of dynamic brain PET - the impact of scatter corrections on parameter errors. *Medical Physics*, *41*(11). https://doi.org/10.1118/1.4897610

Harada, H. (2011). How can we overcome tumor hypoxia in radiation therapy? *Journal of Radiation Research*, *52*(5), 545–556. https://doi.org/10.1269/jrr.11056

Herscovich, P., Raichle, M., Kilbourne, M., & Welch, M. (1987). Positron emission tomographic measurements of cerebral blood flow and permeability. *Journal of Cerebral Blood Flow & Metabolism*, *7*, 527-542.

Herscovitch, P., Markham, J., & Raichle, M. E. (1983). Brain blood flow measured with intravenous $H_2{}^{15}O$. I. Theory and error analysis. *Journal of Nuclear Medicine*, *24*(9), 782–789.

Herscovitch, P., Raichle, M. E., Kilbourn, M. R., & Welch, M. J. (1987). Positron emission tomographic measurement of cerebral blood flow and permeability-surface area product of water using [^{15}O]water and [^{11}C]butanol. *Journal of Cerebral Blood Flow and Metabolism*, *7*(5), 527–542. https://doi.org/10.1038/jcbfm.1987.102

Herzog, H., Seitz, R. J., Tellmann, L., Kops, E. R., Jülicher, F., Schlaug, G., Kleinschmidt, A., & Müller-Gärtner, H. W. (1996). Quantitation of regional cerebral blood flow with ^{15}O-butanol and positron emission tomography in humans. *Journal of Cerebral Blood Flow and Metabolism*, *16*(4), 645–649. https://doi.org/10.1097/00004647-199607000-00015

Herzog, H., Seitz, R. J., Tellmann, L., Schlaug, G., Kleinschmidt, A., Nebeling, B., Stöcklin, G., & Müller-Gärtner, H. W. (1994). Pharmacokinetics and radiation dose of oxygen-15 labelled butanol in rCBF studies in humans. *European Journal of Nuclear Medicine*, *21*(2), 138–143. https://doi.org/10.1007/BF00175761

Hess, S., Blomberg, B. A., Zhu, H. J., Høilund-Carlsen, P. F., & Alavi, A. (2014). The pivotal role of FDG-PET/CT in modern medicine. *Academic Radiology*, *21*(2), 232–249. https://doi.org/10.1016/j.acra.2013.11.002

Hinz, R. (2012). *Measurement of cerebral metabolic rates of glucose CMR_{glc} with [^{18}F]FDG PET: A practical introduction with references*. https://personalpages.manchester.ac.uk/staff/Rainer.Hinz/material/popif12.html

Hinz, R., & Turkheimer, F. E. (2006). Determination of tracer arrival delay with spectral analysis. *IEEE Transactions on Nuclear Science*, *53*(1), 212–219. https://doi.org/10.1109/TNS.2005.862982

Horsager, J., Okkels, N., van den Berge, N., Jacobsen, J., Schact, A., Munk, O. L., Vang, K., Bender, D., Brooks, D. J., & Borghammer, P. (2022). In vivo vesicular acetylcholine transporter density in human peripheral organs: an [^{18}F]FEOBV PET/CT study. *EJNMMI Research*, *12*(1), 17. https://doi.org/10.1186/s13550-022-00889-9

Hove, J. D., Rasmussen, R., Freiberg, J., Holm, S., Kelbæk, H., & Kofoed, K. E. (2008). Clinical evaluation of iterative reconstruction (ordered-subset expectation maximization) in dynamic positron emission tomography: Quantitative effects on kinetic modeling with N-13 ammonia in healthy subjects. *Journal of Nuclear Cardiology*, *15*(4), 530–534. https://doi.org/10.1016/j.nuclcard.2008.02.034

Huang, S. C., Phelps, M. E., Hoffman, E. J., Sideris, K., Selin, C. J., & Kuhl, D. E. (1980). Noninvasive determination of local cerebral metabolic rate of glucose in man. *American Journal of Physiology-Endocrinology and Metabolism*, *238*(1), E69–E82. https://doi.org/10.1152/ajpendo.1980.238.1.e69

Huisman, M. C., van Golen, L. W., Hoetjes, N. J., Greuter, H. N., Schober, P., Ijzerman, R. G., Diamant, M., & Lammertsma, A. A. (2012). Cerebral blood flow and glucose metabolism in healthy volunteers measured using a high-resolution PET scanner. *EJNMMI Research*, *2*(1), 1–9. https://doi.org/10.1186/2191-219X-2-63

Iida, H., Kanno, I., Miura, S., Murakami, M., Takahashi, K., & Uemura, K. (1986). Error analysis of a quantitative cerebral blood flow measurement using $H_2{}^{15}O$ autoradiography and positron emission tomography, with respect to the dispersion of the input function. *Journal of Cerebral Blood Flow and Metabolism*, *6*(5), 536–545. https://doi.org/10.1038/jcbfm.1986.99

Iida, H., Kanno, I., Takahashi, A., Miura, S., Murakami, M., Takahashi, K., Ono, Y., Shishido, F., Inugami, A., Tomura, N., Higano, S., Fujita, H., Sasaki, H., Nakamichi, H., Mizusawa, S., Kondo, Y., & Uemura, K. (1988). Measurement of absolute myocardial blood flow with

$H_2{}^{15}O$ and dynamic positron-emission tomography. Strategy for quantification in relation to the partial-volume effect. *Circulation*, *78*(1), 104–115. https://doi.org/10.1161/01.CIR.78.1.104

Iida, H., Law, I., Pakkenberg, B., Krarup-Hansen, A., Eberl, S., Holm, S., Hansen, A. K., Gundersen, H. J. G., Thomsen, C., Svarer, C., Ring, P., Friberg, L., & Paulson, O. B. (2000). Quantitation of regional cerebral blood flow corrected for partial volume effect using O-15 water and PET: I. Theory, error analysis, and stereologic comparison. *Journal of Cerebral Blood Flow and Metabolism*, *20*(8), 1237–1251. https://doi.org/10.1097/00004647-200008000-00009

Iida, H., Rhodes, C. G., Silva, R. de, Yamamoto, Y., Araujo, L. I., Maseri, A., & Jones, T. (1991). Myocardial tissue fraction correction for partial volume effects and measure of tissue viability. *Journal of Nuclear Medicine*, *32*(11), 2169–2175.

Iida, S., Harada, Y., Ikenoue, S., & Moriya, H. (1999). Measurement of bone marrow blood volume in the knee by positron emission tomography. *Journal of Orthopaedic Science*, *4*(3), 216–222. https://doi.org/10.1007/s007760050096

Islam, M. M., Tsujikawa, T., Mori, T., Kiyono, Y., & Okazawa, H. (2017). Pixel-by-pixel precise delay correction for measurement of cerebral hemodynamic parameters in $H_2{}^{15}O$ PET study. *Annals of Nuclear Medicine*, *31*(4), 283–294. https://doi.org/10.1007/s12149-017-1156-5

Ito, H., Kanno, I., Iida, H., Hatazawa, J., Shimosegawa, E., Tamura, H., & Okudera, T. (2001). Arterial fraction of cerebral blood volume in humans measured by positron emission tomography. *Annals of Nuclear Medicine*, *15*(2), 111–116. https://doi.org/10.1007/BF02988600

Jackson, I. M., Lee, S. J., Sowa, A. R., Rodnick, M. E., Bruton, L., Clark, M., Preshlock, S., Rothley, J., Rogers, V. E., Botti, L. E., Henderson, B. D., Hockley, B. G., Torres, J., Raffel, D. M., Brooks, A. F., Frey, K. A., Kilbourn, M. R., Koeppe, R. A., Shao, X., & Scott, P. J. H. (2020). Use of 55 PET radiotracers under approval of a Radioactive Drug Research Committee (RDRC). *EJNMMI Radiopharmacy and Chemistry*, *5*(1). https://doi.org/10.1186/s41181-020-00110-z

Kadrmas, D. J., & Hoffman, J. M. (2013). Methodology for quantitative rapid multi-tracer PET tumor characterizations. *Theranostics*, *3*(10), 757–773. https://doi.org/10.7150/thno.5201

Kahn, D., Weiner, G. J., Ben-Haim, S., Ponto, L. L. B., Madsen, M. T., Bushnell, D. L., Watkins, G. L., Argenyi, E. A., & Hichwa, R. D. (1994). Positron emission tomographic measurement of bone marrow blood flow to the pelvis and lumbar vertebrae in young normal adults. *Blood*, *83*(4), 958–963. https://doi.org/10.1182/blood.v83.4.958.bloodjournal834958

Kannenkeril, D., Janka, R., Bosch, A., Jung, S., Kolwelter, J., Striepe, K., Ott, C., Martirosian, P., Schiffer, M., Uder, M., & Schmieder, R. E. (2021). Detection of Changes in Renal Blood Flow Using Arterial Spin Labeling MRI. *American Journal of Nephrology*, *52*(1), 69–75. https://doi.org/10.1159/000513665

Kaufmann, P. A., Gnecchi-Ruscone, T., Yap, J. T., Rimoldi, O., & Camici, P. G. (1999). Assessment of the reproducibility of baseline and hyperemic myocardial blood flow measurements with ^{15}O-labeled water and PET. *Journal of Nuclear Medicine*, *40*(11), 1848–1856.

Keramida, G., Gregg, S., & Peters, A. M. (2020). Stimulation of the hepatic arterial buffer response using exogenous adenosine: hepatic rest/stress perfusion imaging. *European Radiology*, *30*(11), 5852–5861. https://doi.org/10.1007/s00330-020-06984-6

Kety, S., & Schmidt, C. (1947). The nitrous oxide method for the quantitative determination of cerebral blood flow in man: theory, procedure and normal values. *Journal of Clinical Investigation*, *27*(4), 476–483.

Khan, S., Goh, V., Tam, E., Wellsted, D., & Halligan, S. (2012). Perfusion CT assessment of the colon and rectum: Feasibility of quantification of bowel wall perfusion and vascularization. *European Journal of Radiology*, *81*(5), 821–824. https://doi.org/10.1016/j.ejrad.2011.02.033

Kjaer, A., Meyer, C., Nielsen, F. S., Parving, H. H., & Hesse, B. (2003). Dipyridamole, cold pressor test, and demonstration of endothelial dysfunction: A PET study of myocardial perfusion in diabetes. *Journal of Nuclear Medicine*, *44*(1), 19–23.

Knapp, W. H., Helus, F., Oberdorfer, F., Layer, K., Sinn, H., Ostertag, H., & Matzku, S. (1985). ^{11}C-Butanol for imaging of the blood-flow distribution in tumor-bearing animals. *European Journal of Nuclear Medicine*, *10*(11–12), 540–548. https://doi.org/10.1007/BF00252749

Knoll, G. F. (2005). Radiation Detection and Measurement. In *Book* (3rd ed.). John Wiley and Sons Inc.

Komar, G., Kauhanen, S., Liukko, K., Seppänen, M., Kajander, S., Ovaska, J., Nuutila, P., & Minn, H. (2009). Decreased blood flow with increased metabolic activity: A novel sign of pancreatic tumor aggressiveness. *Clinical Cancer Research*, *15*(17), 5511–5517. https://doi.org/10.1158/1078-0432.CCR-09-0414

Krogh, A. (1919). The supply of oxygen to the tissues and the regulation of the capillary circulation. *The Journal of Physiology*, *52*(6), 457–474. https://doi.org/10.1113/jphysiol.1919.sp001844

Lammertsma, A. A. (2017). Forward to the past: The case for quantitative PET imaging. *Journal of Nuclear*, *58*(7), 1019–1024. https://doi.org/10.2967/JNUMED.116.188029

Lammertsma, A. A. (2019). Essentials of quantitative imaging with PET. In *Nuclear Medicine Textbook* (pp. 219–233). Springer International Publishing. https://doi.org/10.1007/978-3-319-95564-3_10

Lammertsma, A. A., Cunningham, V. J., Deiber, M. P., Heather, J. D., Bloomfield, P. M., Nutt, J., Frackowiak, R. S. J., & Jones, T. (1990). Combination of dynamic and integral methods for generating reproducible functional CBF images. *Journal of Cerebral Blood Flow and Metabolism*, *10*(5), 675–686. https://doi.org/10.1038/jcbfm.1990.121

Leenders, K. L., Perani, D., Lammertsma, A. A., Heather, J. D., Buckingham, P., Jones, T., Healy, M. J. R., Gibbs, J. M., Wise, R. J. S., Hatazawa, J., Herold, S., Beaney, R. P., Brooks, D. J., Spinks, T., Rhodes, C., & Frackowiak, R. S. J. (1990). Cerebral blood flow, blood volume and oxygen utilization: Normal values and effect of age. *Brain*, *113*(1), 27–47. https://doi.org/10.1093/brain/113.1.27

Leung, E. K., Berg, E., Omidvari, N., Spencer, B. A., Li, E. J., Abdelhafez, Y. G., Schmall, J. P., Liu, W., He, L., Tang, S., Liu, Y., Dong, Y., Jones, T., Cherry, S. R., & Badawi, R. D. (2021). Quantitative accuracy in total-body imaging using the uEXPLORER PET/CT scanner. *Physics in Medicine & Biology*, *66*(20), 205008. https://doi.org/10.1088/1361-6560/ac287c

Leung, E. K., Revilla, E., Spencer, B. A., Xie, Z., Zhang, X., Omidvari, N., Badawi, R. D., Cherry, S. R., Lu, Y., & Berg, E. (2021). A quantitative image reconstruction platform with integrated motion detection for total-body PET. *Journal of Nuclear Medicine*, *62*(supplement 1), 1549 LP – 1549. http://jnm.snmjournals.org/content/62/supplement_1/1549.abstract

Li, E. J., Spencer, B. A., Schmall, J. P., Abdelhafez, Y., Badawi, R. D., Wang, G., & Cherry, S. R. (2021). Efficient delay correction for total-body PET kinetic modeling using pulse timing

methods. *Journal of Nuclear Medicine*, jnumed.121.262968. https://doi.org/10.2967/jnumed.121.262968

Li, T., Zhang, M., Qi, W., Asma, E., & Qi, J. (2020). Motion correction of respiratory-gated PET images using deep learning based image registration framework. *Physics in Medicine and Biology*, *65*(15). https://doi.org/10.1088/1361-6560/ab8688

Li, T., Zhang, X., Xie, Z., Shi, H., Cherry, S., Badawi, R., & Qi, J. (2021). Total-body parametric reconstruction with deep learning-based data-driven motion compensation. In *Journal of Nuclear Medicine* (Vol. 62, Issue supplement 1, p. 60).

Liu, Y. J., Yang, H. T., Yao, M. M. S., Lin, S. C., Cho, D. Y., Shen, W. C., Juan, C. J., & Chan, W. P. (2021). Quantifying lumbar vertebral perfusion by a Tofts model on DCE-MRI using segmental versus aortic arterial input function. *Scientific Reports*, *11*(1), 1–12. https://doi.org/10.1038/s41598-021-82300-6

Lowe, A. G., & Walmsley, A. R. (1986). The kinetics of glucose transport in human red blood cells. *Biochimica et Biophysica Acta (BBA) - Biomembranes*, *857*(2), 146–154. https://doi.org/10.1016/0005-2736(86)90342-1

Lucignani, G., Paganelli, G., & Bombardieri, E. (2004). The use of standardized uptake values for assessing FDG uptake with PET in oncology: A clinical perspective. *Nuclear Medicine Communications*, *25*(7), 651–656. https://doi.org/10.1097/01.MNM.0000134329.30912.49

Macey, D. J., Chairman, L. E. W., Johnson, T. K., & Zanzonico, P. B. (2001). AAPM Report No. 71: A primer for radioimmunotherapy and radionuclide therapy. In *Association of Physicists in Medicine* (Issue 71).

Maddahi, J., & Packard, R. R. S. (2014). Cardiac PET perfusion tracers: Current status and future directions. In *Seminars in Nuclear Medicine* (Vol. 44, Issue 5, pp. 333–343). NIH Public Access. https://doi.org/10.1053/j.semnuclmed.2014.06.011

Madsen, S., Dias, A. H., Lauritsen, K. M., Bouchelouche, K., Tolbod, L. P., & Gormsen, L. C. (2020). Myocardial viability testing by positron emission tomography: Basic concepts, mini-review of the literature and experience from a tertiary pet center. *Seminars in Nuclear Medicine*, *50*(3), 248–259. https://doi.org/10.1053/J.SEMNUCLMED.2020.02.010

Manapragada, P. P., Andrikopoulou, E., Bajaj, N., & Bhambhvani, P. (2021). PET cardiac imaging (perfusion, viability, sarcoidosis, and infection). *Radiologic Clinics of North America*, *59*(5), 835–852. https://doi.org/10.1016/J.RCL.2021.05.009

Manautou, J. E., & Carlson, G. P. (1991). Ethanol-induced fatty acid ethyl ester formation in vivo and in vitro in rat lung. *Toxicology*, *70*(3), 303–312. https://doi.org/10.1016/0300-483x(91)90005-l

Manisty, C., Ripley, D. P., Herrey, A. S., Captur, G., Wong, T. C., Petersen, S. E., Plein, S., Peebles, C., Schelbert, E. B., Greenwood, J. P., & Moon, J. C. (2015). Splenic switch-off: A tool to assess stress adequacy in adenosine perfusion cardiac MR imaging. *Radiology*, *276*(3), 732–740. https://doi.org/10.1148/radiol.2015142059

Mankoff, D. A. (2007). A definition of molecular imaging. *Journal of Nuclear Medicine*, *48*(6).

Mankoff, D. A., Shields, A. F., Graham, M. M., Link, J. M., Eary, J. F., & Krohn, K. A. (1998). Kinetic analysis of 2-[carbon-11]thymidine PET imaging studies: Compartmental model and mathematical analysis. *Journal of Nuclear Medicine*, *39*(6), 1043–1055.

Manouilenko, I., Pagani, M., Stone-Elander, S., Odh, R., Brolin, F., Hatherly, R., Jacobsson, H., Larsson, S. A., & Bejerot, S. (2013). Autistic traits, ADHD symptoms, neurological soft signs and regional cerebral blood flow in adults with autism spectrum disorders. *Research in Autism Spectrum Disorders*, *7*(5), 566–578. https://doi.org/10.1016/j.rasd.2012.12.008

Marshall, R. C., Tillisch, J. H., Phelps, M. E., Huang, S. C., Carson, R., Henze, E., & Schelbert, H. R. (1983). Identification and differentiation of resting myocardial ischemia and infarction in man with positron computed tomography, ^{18}F-labeled fluorodeoxyglucose and N-13 ammonia. *Circulation*, *67*(4), 766–778. https://doi.org/10.1161/01.CIR.67.4.766

Martiat, P., Ferrant, A., Cogneau, M., Bol, A., Michel, C., Rodhain, J., Michaux, J. L., & Sokal, G. (1987). Assessment of bone marrow blood flow using positron emission tomography: no relationship with bone marrow cellularity. *British Journal of Haematology*, *66*(3), 307–310. https://doi.org/10.1111/j.1365-2141.1987.tb06914.x

Matsunaga, K., Yanagawa, M., Otsuka, T., Hirata, H., Kijima, T., Kumanogoh, A., Tomiyama, N., Shimosegawa, E., & Hatazawa, J. (2017). Quantitative pulmonary blood flow measurement using ^{15}O-H_2O PET with and without tissue fraction correction: a comparison study. *EJNMMI Research*, *7*(1), 1–9. https://doi.org/10.1186/s13550-017-0350-8

McCarty, R. (2016). The fight-or-flight response: A cornerstone of stress research. In *Stress: Concepts, Cognition, Emotion, and Behavior: Handbook of Stress* (pp. 33–37). Academic Press. https://doi.org/10.1016/B978-0-12-800951-2.00004-2

Meyer, E. (1989). Simultaneous correction for tracer arrival delay and dispersion in CBF measurements by the $H_2{}^{15}O$ autoradiographic method and dynamic PET. *Journal of Nuclear Medicine*, *30*(6), 1069–1078.

Micieli, G., Tassorelli, C., Bosone, D., Cavallini, A., Viotti, E., & Nappi, G. (1994). Intracerebral vascular changes induced by cold pressor test: A model of sympathetic activation. *Neurological Research*, *16*(3), 163–167. https://doi.org/10.1080/01616412.1994.11740219

Miles, K. A., & Williams, R. E. (2008). Warburg revisited: Imaging tumour blood flow and metabolism. *Cancer Imaging*, *8*(1), 81–86. https://doi.org/10.1102/1470-7330.2008.0011

Moeller, B. J., Cao, Y., Li, C. Y., & Dewhirst, M. W. (2004). Radiation activates HIF-1 to regulate vascular radiosensitivity in tumors: Role of reoxygenation, free radicals, and stress granules. *Cancer Cell*, *5*(5), 429–441. https://doi.org/10.1016/S1535-6108(04)00115-1

Morris, E. D., Endres, C. J., Schmidt, K. C., Christian, B. T., Muzic Jr., R. F., & Fisher, R. E. (2004). Kinetic modeling in positron emission tomography. In M. N. Wernick & J. N. Aarsvold (Eds.), *Emission tomography: The fundamentals of PET and SPECT* (1st ed., Vol. 46, Issue 1, pp. 499–540). Elsevier. https://doi.org/10.1016/B978-012744482-6.50026-0

Murthy, V. L., Bateman, T. M., Beanlands, R. S., Berman, D. S., Borges-Neto, S., Chareonthaitawee, P., Cerqueira, M. D., DeKemp, R. A., DePuey, E. G., Dilsizian, V., Dorbala, S., Ficaro, E. P., Garcia, E. v., Gewirtz, H., Heller, G. v., Lewin, H. C., Malhotra, S., Mann, A., Ruddy, T. D., … Corbett, J. R. (2018). Clinical quantification of myocardial blood flow using PET: Joint position paper of the SNMMI Cardiovascular Council and the ASNC. *Journal of Nuclear Cardiology*, *25*(1), 269–297. https://doi.org/10.1007/s12350-017-1110-x

Muzi, M., Mankoff, D. A., Grierson, J. R., Wells, J. M., Vesselle, H., & Krohn, K. A. (2005). Kinetic modeling of 3′-deoxy-3′-fluorothymidine in somatic tumors: Mathematical studies. *Journal of Nuclear Medicine*, *46*(2), 371–380.

Naganawa, M., Gallezot, J. D., Shah, V., Mulnix, T., Young, C., Dias, M., Chen, M. K., Smith, A. M., & Carson, R. E. (2020). Assessment of population-based input functions for Patlak imaging of whole body dynamic ^{18}F-FDG PET. *EJNMMI Physics*, *7*(1). https://doi.org/10.1186/s40658-020-00330-x

Nordberg, A., Lundqvist, H., Hartvig, P., Lilja, A., & Langstrom, B. (1995). Kinetic analysis of regional (S)(-)^{11}C-nicotine binding in normal and Alzheimer brains - In vivo assessment

using positron emission tomography. In *Alzheimer Disease and Associated Disorders* (Vol. 9, Issue 1, pp. 21–27). https://doi.org/10.1097/00002093-199505000-00006

Nuutila, P., Raitakari, M., Laine, H., Kirvelä, O., Takala, T., Utriainen, T., Mäkimattila, S., Pitkänen, O. P., Ruotsalainen, U., Iida, H., Knuuti, J., & Yki-Järvinen, H. (1996). Role of blood flow in regulating insulin-stimulated glucose uptake in humans: Studies using bradykinin, [^{15}O]water, and [^{18}F]fluoro-deoxy-glucose and positron emission tomography. *Journal of Clinical Investigation*, *97*(7), 1741–1747. https://doi.org/10.1172/JCI118601

Oguro, A., Taniguchi, H., Koyama, H., Tanaka, H., Miyata, K., Takeuchi, K., Inaba, T., Nakahashi, H., & Takahashi, T. (1993). Quantification of human splenic blood flow (Quantitative measurement of splenic blood flow with $H_2{}^{15}O$ and a dynamic state method: 1). *Annals of Nuclear Medicine*, *7*(4), 245–250. https://doi.org/10.1007/BF03164705

Patlak, C. S., & Blasberg, R. G. (1985). Graphical evaluation of blood-to-brain transfer constants from multiple-time uptake data. Generalizations. *Journal of Cerebral Blood Flow and Metabolism*, *5*(4), 584–590. https://doi.org/10.1038/jcbfm.1985.87

Patlak, C. S., Blasberg, R. G., & Fenstermacher, J. D. (1983). Graphical evaluation of blood-to-brain transfer constants from multiple-time uptake data. *Journal of Cerebral Blood Flow and Metabolism*, *3*(1), 1–7. https://doi.org/10.1038/jcbfm.1983.1

Petrovic, P., Petersson, K. M., Ghatan, P. H., Stone-Elander, S., & Ingvar, M. (2000). Pain-related cerebral activation is altered by a distracting cognitive task. *Pain*, *85*(1–2), 19–30. https://doi.org/10.1016/S0304-3959(99)00232-8

Phelps, M. E., Huang, S. C., Hoffman, E. J., Selin, C., & Kuhl, D. E. (1981). Cerebral extraction of N-13 ammonia: Its dependence on cerebral blood flow and capillary permeability — surface area product. *Stroke*, *12*(5), 607–619. https://doi.org/10.1161/01.STR.12.5.607

Phelps, M. E., Huang, S. C., Hoffman, E. J., Selin, C., Sokoloff, L., & Kuhl, D. E. (1979). Tomographic measurement of local cerebral glucose metabolic rate in humans with (F-18)2-fluoro-2-deoxy-D-glucose: Validation of method. *Annals of Neurology*, *6*(5), 371–388. https://doi.org/10.1002/ana.410060502

Poon, J. K., Dahlbom, M. L., Moses, W. W., Balakrishnan, K., Wang, W., Cherry, S. R., & Badawi, R. D. (2012). Optimal whole-body PET scanner configurations for different volumes of LSO scintillator: A simulation study. *Physics in Medicine and Biology*, *57*(13), 4077–4094. https://doi.org/10.1088/0031-9155/57/13/4077

Presotto, L., Gianolli, L., Gilardi, M. C., & Bettinardi, V. (2015). Evaluation of image reconstruction algorithms encompassing Time-Of-Flight and Point Spread Function modelling for quantitative cardiac PET: Phantom studies. *Journal of Nuclear Cardiology*, *22*(2), 351–363. https://doi.org/10.1007/s12350-014-0023-1

Prior, J. O., Schindler, T. H., Facta, A. D., Hernandez-Pampaloni, M., Campisi, R., Dahlbom, M., & Schelbert, H. R. (2007). Determinants of myocardial blood flow response to cold pressor testing and pharmacologic vasodilation in healthy humans. *European Journal of Nuclear Medicine and Molecular Imaging*, *34*(1), 20–27. https://doi.org/10.1007/s00259-006-0193-4

Puig, O., Henriksen, O. M., Vestergaard, M. B., Hansen, A. E., Andersen, F. L., Ladefoged, C. N., Rostrup, E., Larsson, H. B. W., Lindberg, U., & Law, I. (2020). Comparison of simultaneous arterial spin labeling MRI and ^{15}O-H_2O PET measurements of regional cerebral blood flow in rest and altered perfusion states. *Journal of Cerebral Blood Flow and Metabolism*, *40*(8), 1621–1633. https://doi.org/10.1177/0271678X19874643

Quarles, R. P., Mintun, M. A., Larson, K. B., Markham, J., Macleod, A. M., & Raichle, M. E. (1993). Measurement of regional cerebral blood flow with positron emission tomography: a comparison of [^{15}O] water to [^{11}C] butanol with distributed-parameter and compartmental models. *Journal of Cerebral Blood Flow and Metabolism*, *13*, 733–747.

Raichle, M. E., Eichling, J. O., Straatmann, M. G., Welch, M. J., Larson, K. B., & Ter-Pogossian, M. M. (1976). Blood brain barrier permeability of ^{11}C labeled alcohols and ^{15}O labeled water. *American Journal of Physiology*, *230*(2), 543–552. https://doi.org/10.1152/ajplegacy.1976.230.2.543

Raichle, M. E., Martin, W. R., Herscovitch, P., Mintun, M. A., & Markham, J. (1983). Brain blood flow measured with intravenous $H_2{}^{15}O$. II. Implementation and validation. *Journal of Nuclear Medicine*, *24*(9), 790–798.

Raitakari, M., Knuuti, M. J., Ruotsalainen, U., Laine, H., Makela, P., Teras, M., Sipila, H., Niskanen, T., Raitakari, O. T., Iida, H., Harkonen, R., Wegelius, U., Yki- Jarvinen, H., & Nuutila, P. (1995). Insulin increases blood volume in human skeletal muscle: Studies using [^{15}O]CO and positron emission tomography. *American Journal of Physiology - Endocrinology and Metabolism*, *269*(6 32-6). https://doi.org/10.1152/ajpendo.1995.269.6.e1000

Rankin, E. B., & Giaccia, A. J. (2008). The role of hypoxia-inducible factors in tumorigenesis. In *Cell Death and Differentiation* (Vol. 15, Issue 4, pp. 678–685). Nature Publishing Group. https://doi.org/10.1038/cdd.2008.21

Renkin, E. M. (1959). Transport of potassium-42 from blood to tissue in isolated mammalian skeletal muscles. *The American Journal of Physiology*, *197*, 1205–1210. https://doi.org/10.1152/ajplegacy.1959.197.6.1205

Roth, K. S., Voltin, C. A., van Heek, L., Wegen, S., Schomäcker, K., Fischer, T., Marnitz, S., Drzezga, A., Kobe, C., & Roth, K. (2022). Dual-tracer PET/CT protocol with [^{18}F]-FDG and [^{68}Ga]Ga-FAPI-46 for cancer imaging - a proof of concept. *Journal of Nuclear Medicine*, jnumed.122.263835. https://doi.org/10.2967/JNUMED.122.263835

Rumboldt, Z., Al-Okaili, R., & Deveikis, J. P. (2005). Perfusion CT for head and neck tumors: Pilot study. *American Journal of Neuroradiology*, *26*(5), 1178–1185. /pmc/articles/PMC8158592/

Rutland, M. D. (1979). A single injection technique for subtraction of blood background in ^{131}I-hippuran renograms. *British Journal of Radiology*, *52*(614), 134–137. https://doi.org/10.1259/0007-1285-52-614-134

Sage, J. I., van Uitert, R. L., & Duffy, T. E. (1981). Simultaneous measurement of cerebral blood flow and unidirectional movement of substances across the blood-brain barrier: Theory, method, and application to leucine. *Journal of Neurochemistry*, *36*(5), 1731–1738. https://doi.org/10.1111/j.1471-4159.1981.tb00425.x

Sahani, D. v., Kalva, S. P., Hamberg, L. M., Hahn, P. F., Willett, C. G., Saini, S., Mueller, P. R., & Lee, T. Y. (2005). Assessing tumor perfusion and treatment response in rectal cancer with multisection CT: Initial observations. *Radiology*, *234*(3), 785–792. https://doi.org/10.1148/radiol.2343040286/asset/images/large/r05mr12la2x.jpeg

Sánchez-Crespo, A., Andreo, P., & Larsson, S. A. (2004). Positron flight in human tissues and its influence on PET image spatial resolution. *European Journal of Nuclear Medicine and Molecular Imaging*, *31*(1), 44–51. https://doi.org/10.1007/s00259-003-1330-y

Schelbert, H. R., Phelps, M. E., Huang, S. C., MacDonald, N. S., Hansen, H., Selin, C., & Kuhl, D. E. (1981). N-13 ammonia as an indicator of myocardial blood flow. *Circulation*, *63*(6 I), 1259–1272. https://doi.org/10.1161/01.CIR.63.6.1259

Schindler, T. H., Nitzsche, E. U., Olschewski, M., Brink, I., Mix, M., Prior, J., Facta, A., Inubushi, M., Just, H., & Schelbert, H. R. (2004). PET-measured responses of MBF to cold pressor testing correlate with indices of coronary vasomotion on quantitative coronary angiography. *Journal of Nuclear Medicine*, *45*(3), 419–428. https://doi.org/10.1097/00006231-200404000-00092

Schindler, T. H., Zhang, X. L., Prior, J. O., Cadenas, J., Dahlbom, M., Sayre, J., & Schelbert, H. R. (2007). Assessment of intra- and interobserver reproducibility of rest and cold pressor test-stimulated myocardial blood flow with ^{13}N-ammonia and PET. *European Journal of Nuclear Medicine and Molecular Imaging*, *34*(8), 1178–1188. https://doi.org/10.1007/s00259-007-0378-5

Schober, O. H., Meyer, G. J., Bossaller, C., Creutzig, H., Lichtlen, P. R., & Hundeshagen, H. (1985). Quantitative determination of regional extravascular lung water and regional blood volume in congestive heart failure. *European Journal of Nuclear Medicine*, *10*(1–2), 17–24. https://doi.org/10.1007/BF00261757

Schuster, D. P., Kaplan, J. D., Gauvain, K., Welch, M. J., & Markham, J. (1995). Measurement of regional pulmonary blood flow with PET. *Journal of Nuclear Medicine*, *36*(3), 371–377.

Schwaiger, M. (1994). Myocardial perfusion imaging with PET. *Journal of Nuclear Medicine*, *35*(4), 693–698.

Shannon, A. M., Bouchier-Hayes, D. J., Condron, C. M., & Toomey, D. (2003). Tumour hypoxia, chemotherapeutic resistance and hypoxia-related therapies. *Cancer Treatment Reviews*, *29*(4), 297–307. https://doi.org/10.1016/S0305-7372(03)00003-3

Siegrist, P. T., Gaemperli, O., Koepfli, P., Schepis, T., Namdar, M., Valenta, I., Aiello, F., Fleischmann, S., Alkadhi, H., & Kaufmann, P. A. (2006). Repeatability of cold pressor test-induced flow increase assessed with $H_2{}^{15}O$ and PET. *Journal of Nuclear Medicine*, *47*(9), 1420–1426.

Siekkinen, R., Teuho, J., Smith, N. A. S., Fenwick, A., Kirjavainen, A. K., Koskensalo, K., Saraste, A., & Teräs, M. (2020). Study of the effect of reconstruction parameters for myocardial perfusion imaging in PET with a novel flow phantom. *Frontiers in Physics*, *8*, 148. https://doi.org/10.3389/fphy.2020.00148

Sokoloff, L., Reivich, M., Kennedy, C., Rosiers, M. H. des, Patlak, C. S., Pettigrew, K. D., Sakurada, O., & Shinohara, M. (1977). The [^{14}C]deoxyglucose method for the measurement of local cerebral glucose utilization: theory, procedure, and normal values in the conscious and anesthetized albino rat. *Journal of Neurochemistry*, *28*(5), 897–916. https://doi.org/10.1111/j.1471-4159.1977.tb10649.x

Soldin, O. P., & Mattison, D. R. (2009). Sex differences in pharmacokinetics and pharmacodynamics. *Clinical Pharmacokinetics*, *48*(3), 143–157. https://doi.org/10.2165/00003088-200948030-00001

Spencer, B. A., Berg, E., Schmall, J. P., Omidvari, N., Leung, E. K., Abdelhafez, Y. G., Tang, S., Deng, Z., Dong, Y., Lv, Y., Bao, J., Liu, W., Li, H., Jones, T., Badawi, R. D., & Cherry, S. R. (2021). Performance evaluation of the uEXPLORER total-body PET/CT scanner based on NEMA NU 2-2018 with additional tests to characterize PET scanners with a long axial field of view. *Journal of Nuclear Medicine*, *62*(6), 861–870. https://doi.org/10.2967/jnumed.120.250597

Stabin, M. G., & Farmer, A. (2012). OLINDA/EXM 2.0: The new generation dosimetry modeling code. *Journal of Nuclear Medicine*, *53*(supplement 1), 585–585. http://jnm.snmjournals.org/content/53/supplement_1/585

Stabin, M. G., & Siegel, J. A. (2018). RADAR dose estimate report: A compendium of radiopharmaceutical dose estimates based on OLINDA/EXM version 2.0. *J Nucl Med*, *59*, 154–160. https://doi.org/10.2967/jnumed.117.196261

Stabin, M. G., Sparks, R. B., & Crowe, E. (2005). OLINDA/EXM: the second-generation personal computer software for internal dose assessment in nuclear medicine. *Journal of Nuclear Medicine*, *46*(6), 1023–1027. http://www.ncbi.nlm.nih.gov/pubmed/15937315

Sun, D. Q., Nguyen, N., DeGrado, T. R., Schwaiger, M., & Brosius, F. C. (1994). Ischemia induces translocation of the insulin-responsive glucose transporter GLUT4 to the plasma membrane of cardiac myocytes. *Circulation*, *89*(2), 793–798. https://doi.org/10.1161/01.CIR.89.2.793

Sundar, L. S., Iommi, D., Spencer, B., Wang, Q., Cherry, S., Beyer, T., & Badawi, R. (2021). Data-driven motion compensation using cGAN for total-body [^{18}F]FDG-PET imaging. *Journal of Nuclear Medicine*, *62*(supplement 1), 35 LP – 35.

Sundar, L. S., Wang, Y., Spencer, B. A., Wang, G., Li, E. J., Cherry, S. R., Beyer, T., & Badawi, R. D. (2021). Motion correction using multi-resolution scheme (MOTIONLESS) for ^{18}F-FDG Total-body PET/CT systems. *IEEE Nuclear Science Symposium and Medical Imaging Conference*.

Swartz, M. A., & Fleury, M. E. (2007). Interstitial flow and its effects in soft tissues. *Annual Review of Biomedical Engineering*, *9*(1), 229–256.

Takagi, S., Ehara, K., Kenny, P. J., Finn, R. D., Kothari, P. J., & Gilson, A. J. (1984). Measurement of cerebral blood flow in the rat with intravenous injection of [^{11}C]butanol by external coincidence counting: A repeatable and noninvasive method in the brain. *Journal of Cerebral Blood Flow and Metabolism*, *4*(2), 275–283. https://doi.org/10.1038/jcbfm.1984.38

Tamaki, N., Yonekura, Y., Yamashita, K., Saji, H., Magata, Y., Senda, M., Konishi, Y., Hirata, K., Ban, T., & Konishi, J. (1989). Positron emission tomography using fluorine-18 deoxyglucose in evaluation of coronary artery bypass grafting. *The American Journal of Cardiology*, *64*(14), 860–865. https://doi.org/10.1016/0002-9149(89)90832-1

Taniguchi, H., Masuyama, M., Koyama, H., Oguro, A., & Takahashi, T. (1996). Quantitative measurement of human tissue hepatic blood volume by C^{15}O inhalation with positron-emission tomography. *Liver*, *16*(4), 258–262. https://doi.org/10.1111/j.1600-0676.1996.tb00739.x

Taniguchi, H., Yamaguchi, A., Kunishima, S., Koh, T., Masuyama, M., Koyama, H., Oguro, A., & Yamagishi, H. (1999). Using the spleen for time-delay correction of the input function in measuring hepatic blood flow with oxygen-15 water by dynamic PET. *Annals of Nuclear Medicine*, *13*(4), 215–221. https://doi.org/10.1007/BF03164895

Tian, M., Ogawa, K., Wendt, R., Mukhopadhyay, U., Balatoni, J., Fukumitsu, N., Uthamanthil, R., Borne, A., Brammer, D., Jackson, J., Mawlawi, O., Yang, B., Alauddin, M. M., & Gelovani, J. G. (2011). Whole-body biodistribution kinetics, metabolism, and radiation dosimetry estimates of ^{18}F-PEG6-IPQA in nonhuman primates. *Journal of Nuclear Medicine*, *52*(6), 934–941. https://doi.org/10.2967/jnumed.110.086777

Tillisch, J., Brunken, R., Marshall, R., Schwaiger, M., Mandelkern, M., Phelps, M., & Schelbert, H. (1986). Reversibility of cardiac wall-motion abnormalities predicted by positron

tomography. *New England Journal of Medicine*, *314*(14), 884–888. https://doi.org/10.1056/nejm198604033141405

Tran, Q., Matsukuma, K., Spencer, B. A., Wang, Y., Li, E. J., Corwin, M. T., Cherry, S. R., Badawi, R. D., Sarkar, S., & Wang, G. (2022). High-temporal resolution kinetic modeling on total-body PET differentiates the hepatic interstitial space in nonalcoholic fatty liver disease and healthy subjects [Abstract]. *Journal of Nuclear Medicine*.

Valentin, J. (2002). Basic anatomical and physiological data for use in radiological protection: reference values: ICRP Publication 89. *Annals of the ICRP*, *32*(3–4), 1–277. https://doi.org/10.1177/ANIB_32_3-4

Velasco, M., Gómez, J., Blanco, M., & Rodriguez, I. (1997). The cold pressor test: Pharmacological and therapeutic aspects. *American Journal of Therapeutics*, *4*(1), 34–38. https://doi.org/10.1097/00045391-199701000-00008

Virani, S. S., Aparicio, H. J., Benjamin, E. J., Callaway, C. W., Carson, A. P., Cheng, S., Elkind, M. S. V, Evenson, K. R., Ferguson, J. F., Knutson, K. L., Lee, C. D., Lewis, T. T., Loop, M. S., Lutsey, P. L., Mackey, J., & Matchar, D. B. (2021). Heart disease and stroke statistics-2021 update a report from the American Heart Association. *Circulation*, *143*, E254–E743. https://doi.org/10.1161/CIR.0000000000000950

Vraka, C., Murgaš, M., Rischka, L., Geist, B. K., Lanzenberger, R., Gryglewski, G., Zenz, T., Wadsak, W., Mitterhauser, M., Hacker, M., Philippe, C., & Pichler, V. (2022). Simultaneous radiomethylation of [^{11}C]harmine and [^{11}C]DASB and kinetic modeling approach for serotonergic brain imaging in the same individual. *Scientific Reports 2022 12:1*, *12*(1), 1–12. https://doi.org/10.1038/s41598-022-06906-0

Wahood, W., Ghozy, S., Al-Abdulghani, A., & Kallmes, D. F. (2022). Radial artery diameter: a comprehensive systematic review of anatomy. *Journal of Neurointerventional Surgery*, neurintsurg-2021-018534. https://doi.org/10.1136/NEURINTSURG-2021-018534

Wallstén, E., Axelsson, J., Karlsson, M., Riklund, K., & Larsson, A. (2017). A study of dynamic PET frame-binning on the reference logan binding potential. *IEEE Transactions on Radiation and Plasma Medical Sciences*, *1*(2), 128–135.

Wang, G., Corwin, M. T., Olson, K. A., Badawi, R. D., & Sarkar, S. (2018). Dynamic PET of human liver inflammation: impact of kinetic modeling with optimization-derived dual-blood input function. *Physics in Medicine and Biology*, *63*(15), 155004. https://doi.org/10.1088/1361-6560/aac8cb

Wang, G., Nardo, L., Parikh, M., Abdelhafez, Y. G., Li, E. J., Spencer, B. A., Qi, J., Jones, T., Cherry, S. R., & Badawi, R. D. (2021). Total-Body PET multiparametric imaging of cancer using a voxel-wise strategy of compartmental modeling. *Journal of Nuclear Medicine*, jnumed.121.262668. https://doi.org/10.2967/jnumed.121.262668

Wang, G., & Qi, J. (2009). Generalized algorithms for direct reconstruction of parametric images from dynamic PET data. *IEEE Transactions on Medical Imaging*, *28*(11), 1717–1726. https://doi.org/10.1109/TMI.2009.2021851

Wang, G., & Qi, J. (2015). PET image reconstruction using kernel method. *IEEE Transactions on Medical Imaging*, *34*(1), 61–71. https://doi.org/10.1109/TMI.2014.2343916

Wang, Y., Cherry, S. R., Badawi, R. D., & Wang, G. (2020). Effect of dual-input function and dispersion on lung FDG-PET kinetic quantification using the EXPLORER total-body PET/CT scanner. *Journal of Nuclear Medicine*, *61*(supplement 1).

Wang, Y., Li, E. J., Cherry, S. R., & Wang, G. (2021). Total-Body PET kinetic modeling and potential opportunities using deep learning. *PET Clinics*, *16*(4), 613–625. https://doi.org/10.1016/j.cpet.2021.06.009

Wang, Z., Mascarenhas, C., & Jia, X. (2020). Positron emission tomography after ischemic brain injury: current challenges and future developments. In *Translational Stroke Research* (Vol. 11, Issue 4, pp. 628–642). Springer. https://doi.org/10.1007/s12975-019-00765-0

Warburg, O., Wind, F., & Negelein, E. (1927). The metabolism of tumors in the body. *The Journal of General Physiology*, *8*(6), 519. https://doi.org/10.1085/JGP.8.6.519

Watabe, H., Ikoma, Y., Kimura, Y., Naganawa, M., & Shidahara, M. (2006). PET kinetic analysis - Compartmental model. *Annals of Nuclear Medicine*, *20*(9), 583–588. https://doi.org/10.1007/BF02984655

Wells, J. M., Mankoff, D. A., Muzi, M., O'Sullivan, F., Eary, J. F., Spence, A. M., & Krohn, K. A. (2002). Kinetic Analysis of 2-[^{11}C]Thymidine PET Imaging Studies of Malignant Brain Tumors: Compartmental Model Investigation and Mathematical Analysis. *Molecular Imaging*, *1*(3), 151–159. https://doi.org/10.1162/15353500200202112

Wilson, T. D., Shoemaker, J. K., Kozak, R., Lee, T. Y., & Gelb, A. W. (2005). Reflex-mediated reduction in human cerebral blood volume. *Journal of Cerebral Blood Flow and Metabolism*, *25*(1), 136–143. https://doi.org/10.1038/sj.jcbfm.9600015

Wu, Y., & Carson, R. E. (2002). Noise reduction in the simplified reference tissue model for neuroreceptor functional imaging. *Journal of Cerebral Blood Flow and Metabolism*, *22*(12), 1440–1452. https://doi.org/10.1097/01.WCB.0000033967.83623.34

Yamagishi, H., Akioka, K., Hirata, K., Sakanoue, Y., Takeuchi, K., Yoshikawa, J., & Ochi, H. (1999). A reverse flow-metabolism mismatch pattern on PET is related to multivessel disease in patients with acute myocardial infarction. *Journal of Nuclear Medicine*, *40*(9), 1492–1498.

Yamagishi, H., Akioka, K., Hirata, K., Sakanoue, Y., Toda, I., Yoshiyama, M., Teragaki, M., Takeuchi, K., Yoshikawa, J., & Ochi, H. (2000). A reverse flow - Metabolism mismatch pattern: A new marker of viable myocardium with greater contractility during dobutamine stress than myocardium with a flow-metabolism mismatch pattern. *Japanese Circulation Journal*, *64*(9), 659–666. https://doi.org/10.1253/jcj.64.659

Yamashita, M., Inaba, T., Oda, Y., & Mizukawa, N. (1989). Renal blood volume vs. glomerular filtration rate: evaluation with C^{15}O and ^{88}Ga-ethylenediaminetetraacetic acid (EDTA) study. *Radioisotopes*, *38*(9), 373–376. https://doi.org/10.3769/radioisotopes.38.9_373

Yan, C., Han, X., Liang, X., Jia, J., Xu, Y., & Zhao, L. (2022). Non-invasive evaluation of esophageal varices in patients with liver cirrhosis using low-dose splenic perfusion CT. *European Journal of Radiology*, *152*(October 2021), 110326. https://doi.org/10.1016/j.ejrad.2022.110326

Zanotti-Fregonara, P., Lammertsma, A. A., & Innis, R. B. (2021). ^{11}C dosimetry scans should be abandoned. In *Journal of Nuclear Medicine* (Vol. 62, Issue 2, pp. 158–159). Society of Nuclear Medicine. https://doi.org/10.2967/jnumed.120.257402

Zhang, X., Cherry, S. R., Xie, Z., Shi, H., Badawi, R. D., & Qi, J. (2020). Subsecond total-body imaging using ultrasensitive positron emission tomography. *Proceedings of the National Academy of Sciences of the United States of America*, *117*(5), 2265–2267. https://doi.org/10.1073/pnas.1917379117

Zuo, Y., López, J. E., Smith, T. W., Foster, C. C., Carson, R. E., Badawi, R. D., & Wang, G. (2021). Multiparametric cardiac ^{18}F-FDG PET in humans: pilot comparison of FDG delivery

rate with ^{82}Rb myocardial blood flow. *Physics in Medicine & Biology*, *66*(15), 155015. https://doi.org/10.1088/1361-6560/ac15a6

Zuo, Y., Sarkar, S., Corwin, M. T., Olson, K., Badawi, R. D., & Wang, G. (2019). Structural and practical identifiability of dual-input kinetic modeling in dynamic PET of liver inflammation. *Physics in Medicine & Biology*, *64*(17), 175023. https://doi.org/10.1088/1361-6560/ab1f29